Electrorotation of the Bacterial Flagellar Motor

TANIA E. SAXL

A thesis submitted in partial fulfillment of
the requirements for the degree of
Doctor of Philosophy at the University of Oxford

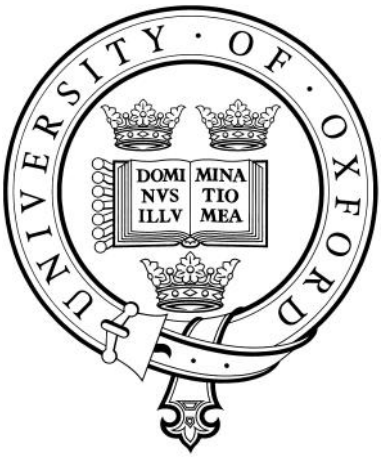

Merton College
University of Oxford
Hilary Term 2007

Electrorotation of the Bacterial Flagellar Motor

Tania E. Saxl
Merton College

Thesis submitted for the degree of Doctor of Philosophy
at the University of Oxford, Hilary Term 2007

Abstract

Knowledge of the relationship between the torque generated by the bacterial flagellar motor of *Escherichia coli* and its rotation rate provides a valuable insight into the mechanism of the motor's function. A method was devised to measure this characteristic in the high-speed, low-load regime, so that the effect of stator number could be investigated. This involved the electrorotation of a polarisable particle, attached to the bacterial filament, as a handle to rotate the motor. I designed and built an upright laser position detector and fabricated an electrode flow cell and optically asymmetric, polarisable particles. The particles allow a high resolution to be achieved, so that stator numbers can be distinguished. The flow cell enables positioning of the bacterium with respect to the electrodes and exchange of the medium during the experiment. Using the novel flow cell, previous torque speed measurements for the flagellar motor of *E. coli*, made by rotating the cell body about its tether point, were confirmed. The method was extended to measure the torque speed curve for the polarisable particle attached to the filament. I was then able to determine a torque speed curve for varying stator numbers. Results indicate that the zero-torque speed decreases for decreasing stator numbers, contrary to previous assumptions.

Contents

Chapter 1

Introduction

The subject of this thesis is the bacterial flagellar motor, a molecular machine that bacteria use to swim. The flagellar motor is attached to a long, rigid filament that it rotates, propelling the organism through its environment. Although much is known about the flagellar motor, the mechanism by which it functions is still unclear. The relationship between torque generated by the motor and the speed of rotation is one of the most important measurable biophysical characteristics of the motor, it is this information that can be best used to test theoretical models of motor function.

This introduction will cover molecular motors, optical trapping and electrorotation, with particular reference to the bacterial flagellar motor. It has been my goal to bring together small aspects from each of these fields to extend knowledge of the torque speed relationship to the high-speed, low-torque regime and to single stator units, in order to attempt to understand how these units work in combination.

1.1 The mechanics of molecular motor proteins

Nothing in nature is stationary. When a cell is observed under a light microscope it is possible to see cargo of the sub-nanometre sized motor proteins, rushing along cellular tracks, in constant motion. Eukaryotes, of which plants, insects and ourselves are members, have a complex intracellular network called the cytoskeleton. This filamental structure provides a pathway for a teeming mass of active proteins, traveling back and forth to the various organelles distributed throughout the cell. Part of the cytoskeleton is made up of actin and microtubules, filaments used by linear motor proteins myosin and kinesin respectively as a track to guide them through the cytoplasm. It is not just the obvious cargo carrying proteins that behave as actuators, motility of the cells themselves is brought about by motor proteins. A second function of microtubules is to form cilia, protrusions from the cell surface that bend in coordinated waves to move the external medium. The beating of cilia is generated by large assemblies of the motor protein dynein [1]. Further down the scale, it is even possible to think of biological enzymes as motors, for example DNA helicase, which unwinds duplex DNA to form single stranded DNA. Mechanistic similarities to kinesin have been inferred and comparison between the underlying mechanisms of these molecular motors can be usefully made [2].

Prokaryotic cells, such as bacteria, have no organelles. It was originally thought that they simply contained an homogenous soup of chemicals, necessary for the cell's proliferation. However, these tiny organisms have a wondrously complex level of organisation that is becoming apparent as new proteins are discovered. Homologues to actin, tubulin and other intermediate filament proteins have been found, along with a fourth group of cytoskeletal proteins, believed to be unique to bacteria [3]. Prokaryote cells are far from simplistic.

Bacteria are able to synthesize one of the largest, most complex protein structures in nature, the flagellar motor. Rotation of the bacterial flagellar motor allows many species of bacteria, including *Escherichia coli* to swim. The motor has been studied for decades and the knowledge we have on the subject is voluminous, however, the precise mechanism by which the motor generates movement is not known, partly due to its size and also its location in the membrane envelope. Although it is a rotary motor, and despite its size, aspects of the mechanism of torque generation might be related to that of other motor proteins, including linear motors. A few of the families of motor proteins and the way in which they move, are therefore discussed in this section.

1.1.1 Linear motors of the eukaryotic cell

Kinesin

Cytoplasmic microtubules radiate from the centre of the cell out to the periphery and are part of the eukaryotic cytoskeleton [4]. They are hollow tubes formed from tubulin dimers. Kinesin is a molecular machine that walks along the microtubules transporting cargo throughout the cell. It is a linear motor protein that uses the hydrolysis of Adenosine Triphosphate (ATP) to move along the microtubules. It carries a wide variety of cargo from vesicles containing RNA molecules to whole organelles such as mitochondria. The widely studied conventional kinesin is one member of a large and diverse kinesin superfamily. It is an example of a processive motor protein with a high duty ratio, this means that it spends a high fraction of its time bound to the microtubule, in fact one of its motor domains is always bound. Kinesin is therefore able to take several hundred steps along the microtubule before detaching, which allows it to carry its cargo over long ranges.

Conventional kinesin is a dimer with two motor domains, see figure 1.1, coloured blue in the figure. These two domains are joined to a long coiled-coil neck domain, coloured grey, by a neck linker, coloured red for the leading head and yellow for the trailing head linker. Kinesin walks by placing one head domain in front of the other, in a hand-over-hand pattern [5]. It takes $8nm$ steps along the microtubule, independent of ATP concentration and load [6]. Stepping is a tightly coupled process with one molecule of ATP being used per step [7]. There are two distinct models for the kinesin stepping mechanism, a lever arm model which relies on a powerstroke, and a diffusional model. In the first type, the motor head domain attaches tightly to the track, where it undergoes a conformational change. The motion associated with the change of shape is amplified by a rigid lever arm. When kinesin binds ATP the neck linker region becomes rigid, release of the phosphate returns the linker to a mobile state [8]. The diffusional model is a thermal ratchet type model. The motor domain diffuses along the microtubule, stretching a theoretical spring. When the head binds, the energy is captured. Here the conformational change functions to secure binding, but does not stretch the spring [9, 10]. Carter and Cross recently showed that it was possible to drive the kinesin to step backwards, using a bead attached to the kinesin dimer and held in an optical trap [11]. They were also unable to resolve substeps in the motion at the $50\mu s$ resolution of the experiment, where substeps would not be expected in diffusional motion but might be evident in a powerstroke. Although these results do not confirm either hypothesis they do place limits on a model for the motion [12].

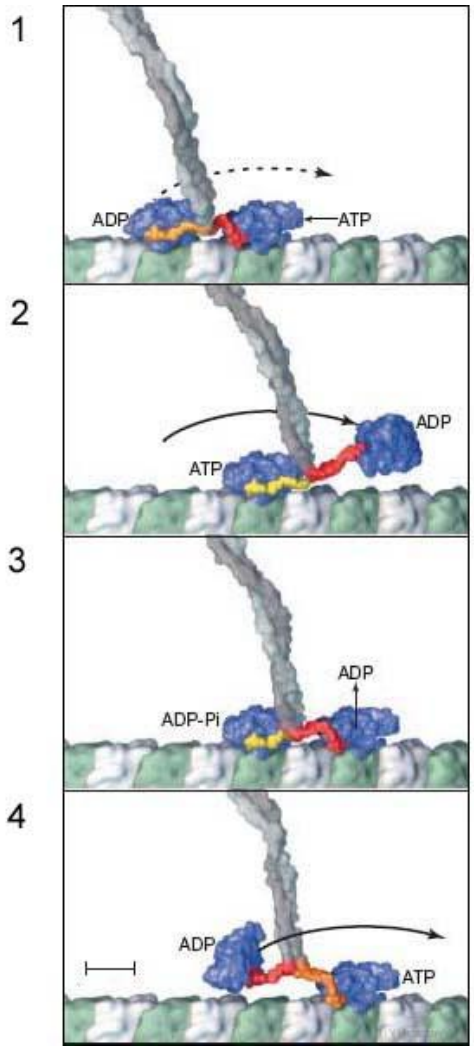

Figure 1.1: A model for the mechanism of kinesin motility. The two heads of kinesin coordinate their motion. 1: Each motor domain (blue) is bound to a tubulin monomer. The neck linker points forwards on the trailing head (orange) and backwards on the leading head (red). ATP binding to the leading head initiates the docking of the neck domain. 2: Docking of the neck domain throws the trailing head forward, this becomes the new leading head with red neck domain. 3: After a diffusional search the new leading head docks on the binding site and it releases ADP. The new trailing head hydrolyses ATP to ADP + Pi. 4: ADP dissociates and the leading head binds ATP and the stepping motion is repeated. Scale bar 4nm. Figure from Vale and Milligan [13]

Myosin

Myosins are motor proteins that use ATP hydrolysis to move along actin filaments. Conventional myosin, myosin II, has its role in muscle and has been well studied. A muscle cell is composed of thick and thin filaments that slide past each other when muscle contracts. The thin filaments are actin protein filaments and what once appeared to be a single thick filament is actually an assembly of myosin II motor proteins. Myosin II, like conventional kinesin, is a dimer. It has two motor domains, see figure 1.2, joined to a long coiled-coil by short linkers or 'lever arms'. It is a low duty ratio motor protein: the percentage of its ATP binding cycle that is spent bound to actin is low. The two heads work independently and only one head of the protein is bound to the actin filament at a time. Unlike conventional kinesin, myosin II executes a single stroke, then dissociates, where the powerstroke of a single motor domain has been observed [14]. A conformational change of the motor domain is proposed to rotate the lever arm, which pulls the actin filament approximately 10nm [13]. Much is known of myosin's role in muscle contraction, however, the role of the myosin superfamily extends far beyond this to motility, endocytosis, cytoplasmic streaming and more [4, 15].

Another member of the myosin superfamily, myosin V, has been shown to have a relatively high duty ratio [16]. It is able to progress several hundred nanometres, corresponding to tens of steps along the acting filament. Myosin V is also made up of two motor head domains, each connected to a lever of three calmodulin molecules. This extra length of the lever domain allows the myosin to take 36nm steps along the actin filament[17]. The suggested mechanism for stepping is that the bound head rotates the lever, moving the centre of mass of the protein 25nm. This step can be broken into two separate mechanical motions corresponding to conformational

changes within the protein [18]. The lever arm of the myosin controls the stroke size [19]. The further 11nm of the step is then achieved by a diffusional search [20].

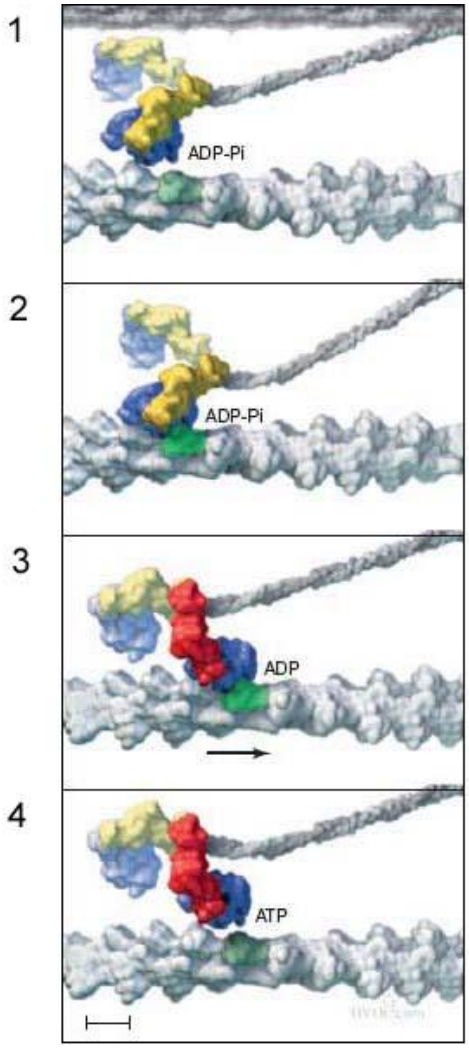

Figure 1.2: A model for the mechanism of muscle myosin, myosin II, motility. 1: The motor domain (blue) of the myosin head binds weakly to actin. The ADP-Pi state is coloured yellow. 2: The head becomes tightly bound to the actin binding site (green). 3: Binding causes phosphate release and the lever arm changes conformation, moving the filament 10nm. Scale bar 6nm. Figure from [13]

1.1.2 Rotary motors

ATP synthase

ATP synthase is a rotary enzyme that generates adenosine triphosphate (ATP) from adenosine diphosphate (ADP) by mechanical action, where ATP is known as the energy currency of the cell. ATP synthase is common to both eukaryotic and prokaryotic cells and is located in the membrane of mitochondria, chloroplasts and bacteria. In *Escherichia coli*, ATP synthase is composed of eight subunits, α β γ δ ϵ a b and c. The complex can be divided into the membrane spanning F_0 motor and the water soluble F_1 motor, see figure 1.3. The F_0 part of the motor uses proton flow to generate torque, driving the synthesis of ATP molecules by F_1. When purified, the F_1 motor generates torque from the energetically favourable hydrolysis of ATP molecules. It has been possible to isolate and crystalise the soluble F_1 motor, enabling it to be studied [21]. F_1 is composed of α, β and γ subunits, where three α and three β subunits are arranged as a trimer of dimers, see figure 1.4. The β subunit contains the catalytic sites where ATP binds. At any time the binding at each site differs, one site binds the hydrolysable form of ATP, the second binds ADP and the third is empty. Binding of ATP causes a conformational change from one state to the next driving rotation of the motor. Single molecule studies of F_1 have found the motor generates around 40pNnm of torque, irrespective of load [22]. The motor is seen to make 120° steps at low ATP concentration and high speed imaging of F_1 has resolved two further substeps of 90° and 30° [23]. Elucidation of a full torque speed profile for the motor would provide information on the underlying mechanism of ATP hydrolysis.

The bacterial flagellar motor - The flagellar motor is the subject of this thesis and as such will be paid special attention in the following sections.

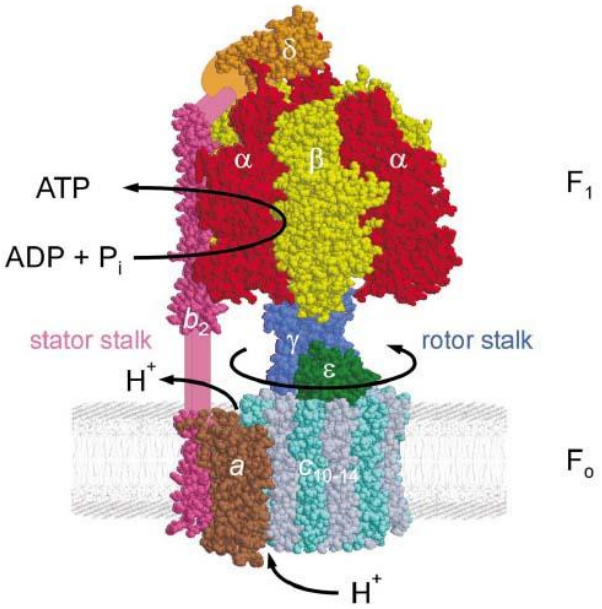

Figure 1.3: The structure of *E.coli* ATP synthase, consisting of eight subunits, $\alpha_3\beta_3\gamma\delta\epsilon ab_2c_n$. The c subunits form a ring. The γ unit has a long coiled coil (not shown) that projects up into the $\alpha_3\beta_3$ hexagon. The proton pathway lies between the a and c subunits. The ATP binding domains are illustrated in figure 1.4. Figure from [24]

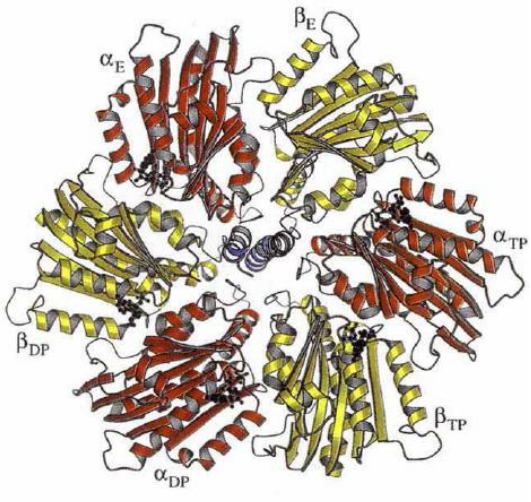

Figure 1.4: The nucleotide binding domains of F_1 ATPase. The nucleotide binding sites are at the interfaces between the β and α subunits. AMP-PNP is bound at β_{TP}, ADP is bound at β_{DP}. At subunit β_E the nucleotide binding site is empty. Figure from [21]

1.2 The flagellar motor of *Escherichia coli*

Figure 1.5: Illustration of an *E. coli* cell with four flagellar filaments. Adapted from K. Namba

The bacterium *Escherichia coli* is a prokaryotic cell of approximately 3μm in length by 1μm in diameter. *E.coli* is a peritrichiously flagellated bacterium (*peri-* around, *trichos-* hair) with $4-6$ filaments randomly distributed around the cell body. Each filament is around 15μm in length and 18nm in diameter. Unlike many other flagellated organisms, the filaments do not waft or oscillate, but instead rotate at approximately 100Hz, propelled by a highly efficient molecular motor, known as the bacterial flagellar motor. When rotating counter clockwise, the multiple flagellar filaments come together to form a helical bundle that propels the bacterium through the environment, see illustration, figure 1.5. When the direction of rotation of one of the filaments is reversed, the bundle splays out and the cell tumbles.

The scale of the bacterium and motor is very important when considering mechanics of the system. *Escherichia coli* lives in an environment that is completely un-intuitive, characterised by low Reynolds number dynamics. The 1μm bacterium swims at roughly $30\mu\text{ms}^{-1}$. In this regime, inertial forces have no bearing on the motion of the motor. If the driving force is removed from the motor, it would stop dead in 0.01nm, coasting for a total of 0.3μs [25].

At 45nm in diameter [26] and the product of nearly 50 genes, the flagellar motor is a large and complex assembly of proteins. Unlike the other motor proteins mentioned, its power source is not ATP but the membrane gradient of ions, H^+

for *Escherichia coli* [27, 28, 29] and Na^+ for some alkalophilic or marine species of the *Bacillus* or *Vibrio* genus [30]. The sodium powered motor is able to rotate extremely fast, at up to 1700 revolutions a second [31, 32]. Measurements of the flux of protons in *Streptococcus* indicates that the motor has an efficiency, far beyond any man-made actuator on this scale, of close to 1 [33].

The motion of the bacterium is directed. In the majority of cases the cell is too tiny to sense spatial variations in its surrounding medium [34], but performs a temporal analysis of its surroundings in order to progress towards a more favourable environment, a process called *chemotaxis*. The cell performs a biased random walk to reach its goal, by alternating between unidirectional runs and re-orienting tumbles. Figure 1.6 shows a projection of the path of an *Escherichia coli* bacterium in an isotropic medium as tracked by Berg and Brown [35]. The frequency of tumble events is moderated according to stimuli in the environment which results in a bias of this random search.

The chemotaxis pathway of *E.coli* is the best understood signalling pathway in biology, it is comparatively simple and utilising only a few types of protein. However, there are thousands of individual proteins involved in the pathway of each cell, and there is yet much to be understood. The regulated switching of the motor is the output from this system. Methyl-accepting chemotaxis proteins (MCPs) in the membrane of the cell detect attractants in the cell's environment [36]. *E.coli* has four types of MCP, Tar, Tsr, Tap and Trg, with Tar and Tsr being the most abundant. Each MCP forms a homodimer [37] and these in turn are arranged in trimers of dimers, where the trimer can be made up of any combination of MCP type. Many thousands of trimers then form tight clusters at the poles of the cell[38]. The cytoplasmic region of the MCP associates, via CheW, with the histidine protein kinase

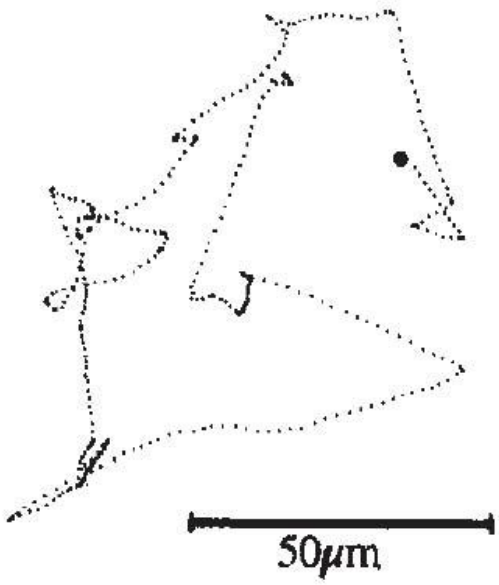

Figure 1.6: Motion in an isotropic solution. Digital plots of the displacement of a wild type bacterium tracked at 12.6 data points a second. Tracking began at the point indicated by the black circle. Figure from [35]

CheA. A decrease in concentration of attractant is transduced across the membrane, resulting in the autophosphorylation of CheA [39]. In *E.coli*, attractants such as aspartate inhibit the kinase activity of CheA. The phosphorylated CheA is able to pass its phosphoryl group to either of two proteins, CheY or CheB [40]. CheB functions with CheR as part of an adaptive feedback mechanism that resets the MCP and it is this feedback that allows for temporal sensing of attractant concentration, see figure 1.7. CheZ acts as a catalyst for the dephosphorylation of CheY-P. CheY-P diffuses to the rotor, where it binds; it is this binding of phosphorylated CheY that causes the motor to switch direction [41].

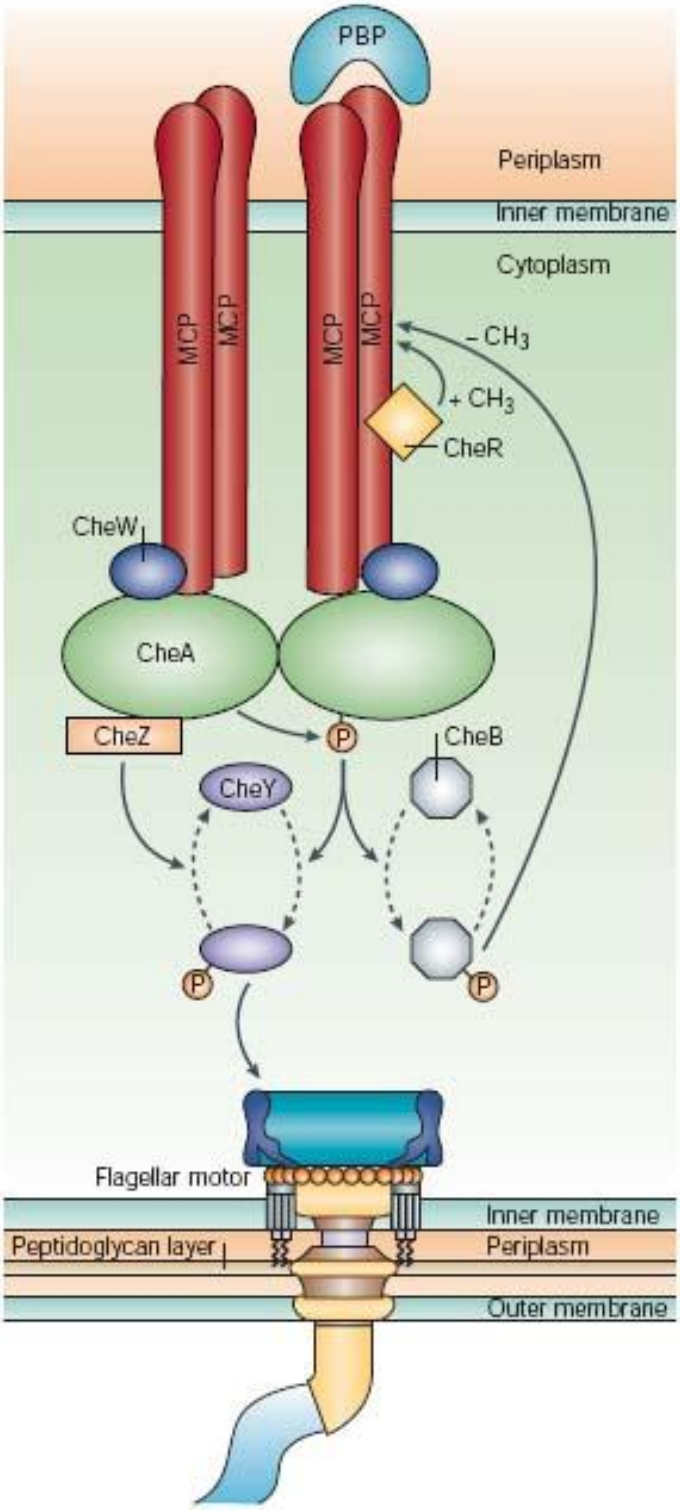

Figure 1.7: Two MCP dimers, coloured red, span the membrane. Each dimer associates with a CheW and CheA dimer. Phosphotransfer occurs from CheA to CheY and CheB. CheY-P binds to the motor and induces switching. CheZ catalyses the release of the phosphoryl group from CheY-P. CheB and CheR are involved in the adaptive feedback that resets the MCP. Figure from [42]

1.3 Structure and function of the bacterial flagellar motor

The body of the flagellar motor of *Escherichia coli* is assembled and operates in the bacterial membrane, which is problematic for structure determination. The lipid molecules that make up each cell membrane, of which *E.coli* has two, form a double layer with a hydrophobic core. As such, membrane channels and other membrane spanning proteins tend to denature when they are removed from the hydrophobic environment and exposed to water. This is also true of the flagellar motor and results in a lack of detailed crystal structure for parts of the motor, such as the torque generating stator units. The motor is also very large at 45nm in diameter at the C-ring, in comparison to other motor proteins such as myosin, where one motor domain is of the order of 10nm [13]. Kinesin is approximately half the size of myosin and F_1 ATPase has a diameter of approximately 10nm [21]. This adds to the difficulty in obtaining crystallographic data for the flagellar motor.

A picture of the motor has therefore been derived from alternative methods such as electron cryomicroscopy, genetic sequencing, mutational studies and partial crystallisation. This has shown that the long flagellar filament is connected via a flexible hook to the basal body, the collective central rod and its surrounding rings, see figure 1.9. The hook acts as a universal joint that transmits torque from the motor to the filament [43]. The entire flagellum is the product of approximately 50 genes, where the basal body consists of a few hundred proteins. In proton powered motors such as *E.coli* the stator is formed from a ring of several proton conducting channels formed from MotA and MotB. For a review of the flagellar motor see Berg or Blair [44, 45].

The flagellar proteins are named after the genes which encode them. Genes, mutants of which produce non-flagellate organisms, were originally called "*fla*" for flagellum, these have since been subdivided alphabetically according to their location in the genome. Genes, mutants of which produce paralysed flagella, were named "*mot*" for motility. DePamphilis and Adler were able to isolate the basal body of the motor, one of their images of purified filament and basal body, taken in 1971, is shown in figure 1.8 [46]. The rings were named by DePamphilis and Adler, who used this purification technique to obtain more detailed electron micrographs of the basal body [47]. The letter M- stands for membrane, S- for supramembranous, P-peptidoglycan and L-lipopolysaccharide, according to the original estimation of their location in the membrane envelope.

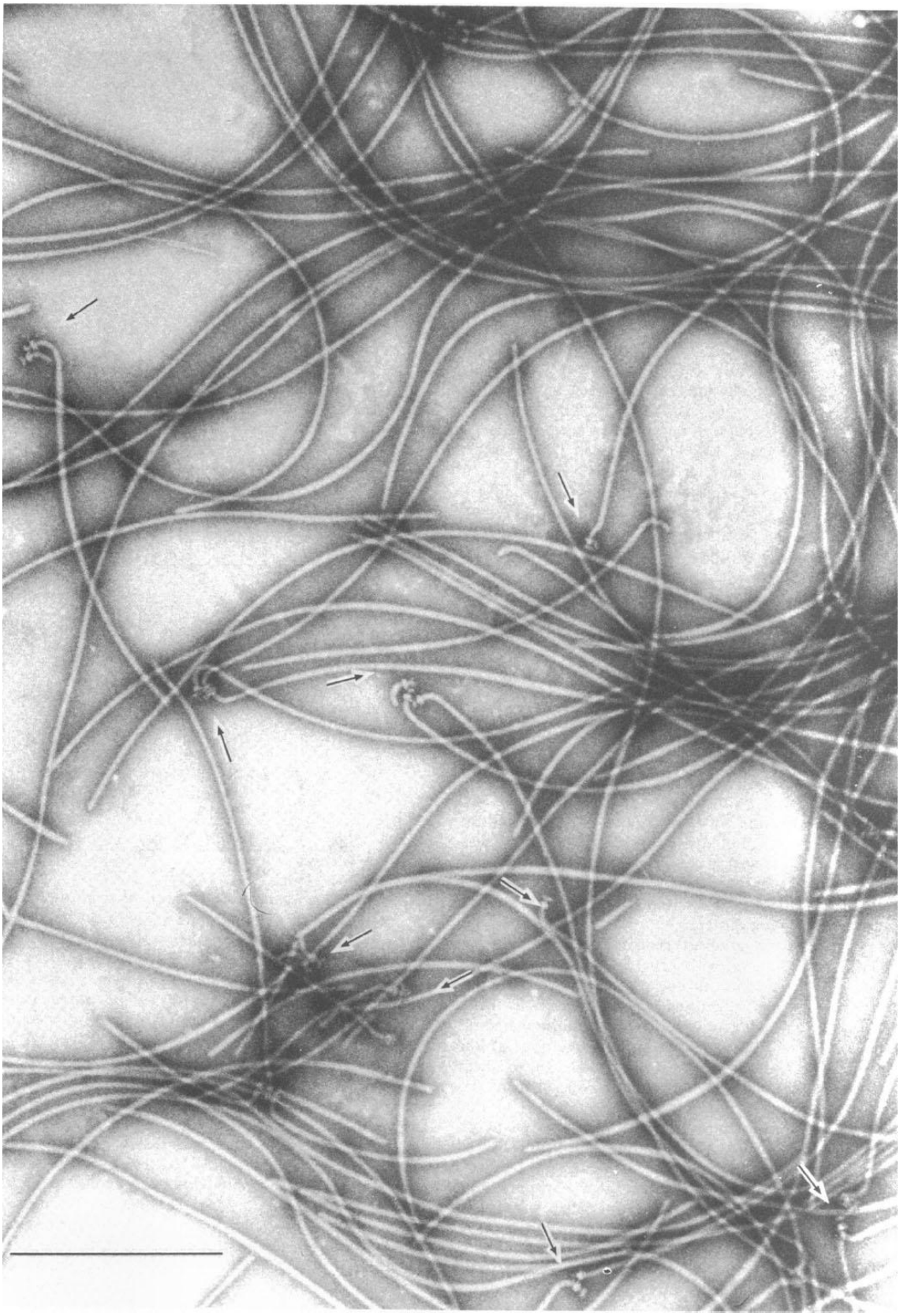

Figure 1.8: Purified intact flagella, negatively stained with uranyl acetate, pH 4.5. Arrows indicate the hook and basal body complex, visible at the end of many of the filaments. Scale 0.5μm. Figure from [46].

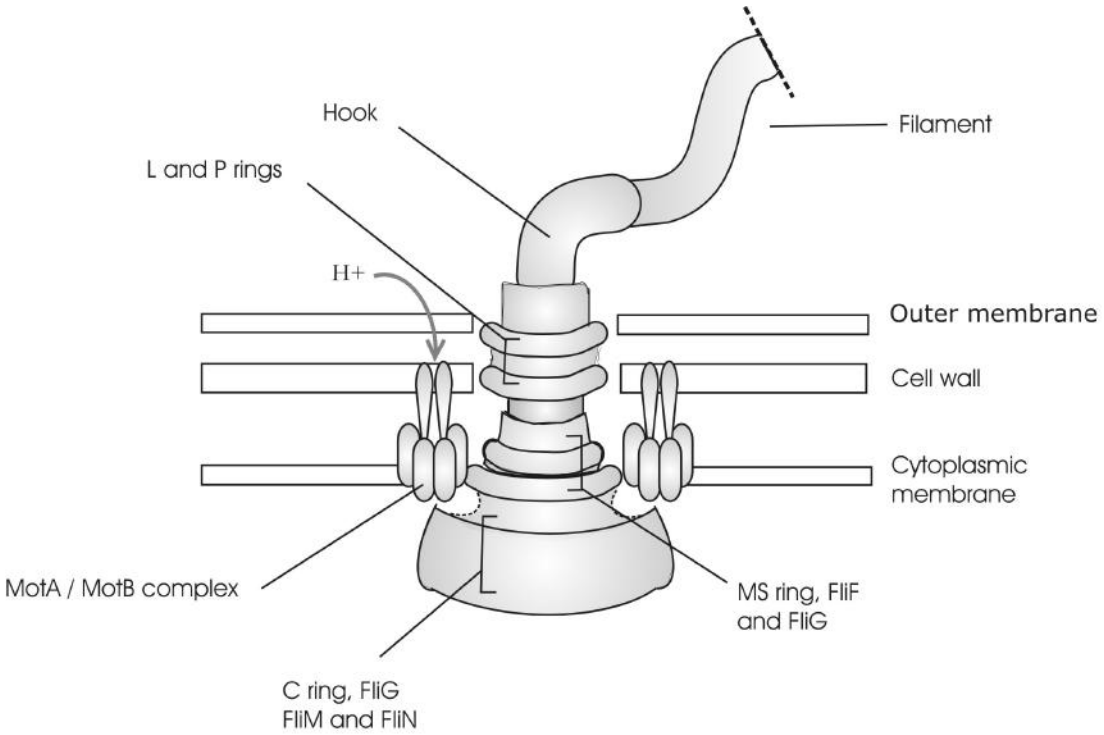

Figure 1.9: Illustration of the bacterial flagellar motor in the cell envelope with suggested MotA and MotB positions, based on structural data [44, 45, 48].

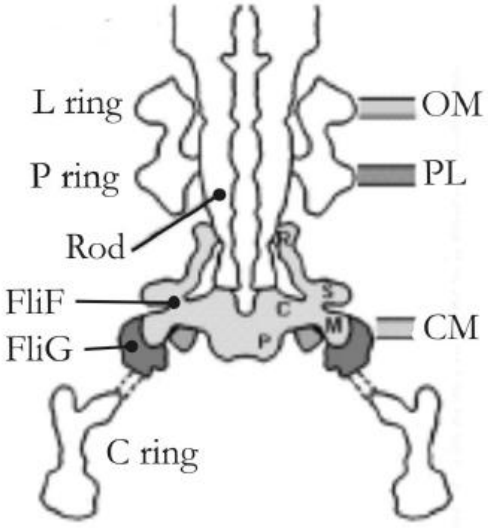

Figure 1.10: Freeze fracture image of the basal body, with the positions of FliF and FliG superimposed. OM=outer membrane, PL=peptidoglycan, CM=cytoplasmic membrane. Adapted from [48].

The central rod or drive shaft of the motor is composed of four proteins, FlgB, FlgC, FlgF and FlgG [49]. The L- and P-rings appear to act like bearings in which the rotor may rotate and are not involved in torque generation [50]. Mutational studies have identified the five proteins active in torque generation as MotA, MotB and FliG, FliM and FliN [51, 52, 53]. The MS-ring, originally thought to be two separate structures, is assembled from the proteins FliF and FliG, and cytoplasmic C-ring from FliG, FliN and FliM, see figure 1.9. An image of the basal body, with the locations of FliG and FliF superimposed, has been obtained by freeze fracture 1.10. FliM and FliN are involved in the transition from CCW to CW rotation and are collectively named the switch complex [54]. There are over 100 copies of FliN in the $45nm$ C-ring and it is estimated that these form around 34 copies of a 1 : 4 FliM:FliN unit [55]. Functionally significant FliG, involved in the generation of torque[52, 53] is located on the cytoplasmic surface of the MS-ring. Images of the FliF ring and the FliFG ring were derived by electron cryomicroscopy and single particle analysis. These density maps indicate 26 fold symmetry of FliF and 1:1 ratio of FliF:FliG. Suzuki *et al.* suggest that FliG is flexible, and possibly an elastic linker such as the neck in myosin. The crystal structure of the C-terminus of FliG in *Thermotoga maritima* was obtained by Lloyd *et al.* and the location of the significant residues resolved, charged residues appear to be clustered along a ridge in this domain [56]. The symmetry of the M- and C-rings was found to vary as 25 and 26 fold in the M-ring and 33, 34 and 35 fold in the C-ring, by Thomas *et al.* [26]. Figure 1.11 shows density maps of M- and C-ring complexes with symmetry of the 25 fold M-ring enforced in a) and c) and the 34 fold C-ring in b) and c).

The molecules MotA and MotB form a membrane spanning proton channel [57, 58]. They are arranged in a ring around the rotor, see figure 1.12. These molecules are thought to form a $MotA_4B_2$ complex that generates torque in the

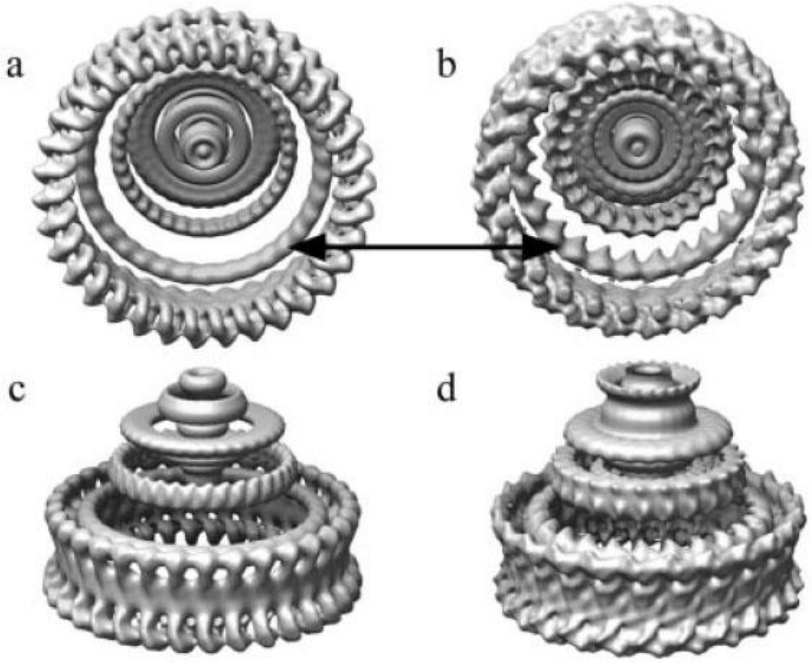

Figure 1.11: Maps of the M- and C-rings, made from images with 25 fold M-rings and 34 fold C-rings. In a) and c) the 34 fold symmetry is enforced on both the M- and C-rings. In b) and d) 25 fold symmetry of the M-ring is enforced. Figure adapted from Thomas and DeRosier [26].

flagellar motor, as indicated by crosslinking and chromatographic studies [45]. Between 11 and 16 of these units are arranged around the MS- and C-rings [59, 60, 61]. They both exhibit hydrophobic membrane spanning sections, where MotA has four membrane spanning helices and MotB one, see figure 1.13. MotA's sequence suggests that most of the rest of the protein lies in the cytoplasm, with only four short loops in the periplasm [62]. MotB exhibits a periplasmic peptidoglycan binding motif and variable loop region at the C-terminus of the protein. The MotAB complex appears to be anchored by this 308 residue to the peptidoglycan of the cell wall [63].

Van Way investigated the function of the periplasmic domain of MotB using site directed mutagenesis[66]. She postulated that MotA and MotB form a stable complex in the membrane, however, MotB cannot attach to peptidoglycan in this conformation and the channel is blocked until it interacts with the flagellar

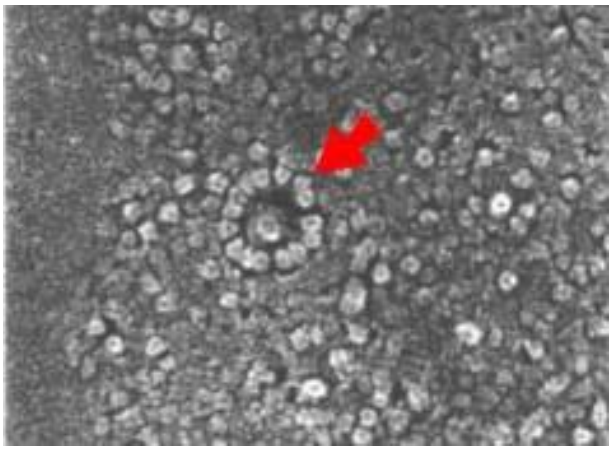

Figure 1.12: Freeze fracture image of the MotA MotB stator units in the membrane. The arrow indicates the ring. Figure from Khan *et al.* [64].

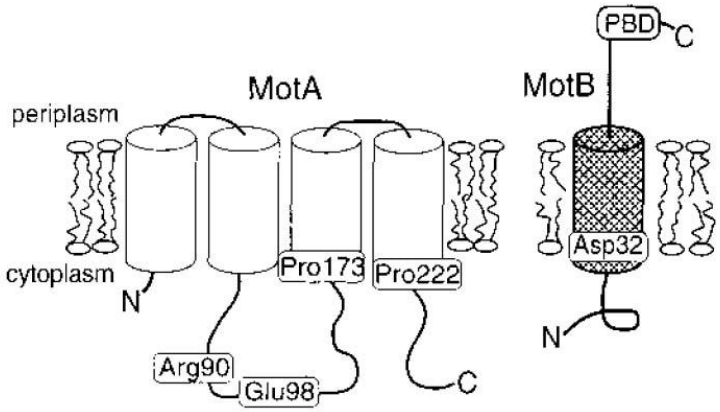

Figure 1.13: Membrane topologies of MotA and MotB proteins. Functionally significant residues are indicated. Figure from [65].

motor possibly when MotA makes contact with the C- and or MS-rings. MotB also contains a single conserved Asp acidic residue, Asp32. The two thirds of the MotA protein found in the cytoplasm contains three functionally important charged residues, which appear to act collectively as a group. Similar groups of conserved charged residues are also present in FliG in the rotor. Figure 1.14 illustrates the significant residues in MotA, MotB and FliG and their possible function [45].

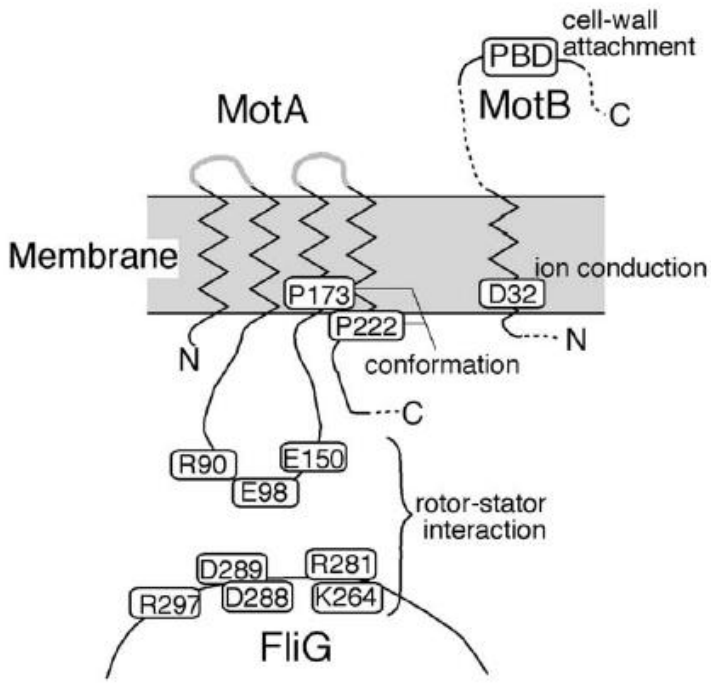

Figure 1.14: Functionally important elements of MotA, MotB and FliG, indicated by mutational studies. PBD is the peptidoglycan-binding domain. Figure from [45].

A strain with MotB replaced by green fluorescent protein (GFP) labeled MotB, MotB-GFP, was used to investigate the turnover rates of this protein from the membrane to the motor [67]. Single fluorophores were observed with a total internal reflection fluorescence (TIRF) microscope, using photobleaching to highlight incoming GFP molecules. Stator units were found to have a turnover rate of $0.04s^{-1}$ with an average dwell time of only half a minute in the motor.

The structure of the spirochaete *Treponema primita* flagellar motor was obtained recently from electron cryotomography [68], and is of interest for comparison with the flagellar motor of *E.coli*. It is slightly larger than that of *E.coli* and as such, structural features are more obvious. Interaction between the stator and the C-ring might occur at the top of the C-ring, as is postulated in *E.coli*, the two components touch here, see figure 1.15. Also evident from the study was a definite 16 fold symmetry of the stator studs. The number of stator units in the *E.coli* motor has been contested and currently lies at 11 or greater[61].

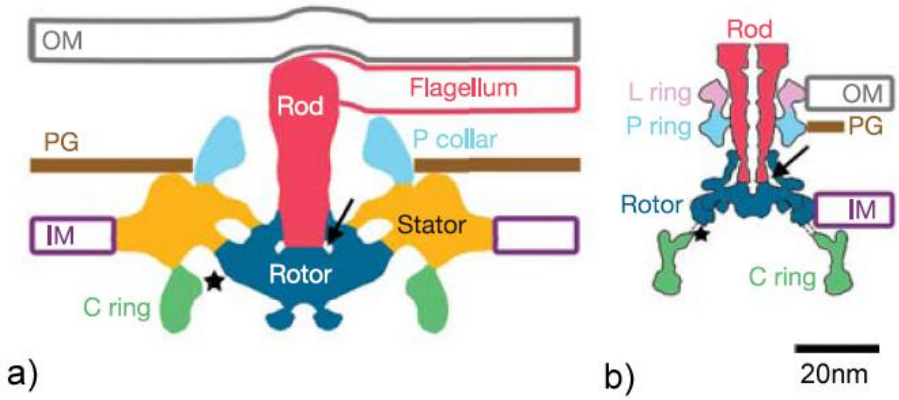

Figure 1.15: Comparative diagrams taken from freeze fracture images of the *Treponema* and *Salmonella* motors. a) Cross section of the *Treponema primitia* motor, b) cross section of the freeze fracture image of the bacterial flagellar motor of *Salmonella*, where the diagrams are on the same scale. Figure from [68].

1.4 Techniques to study the flagellar motor

Tethered cells

The standard technique to study the motor, used for many years and in all previous electrorotation experiments, is the tethered cell assay. Cell tethering involves the attachment of a single filament to a glass surface so the rotation of the cell about this tether point can be studied [69]. Cells expressing a sticky filament gene will attach spontaneously to glass. As the cell is approximately 3μm $\times$ 1μm the load and drag on the motor is much larger than in free swimming, so the motor operates in the high load, low speed regime. A filament that would rotate at 100Hz un-hindered now rotates at around 10Hz.

Latex beads

The bead assay was developed by Ryu *et al.* [70]. Instead of the cell rotating about a tether point, the cell body was fixed to a glass surface and a latex bead attached to one filament. Filaments are genetically modified to be hydrophobic. These sticky filaments are sheared off leaving a short hydrophobic stub. The cell body is attached to the glass by means of a layer of positively charged polylysine, which bonds to the negatively charged cell. Latex beads are washed over the carpet of cells and attach to the sticky filament stubs. The viscous load on the motor depends on the orbit of the bead and its diameter. The load on the motor can therefore be controlled by varying the diameter of the bead.

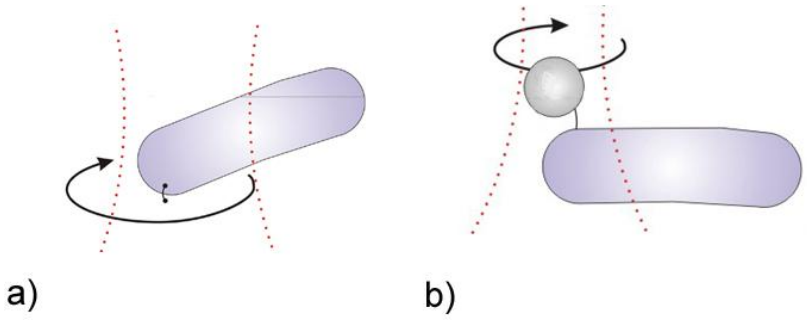

Figure 1.16: a)A tethered cell; the cell body rotates about a filament b) a bead on cell; the cell is fixed to the glass surface and a bead rotates attached to a free filament

Resurrection

Motors without functioning stator units do not rotate. Silverman *et al.* found that rotation could be restored in *mot* mutants by expression of the wild type genes [71]. Block and Berg were able to induce production of wild type MotB and observe an increase in rotation rate from non swimming to wild type speeds [59]. They coined the term resurrection for the successive incorporation of torque generating units to restore rotation rate. Step increases in speed can clearly be seen using a bead assay, see figure 1.17. *E.coli* strain WSR8 (*motA* point mutation) was grown under low induction conditions in $5\mu M$ isopropyl β-D-thiogalactopyranoside (IPTG). A high concentration of inducer ($1mM$ IPTG) was added to a bead assay of the cells and the rotation rate of the bead observed. The figure shows the rotation rate against time, with steps generated by a step finder algorithm super imposed. This trace shows a possible number of steps as 11, indicating the incorporation of 11 stator units into the motor.

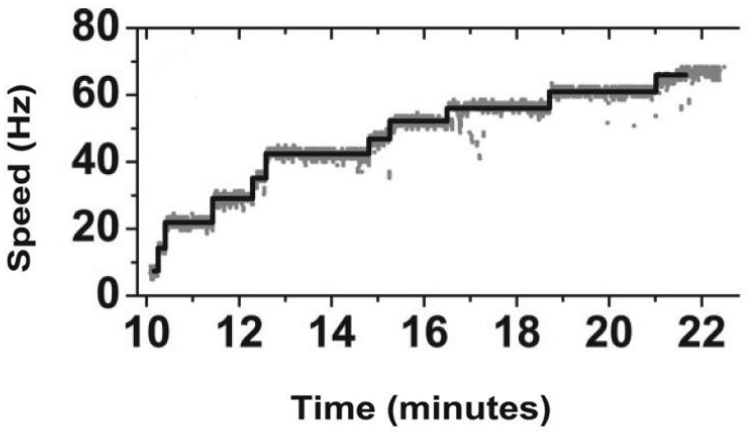

Figure 1.17: An example of a resurrection trace for *E.coli* strain WSR8. Steps, corresponding to a discrete change in speed, are found with an algorithm detail in reference [61]. These are indicated with the solid line. Figure from [61]

1.5 The application of the optical trap to biological systems

In the 1960's, Arthur Ashkin considered the application of light, and its inherent momentum, as a manipulative tool for the study of biological systems [72]. He calculated that when a particle is close in size to the wavelength of visible light, forces arising from interaction with the light are significant due to the small mass. Transfer of momentum from a coherent beam of light induces two types of force, a scattering force in the direction of propagation, and a gradient force. When a transparent object of refractive index greater than that of the medium is placed in a light gradient, such as the gaussian beam of a laser, the gradient force draws the object to the region of highest intensity, see figure 1.18 a). In 1985 Ashkin and collegues at the Bell laboratories demonstrated the trapping of a neutral dielectric particle using light alone [73]. The scattering force due to radiation pressure was overcome using two counter propagating laser beams.

Two years later, Ashkin and Dzeidzic reported that they had trapped tobacco mosaic virus (TMV) using a single beam gradient trap [74]. A high numerical aperture objective was used to focus a 5145Åargon laser. The gradient force arising from the high-angle incident light was sufficient to allow trapping using only one beam. Figure 1.18 b) illustrates the momentum transfer due to high-angle light, from a high numerical aperture objective, which allows a single beam to trap an object. Whilst observing the TMV particles, they noticed some further particles in the diluted virus sample, which were also trapped by the laser. When they observed these particles under a high resolution microscope they were identified as "*rod like motile bacteria propelled by rotating tails*" [74].

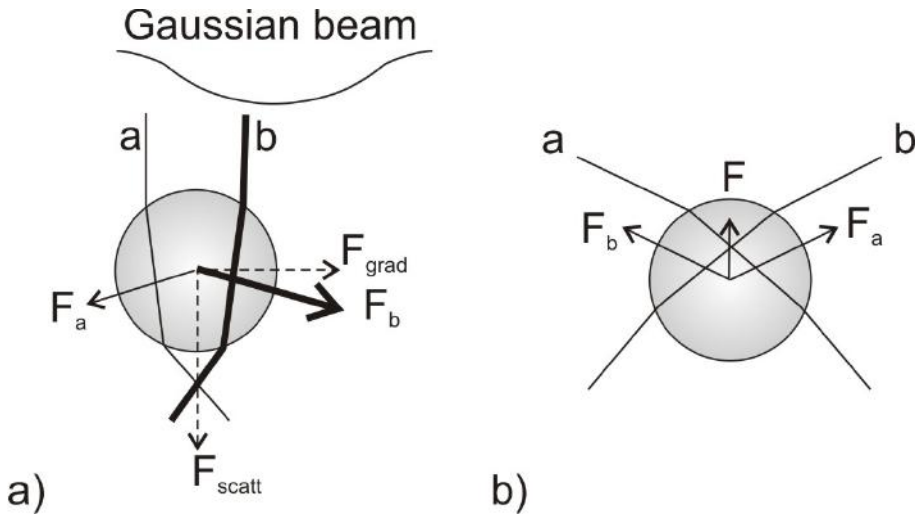

Figure 1.18: Ray diagram illustrating the gradient force. a) Light entering the object is refracted, thus transferring an equal but opposite momentum to the object. The magnitude of this momentum is proportional to the light intensity so it can be seen that a particle outside the high intensity focus of the beam will be drawn in. b) When a high numerical aperture objective is used to focus the beam, the resulting gradient is steep and the dominating force is the gradient force. This pN force is sufficient to draw dielectric objects from the size of an atom to a biological cell, to the focus of the beam, thus trapping them.

This was the first demonstration of optical trapping of bacteria. The bacteria were trapped with 50mW of power which was then reduced to 5mW to prevent the sample over heating. A mechanical stage was introduced to move the focus of the beam and thus drag the bacterium with it, demonstrating the ability of this technique to manipulate the bacterium. Unfortunately when the power of the laser was increased to the 100mW used to trap the virions, the trapped bacterium "*..apparently vented some of its contents into the surroundings*" [74].

A few months later Ashkin and Dzeidzic wrote in a letter to *Nature* that replacing the original argon laser with one producing infrared light, $\lambda = 1064$nm they were able to perform damage free trapping and manipulation of protozoa and the organelles contained within them [75]. The inspiration for prolific optical trap studies of flagellar motors, and the use of tethering as a technique, may have arisen from

Ashkin's early observation of these samples.

> "*A bacterium, while being manipulated close to the surface of a slide, would occasionally manage to attach itself to the surface with its tail and remain tethered. Under these conditions it was still possible to manipulate the particle in a circle around its tether and observe the action of the optical forces*" [74]

1.5.1 Current applications

Since Ashkin's introduction of the optical trap, its application to the study of biological systems has escalated, due to the combined ablility to apply pN forces to μm sized objects, whilst measuring displacement. The development of Piezo-electric stages has provided a means to manipulate the environment around the trapped particle, with nanometre precision. Detectors have advanced from video analysis to various methods including photodiode detection, of which there are two kinds; one is a variety of polarisation interferometry involving two incident beams split from the incoming laser, the second uses the trapping laser directly. Either the particle is imaged onto the diode, or the back focal plane of the condenser is imaged onto a quadrant photodiode and the signal used to work out the particle's coordinates.

A further development in trapping is the application of acousto-optic deflectors (AOD's) to produce multiple traps. These are crystals through which a sound wave is propagated, which acts like a variable diffraction grating. The trap is deflected so its position can be time varied, resulting in two or more traps. The position and intensity of the traps can then be digitally controlled. Alternatives to AOD's include glavanometer scanning mirrors and electro-optic deflectors (EOD's). Scanning mirrors are robust but have a slow temporal response compared to AOD's. EOD's

are crystals with alterable refractive indexes, which have a similar result to AOD's however their application has been limited due to high cost. For a review of modern optical trapping see Neuman and Block [76] or Molloy and Padgett [77].

A promising technique is the combination of optical trapping and single molecule fluorescence (SMF). SMF can be used to indicate the location of trapping forces and the trap used to align fluorescent species. One recent application was in the un-zipping of a DNA double strand, where the un-zipping was forced by the trap. Discontinuities in the fluorescent signal coincided with mechanical transitions in the DNA. It was suggested that this technique be applied in the future to study conformational changes in proteins [78].

The momentum of light can also be used to apply a torque to certain crystals. Angular momentum from circularly polarised light is used to induce a torque in trapped particles such as birefringent calcite [79]. These particles are useful to be employed as rotating handles.

A third development in optical trapping is the holographic array, where computer designed holograms are used to create a 3D array of traps from one input beam. The hologram can be digitally updated allowing the traps to move in real time. Holographic arrays have been used to transport and deposit volumes of carbon nanotubes [80]. This technique is suggested as a precise method of dealing with large quantities of the nanometre structures, with applications in nano-circuitry.

1.6 Back focal plane detection

The back focal plane method using a focused laser trap allows nanometre displacements to be measured with bandwidths up to $100kHz$ and has the advantage of working in parallel with the trap. The condenser lens collimates the laser, and as such the image in the back focal plane can be seen as a representation of the angular distribution of light exiting the specimen. Beads that are smaller than, or comparable to, the wavelength of light can be approximated as a point scatterer, and a change in the pattern of light in the back focal plane described as an interference effect [81]. For a beam waist of the order of the wavelength, the response of the detector to the motion of a particle is linear for sub μm displacements with a slope depending on $\frac{d^3}{\lambda^4}$, where d is the particle diameter and λ is the laser wavelength.

If an external force is applied to a trapped bead, it is displaced from the centre of the trap by a distance proportional to the force. This displacement is measured by projecting the laser onto a quadrant photodiode. In back focal plane detection the beam transmitted from the particle is recollimated by a condenser lens and the condenser back focal plane is imaged on the surface of the diode. The coordinates of deflection of the trapped particle are calculated from the diode signal using the following equations, where the four quadrants are labeled as in figure 1.19.

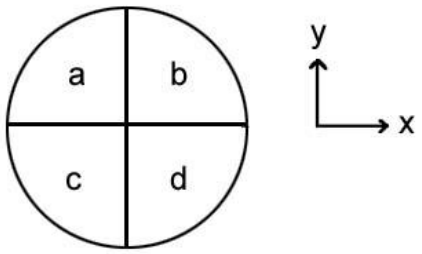

Figure 1.19: Diagram of the quadrants of the photodiode

$$x = \frac{(b+c)-(a+d)}{a+b+c+d} \tag{1.1}$$

$$y = \frac{(a+b)-(c+d)}{a+b+c+d} \tag{1.2}$$

For a particle rotating in a circle radius A at angular velocity ω_0 the coordinates can be written as $x = Acos(\omega_0 t)$ and $y = Asin(\omega_0 t)$ giving the complex signal $z = x + iy = Aexp(i\omega_0 t)$. Thus the power spectrum of the signal gives both the speed and direction of the rotation.

1.7 Electrorotation

1.7.1 Introduction to electrorotation

Arnold and Zimmerman coined the term *electrorotation* when they used 8mm platinum foil electrodes to rotate a mesophyll protoplast of *Avena sativa* [82]. The physical forces behind this phenomenon can be described as follows.

When a particle is exposed to an electric field it becomes polarised. The magnitude of the polarisation depends on the dielectric properties of the particle and the medium, such as permittivity and conductivity. Permittivity can been seen as a static measure of energy storage, or charge accumulation at interfaces, whereas conductivity is the ease with which charge can move through a material.

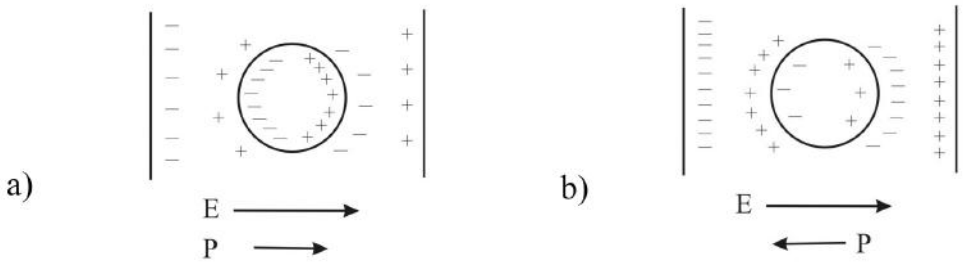

Figure 1.20: Diagrams of a particle between two electrodes. a) A highly conducting particle in a low conductivity medium is polarised in the direction of the field. b) A particle of low conductivity in a highly conductive medium is polarised in the opposite direction to the field. **P** is the polarisation vector and **E** is the electric field vector.

In figure 1.20 a) the particle has a higher conductivity than the medium, the resultant polarisation goes with the field. In figure 1.20 b) the opposite is true and the resultant polarisation of the particle is opposing the field. The polarisation vector (direction in which the polarisation lies) tends to align itself with the field. This polarisation is not instantaneous and involves movement of free charge and re-orientation of fixed charges, such as dipoles on molecules.

If the field is then rotated, the particle experiences a torque that functions to realign its polarisation vector with the field. A circularly rotating field can be approximated by applying a.c. voltage to a set of three or more electrodes, with each electrode out of phase with the previous electrode. For $n = 4$ the phase lag is $\pi/2$, see figure 1.21.

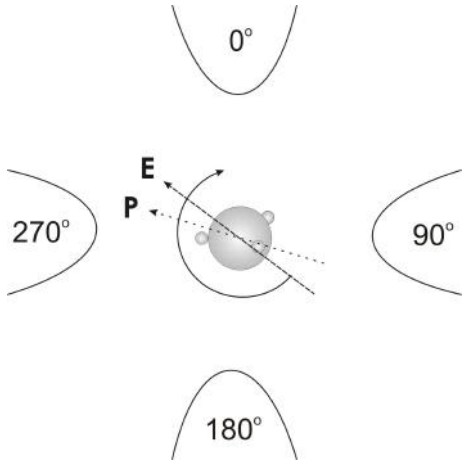

Figure 1.21: If a sinusoidal voltage is applied to a set of four electrodes, each $\pi/2$ out of phase, an effectively circular rotating field is generated. The electric field vector rotates and the polarisation vector of the particle experiences a torque to realign it with the field. In this case the field rotates anti-clockwise.

A note on frequency of rotation : At low frequencies a highly conductive particle with a low permittivity behaves like figure 1.20 a), the free charge can keep up with the changing direction of the field. However at high frequencies this is no longer the case and polarisation of bound charge, or permittivity, dominates. Frequency spectra can give useful information about the particle that is rotating, for example, Huang *et al.* used a polynomial electrode design to manipulate yeast cells using dielectrophoretic forces and electrorotation [83]. They explored the difference in electrorotation spectra between viable yeast cells and heat damaged cells. They were able to show that the spectra for viable yeast cells was markedly different to

that of the damaged cells, despite the lack of visible difference between the two types of cell. It was possible to reproduce the data using a multi-shell model. For further studies see section 1.7.3.

1.7.2 Modeling the electric field

In an attempt to understand and model the behaviour of particles in an electric field, Huang and Pethig looked to define a simple geometry for the electrodes [84]. They used Laplace's equation to describe the shape of a set of polynomial electrodes, where the electrodes were defined according to equipotential lines, see figure 1.22. The defined geometry is approximate to that in figure 1.21. As the polynomial electrodes provide a simple solution to the Laplace equation, these have become a standard for the rough shape of a set of electrodes. Experimentally, Huang *et al.* flowed a suspension of yeast cells over the electrodes. In the case where the suspending medium had a relatively low conductivity of $4\mu Scm^{-1}$, the cells experienced dielectrophoresis directed towards the electrode edges. In the case of a higher conductivity of $170\mu Scm^{-1}$, the cells experienced dielectrophoresis towards the region in the centre of the electrodes, at the minimum of the potential well.

A charge density method was implemented by Wang *et al.* to model the electric field generated by the polynomial electrodes, and is detailed in reference [85]. Wang predicated and demonstrated the separation of a mixture of viable and non viable cells using dielectrophoresis. Consequently, Hughes *et al.* were able to model the vectorial electric field and the spatial variance of torque in the vicinity of a set of polynomial electrodes by combining the work of Huang and Pethig, and Wang [86]. Hughes *et al.* then went on to measure the spatial variation of electrorotational torque, in order to verify their previous numerical simulation [87]. The simulation

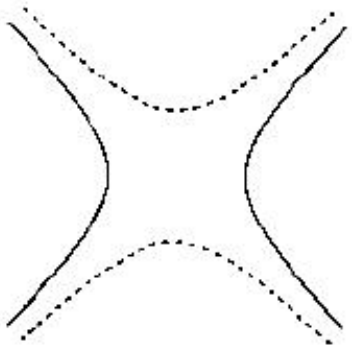

Figure 1.22: The geometry of a set of polynomial electrodes with $n = 2$, where the number of electrodes with each polarity is equal to n. Dashed lines represent negative polarity. From [84]

suggested that both the magnitude and the phase of the electric field varies significantly across the electrodes.

1.7.3 Biological studies using the electrorotation technique

Electrorotation can be used both to orientate a particle [88] and to study its internal constituents [83, 89, 53, 90]. Although this project is concerned with electrorotation purely as a handle to rotate the flagellar motor, the rotation spectra of a particle can also be used to provide information about that particle. The electrorotation spectrum of a particle displays features, characteristic of the dielectric properties of the particle. The internal structure of a particle can be approximated and electrorotational behaviour predicted by both compartment models [91]and multi-layer shell models [83].

For example, Georgieva *et al.* used electrorotation to determine the permeability of capsules templated on red blood cells [90]. This study illustrates how the conductive and dielectric properties of the internal and external medium affect

electrorotation. The capsules formed permeable to macro-molecules, and it was intended to demonstrate that they would function as a drug delivery agent, to be loaded with a chemical and then sealed. Consecutive layering of a cross linking compound (polyallamine hydrochloride) on to red blood cell templates reduced the permeability of the membrane until the capsule was impermeable. Electrorotation spectra of the capsule before and after layering demonstrated this change in permeability. The behaviour was predicted by single and double shell models. Confocal and Scanning Force Microscopy images showed thickening of the particle wall, but an electrorotation spectrum was able to conclusively demonstrate that an individual particle was sealed after the treatment.

Electrorotation has also been used extensively to study microorganisms such as parasites. Each spectrum of an individual particle is unique due to the dielectric properties of the internal media, the organelles contained within the organism and the properties of bounding membranes. Dalton *et al.* gives a nice review of electrorotation applied to pathogenic species [92]. He suggests that the technique is a particularly useful tool for the identification and analysis of visually similar microbial pathogens. Walderich *et al.* were able to experimentally distinguish between non-invasive *Entamoeba dispar* and the morphologically identical invasive *Entamoeba hystologica* from their electrorotation spectra alone [93]. Gimsa *et al.* claimed rotation of the smallest pathogenic particle, a virion [94].

Differing detection techniques for measuring rotation rates also exist, which can be compared to the back focal plane technique used in these experiments. Common in more recent experiments is the Micro-Optical Single Particle Dynamics (MOSPAD) detector, developed by Reichle *et al.* and used by Mietchen *et al.* [95, 96, 97]. The modulation of light through a slot is measured to track the particles rotation

rate. This method suffers from a lack of freedom with the position of the slot, which is fixed, and they rely on particles which are relatively large at $13\mu m$. The maximum time resolution quoted was 0.02 seconds. The MOSPAD detector was used to obtain rotational spectra for a number of cells in octopole cages, in planar electrode slides and to investigate the dependence of electrorotation on temperature.

As well as a diagnostic tool, electorotation also has its applications as a manipulative tool in biology. The experiments detailed in this thesis involve using electrorotation as a handle to rotate the bacterial flagellar motor, electrorotation has been used purely to rotate particles in studies such as those of Park *et al.* [88]. Park *et al.* designed and fabricated a processor chip for single embryo-cell manipulation. *In vitro* fertilisation is a technique that requires precise orientation of an ovum cell for insertion of genetic material. Technicians train for one to two years in cell handling. Here electorotation is incorporated into a Lab-on-a-Chip device and proposed as a technique to orientate the cell. The voltage and frequency of the electrorotation can be tuned so that the cell is rotated at a few radians per second, allowing accurate positioning of the cell and removing the need for invasive manipulation. The device is tested on viable ova, which were shown to divide as normal after rotation. This demonstrates the non invasive nature of electrorotation and its usefulness for the study of biological specimens.

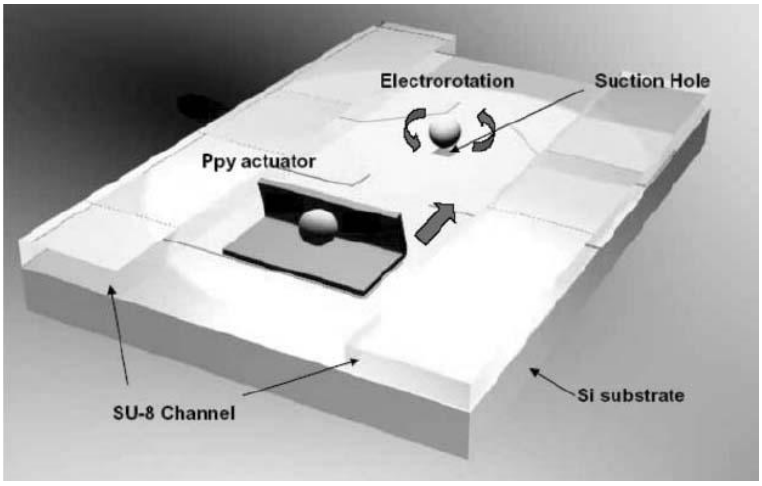

Figure 1.23: A schematic diagram of the device of Park *et al.*. The ovuum cell enters at the Ppy actuator (a valve) where one cell passes through, then the valve is closed. The cell is moved to a micro-hole in the centre of the electrodes, by suction. The cell is then non invasively re-oriented by low power electrorotation, to the correct angle for injection. Figure from [88]

1.7.4 Electrorotation of the flagellar motor

Electrorotation experiments to date have produced a characteristic torque speed curve for the flagellar motor, with much of the foundation work being carried out in the laboratory of Howard Berg. Berg and Turner [98] were inspired to apply an external torque to the motor to test the model of motor function of Meister *et al.* [99]. Meister suggested that tightly coupled models of motor function produce similar torques when the motor is stalled but vary greatly at high speeds. Berg and Turner [98] used Washizu's four electrode method [100] to generate a rotating electric field with which to spin a tethered bacterium. They studied two strains of *E.coli*, one wild type for chemotaxis and one a *cheY* deletion that rotates solely CCW. The flagellar filaments were sheared to enable the cells to bind by hydrophobic interaction, via the filament stub, to the surface of a treated sapphire window, used to reduce local heating. The window then forms one surface of a flow cell allowing different solutions to be passed over the bacteria. A cell was placed over the 70μm gap micro-electrodes. An alternating current in the electrode pairs generated the rotating electric field at 2.25MHz. Rotation of the cell about the tether point was monitored using a linear gradient filter.

Berg and Turner's detector was designed as follows. Light emerging from the back of the objective lens of a phase contrast microscope was split into two beams. Each beam was imaged onto a linear-graded filter. The filters were set at right angles to each other so that one corresponds to a y signal and the other x, see figure 1.24. As the cell rotates the intensity of the light varies as sine and cosine functions. The transmitted light is imaged on a photomultiplier.

A high conductivity buffer was chosen as higher torque could be generated and also fewer cells accumulated at the electrodes. Cells gathering at the electrode tips

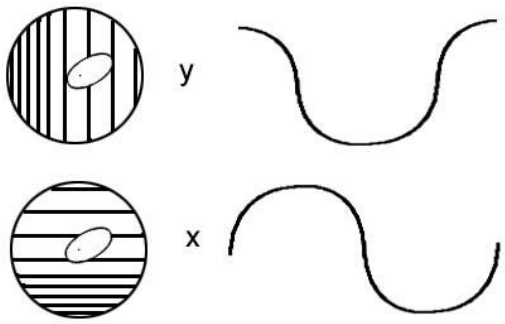

Figure 1.24: Diagram of the operation of the two linear gradient filters for x and y with the bacterial cell imaged on their surface. The transmission of the x filter increases linearly from left to right, and the y filter from bottom to top. The intensity of the transmitted light varies as indicated on the right, as the bacterium rotates.

were seen to cause a transient increase in speed of the rotating body possibly due to leakage of charge from the bacteria. Choice of the high conductivity buffer increases torque but also generates local heating, hence the use of the sapphire window.

A speed offset, equivalent to the torque generated by the motor, was defined as the speed of the cell rotating with a working motor, minus the speed of the cell rotating with a broken motor. This was measured by first spinning the cell at increasing torques, then catastophically breaking the cell motor and repeating the measurements. It was assumed that resistance of the motor after breaking is negligible, compared with the viscous drag on the cell. The speed offset plots showed a constant torque generated by the motor up to about 100Hz. To find the zero torque speed the motors were driven at various low temperatures and also at higher speeds. At room temperature the zero torque speed was found to be of the order of 300Hz in the CCW direction. As the speed was increased the motor torque dropped linearly to zero, beyond this point the motor resisted rotation. See figure 1.25.

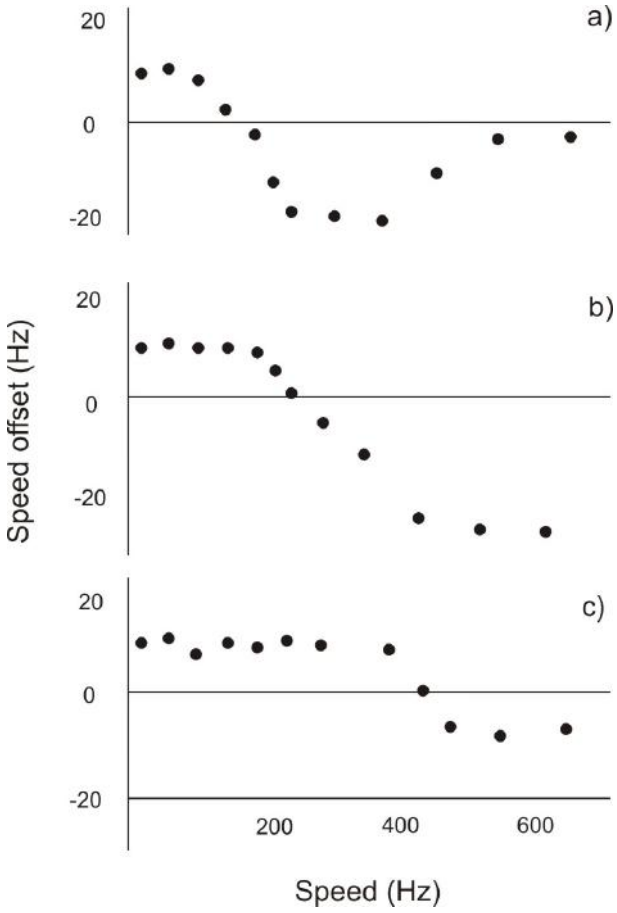

Figure 1.25: Speed offsets obtained by Berg and Turner [98] for cells at a) and b) 11.2°C and c) 22.6°C

Berg and Turner also found a substantial barrier to backwards (CW) rotation and in some cases, breaching of this barrier lead to catastrophic breaking of the motor. The motor could also be broken progressively by switching rotation repeatedly. This effect was short lived however and the motors often revived. Cells resisting CW rotation did not stop completely but turned very slowly.

Khan and Berg had previously examined motor behaviour at low proton motive force (pmf) by de-energising cells [101]. At low rotation rates they found barriers to rotation that were spatially periodic, with a six fold symmetry. Above a threshold speed, variations in rotational period were attributed to free Brownian motion. Khan concluded that the flagellar motor determines torque, not angular position

and that Brownian motion occurs between torque generating events. Conversely, Berg and Turner found that motors stalled by the application of external torque, would creep backwards at rates as low as one revolution in 12 minutes [98]. This would imply a lack of freedom which conflicts with Khan and Berg's results. Samuel and Berg measured the dependence of fluctuations in rotation rate on the mean rotation rate, using electrorotation [102]. They showed that the rotor does not diffuse and predicted a Poisson stepping mechanism with approximately 400 steps. More recently direct observation of steps in a sodium driven *E.coli* chimaera produced a value of 26 steps per revolution, consistent with the periodicity of FliG [103].

In an attempt to understand the torque barrier, Berry *et al.* [104] investigated backwards rotation of the motor and observed cells before, during and after breaking. *E.coli*, wild-type for chemotaxis, were rotated under varying applied torques. The collective data for cells spun repeatedly were plotted. The torque-speed curves were found to be symmetric for both directions of rotation. A barrier was evident in both switching from CCW to CW and vice versa. The experiments on CCW mutants performed by Berg and Turner [98] were repeated to study more closely the process of catastrophic breaking. Cells were broken by applying steadily increasing torque in the CW direction. The motors generated constant torque as they were driven to stop, then approximately 2 to 3 times this value of torque was required to turn the motor backwards. This torque remained constant until the motor broke, when it ceased entirely. It was postulated that the high torque necessary to change the motors direction of rotation was sufficient to break a component of the motor that does not regenerate. Motors broken progressively were seen to recover in steps, similar to those seen in genetic resurrection experiments. This indicated that this form of breaking affects the individual torque generating units. It was shown that the motor also generates a constant torque when driven backwards. The ratio of

maximum torque to stall torque was found to vary considerably among bacteria, raising questions regarding the assumption that a broken motor generates negligible frictional torque. They concluded that the apparent barrier to backwards rotation pointed to a tightly coupled model of rotation and proton flux.

One year later Berry *et al.* re-evaluated their results [105]. Although a barrier to backwards rotation was probable, there were some inconsistencies between the observed behaviour and the theory that predicted a barrier to backwards rotation.

- Cells stalled at particular angles, often at two angles 180° apart.
- Cells which were stalled, then ER removed, would often rotate slowly or not at all, for a second or two.

This lead Berry *et al.* to look for another explanation for the observed barrier. Reconsidering the previous data whilst taking into account spatial orientation of the rotating bacterium, they were able to explain the apparent barrier as an artifact due to angular variation of torque. It was concluded that the source of this angular variation may be irregularities in the applied field. However, these electorotation experiments were not able to discount internal angular variation in the motor.

Berry and Berg confirmed experimentally the absence of the barrier to backwards rotation using optical tweezers [106]. A rotating cell was stalled by an optical trap, then the cell was rotated in both directions using a piezoelectric stage. The force generated by the cell was calculated from the displacement of the cell in the trap. The motor torque was approximately constant in both directions regardless of angle. This was repeated with a trapped bead attached to the motor filament and the results were in agreement. The new conclusions were then interpreted using a simple kinetic model [107]. The previously obtained data were split into subsets

according to angle. The angular dependence was removed and torque-speed relationship estimated by considering each angle separately.

1.8 The relationship between motor torque and speed

The torque speed graph obtained by Berg and Turner [98] is shown in figure 1.26 and displays the basic features of a wild type motor rotated in one direction only. The motor operates at near thermodynamic equilibrium and is highly efficient at low speeds producing a constant torque over a range of speeds. Beyond a certain speed, known as the 'knee' value, the torque declines as a result of limiting rates of proton transfer. The torque speed curve is often plotted as a speed offset, see section 1.7.4 for details of the speed offset.

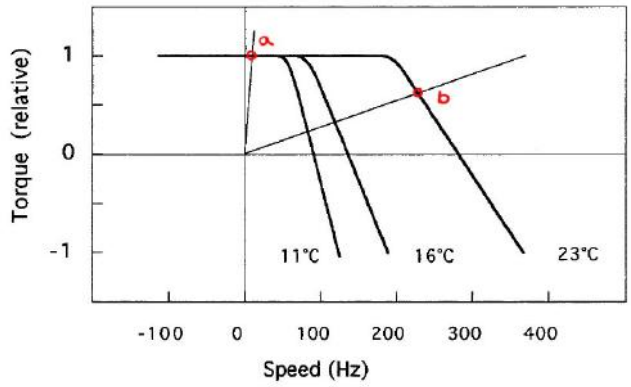

Figure 1.26: Summarising graph of the results of Berg and Turner [98]. a) a large tethered cell b) a tethered small cell. Figure adapted from [44]

The torque generated by the motor has been estimated at between 2700pNnm [108] and 4600pNnm [106]. Torque, τ is equal to the drag coefficient, f_{drag}, of the load, multiplied by the angular rotation rate, ω ($\omega = 2\pi f$ where f is the speed offset).

$$\tau = f_{drag}\omega \tag{1.3}$$

The drag coefficient for a sphere of radius r in medium of viscosity η is

$$f_{drag} = 8\pi r^3 \eta \tag{1.4}$$

Information for the torque generated by the flagellar motor at varying speeds has been gathered using various techniques. Berg and Turner plotted the first torque speed curve for *E.coli* in 1993 using the electorotation technique and rotating cells about a tether point [98], as detailed in section 1.7.4. The experiments of Berry and Berg ruled out a thermal ratchet mechanism and their measured torque speed curves could point towards a conformational change at the heart of the torque generation process [105, 107].

The initial results of Berg and Turner were confirmed by Chen and Berg [109], who altered the viscosity of the surrounding medium in which the cells were suspended, using the viscous agent Ficol. Points on the curve were obtained by increasing the viscosity, see figure 1.27 a), speeds were measured by monitoring the rotation of a bead attached to the filament of a tethered cell, thus reducing the variation in size and shape of the motor load. The dashed red line represents a load line for a bead in a viscous medium with added Ficol and the plain blue line represents the same bead in water. A load line is the straight line through the origin that corresponds to the torque required to rotate an object of fixed size in a viscous medium. The line is described by equation 1.3. The point obtained for the bead in water marks a maximum speed at which a measurement can be taken, with out applying an external torque.

Results were plotted at 22.7° 17.7° and 15.8°, see figure 1.27 b). The point where the constant torque regime ends, and the motor starts to resist the external torque, was estimated using the intersection of two separate linear regressions on the data.

Data from a single cell was plotted, see figure 1.27 c).

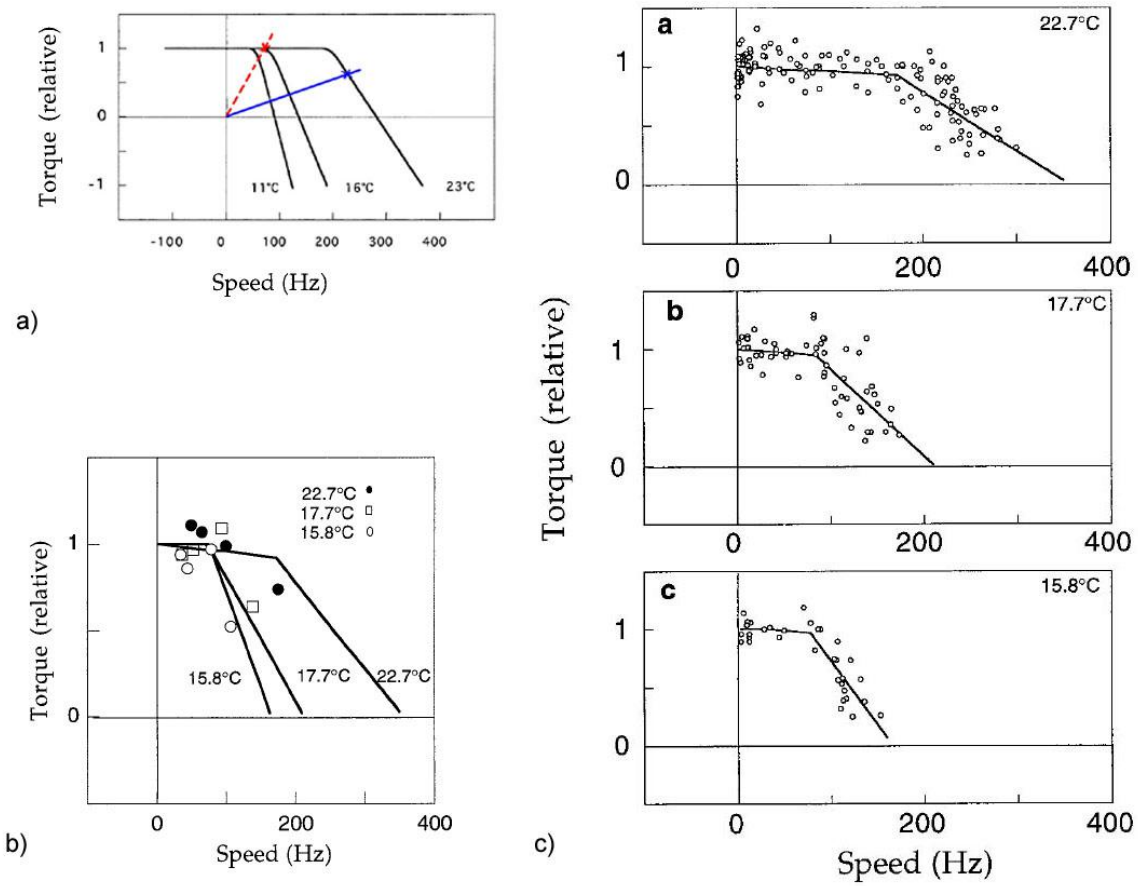

Figure 1.27: a) Altering the viscosity of the medium by adding viscous agent Ficol allows points to be plotted (marked with a cross) from the least viscous; water (blue plain line), in steps of increasing viscosity, to a maxiumum viscosity (dashed red line). Figure adapted from [44] b) Torque speed data for a single cell at 22.7°, 17.7° and 15.8°. Figure from [109] c) Torque speed data for all cells, i) 30 cells at 22.7° ii) 14 cells at 17.7° and ii) 11 cells at 15.8°. Figure from [109]

Ryu, Berry and Berg were able to obtain information on the torque speed curve of *E.coli* for differing stator numbers [70], from one to five. Varying the stator number in the motor was done by resurrection, see section 1.4. Points on the torque speed graph were plotted by altering the size of bead attached to the filament. This allowed a speed to be measured for a range of loads, see figure 1.28. At high load/low speeds, the increase in speed is linear with torque generator number, however, at low load/high speed, the speed saturates as the torque generator number increases, implying the motor has a high duty ratio. The duty ratio of a motor protein is a measure of how long the protein is bound to its substrate. At high speeds the effect of the duty ratio of the stator units becomes obvious, whereas at low speeds the time the stator units spend bound to the rotor is not the rate limiting factor in rotation speed. If the duty ratio is high then an increase in torque generator number at high speeds, low load, will limit the speed of rotation, however if the duty ratio is low this affect will not be seen. The duty ratio of the stator units can be compared to classes of kinesin, which are high duty, and myosin, which tend to be low duty, and their mechanisms compared. In conclusion, Ryu *et al.* determined that each stator unit binds to the motor for the majority of its mechanochemical cycle.

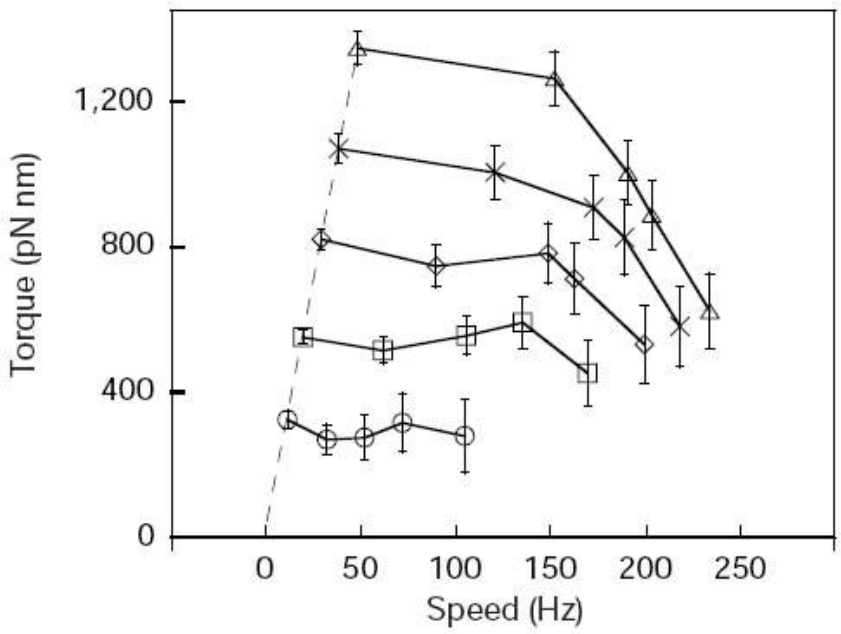

Figure 1.28: Torque speed curves with one (bottom) to five (top) torque generating units. Figure from [70]

To find the effect of proton motive force (PMF) on motors in low and high load regime, two motors on the same cell were measured by Gabel and Berg [110]. A tethered cell was rotating around its filament, this rotating cell was also decorated with a bead, attached to a second filament. Therefore one motor was rotating under high load, and the other under low load, see fig 1.29 a). The rotation rate of the high load was used to indicate the PMF, as these were previously shown to be proportional. The respiratory poison sodium azide was added in one experiment, and the uncoupler carbonylcyanide m-chlorophenylhydrazone (CCCP) in a second. This caused the PMF to be disrupted and the motor to run out of its energy source. The speed of the motor with high load was plotted against that of the motor with low load. These were found to vary linearly, see figure 1.29 a). Gabel and Berg found that the motor's rotation rate remained proportional to the cell's PMF regardless of speed. If the speed varies linearly with PMF, the torque speed curve should also scale linearly with PMF, see figure 1.29 b).

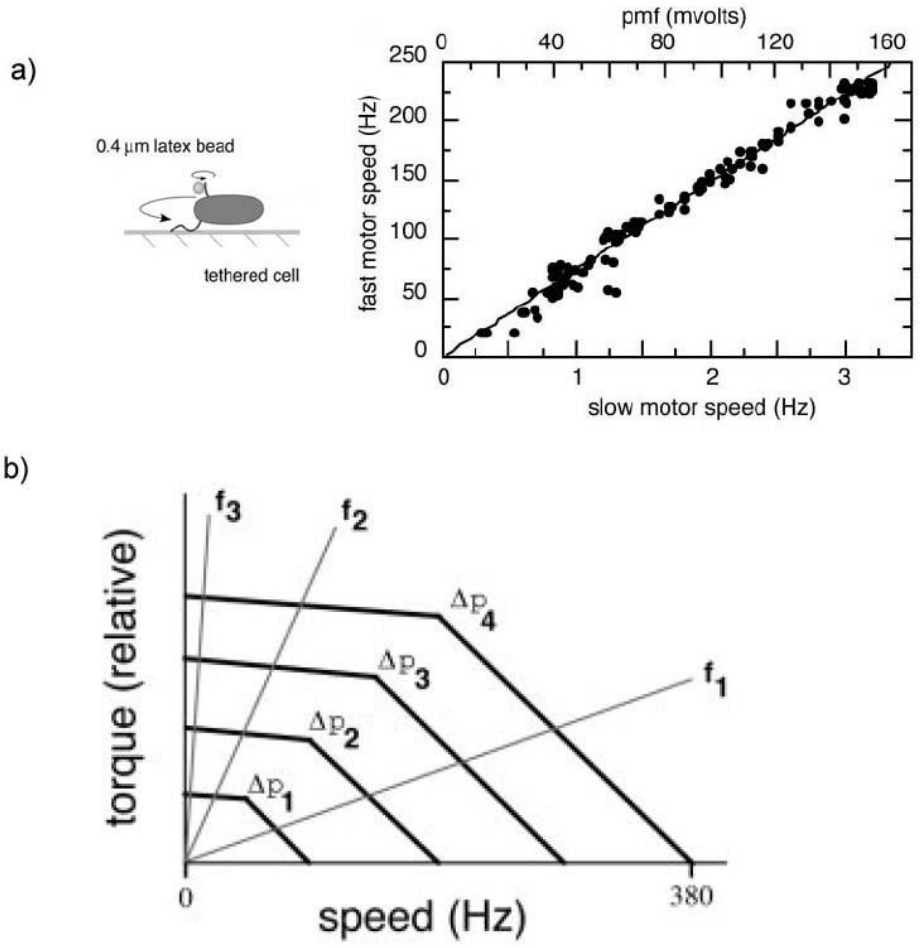

Figure 1.29: The results of Gabel and Berg. a) The results for the same bacterium plotted with fast motor speed versus slow motor speed. The cell was gradually de-energised by the addition of sodium azide. The illustration depicts a cell with one motor under high load and one motor under low load. b) Qualitative torque speed curves for varying PMF, implied by the data. Figure from [110]

1.9 Models of the mechanism of the flagellar motor

1.9.1 Physical models

Early models of motor function could be divided into the 'turnstile' model of Khan and Berg [111], the electrostatic 'turbine' model described by Läuger [112] or Berry [113], and Läuger's second model, the 'crossbridge' model [114]. The former is based on a thermal ratchet and latter two are both based on a power stroke mechanism.

Studies have since discounted the possibility of a thermal ratchet and the mechanism looks to be a power stroke, most likely involving a conformational change, most similar to Läuger's crossbridge model. The crossbridge model of Läuger [114], involves a conformational change similar to that of linear molecular motors such as kinesin. Here, proton binding in the stator induces a conformational change that exerts a torque on the rotor. Release of the proton reverses the conformational change and the stator returns to its initial position. This is a tight-coupled model where binding of the proton and torque generation can be seen as one process.

Linear motor proteins tend to function through a conformational change and it is sensible to assume that there is a possibility that the flagellar motor also has this mechanism at the heart of its operation. Blair is in favour of conformational change and proposes a cyclical mechanism, where the proton enters the stator unit from the periplasmic space and binds to one site in the stator unit [45] [115]. This induces a conformational change that exerts a force on the rotor, and closes the channel, forcing the proton to exit into the cytoplasm, see figure 1.30. Blair suggests that the MotA and MotB proteins are arranged as in figure 1.31.

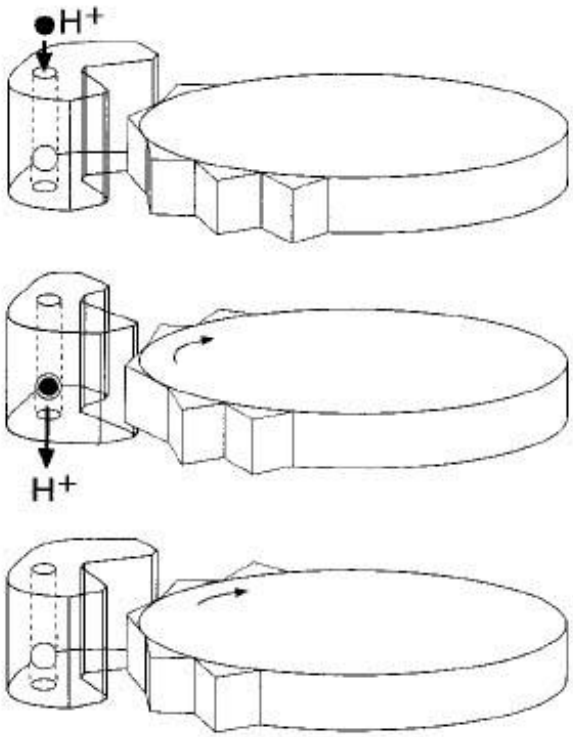

Figure 1.30: Proposed model for the role of the stator conformational change in torque generation. The proton binds to the stator and induces a conformational change, this applies a force to the rotor and drives rotation. The proton then exits the channel and the stator returns to its previous position. Figure from [115]

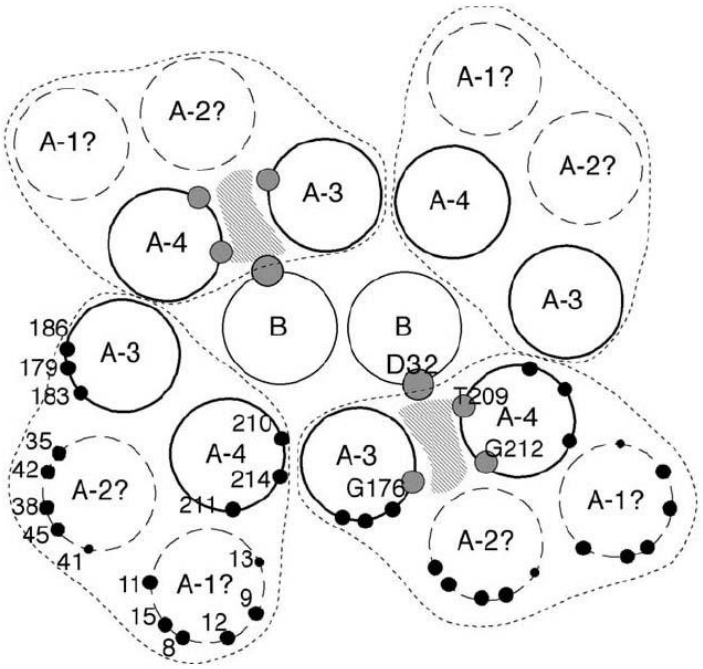

Figure 1.31: Blair's suggested arrangement for the $MotA_4B_2$ unit, as viewed from the periplasmic side of the membrane. Data supporting this configuration has been obtained by cross linking studies and as such most of the information is from the inner cytoplasmic halves of the channels. The Asp32 residues for MotB are shaded grey and labelled D32, there is most likely one per channel. Each proton channel is indicated by the cross-hatched area. Three conserved residues that may face into the channel are indicated by the smaller circles. Black circles indicate where tryptophan replacements were tolerated. Figure from [45]

Schmitt also favours a conformational change, in this case his theory is based on the action of the well characterised KcsA K^+ channel [116]. Rotation of the four inner transmembrane helices in KcsA open and close the central channel, see figure 1.32 a). The four inner helices are depicted in dark grey and four outer helices in light grey. Schmitt suggests that the four MotA and two MotB transmembrane helices of the flagellar motor are arranged to form a pentameric channel, see figure 1.32 b), which gates by rotating in the same manner as the potassium channel. The arrangement of MotA and MotB helices that could form such a channel is illustrated in figure 1.33. Viewed from the cytoplasm there are two pentameric channels. Each channel is formed from a single MotB helix, numbered 5, and four inner helices from two MotA units, numbered 2 and 3. The MotB helices each contain the protonatable Asp residue and are arranged so that there is one per channel.

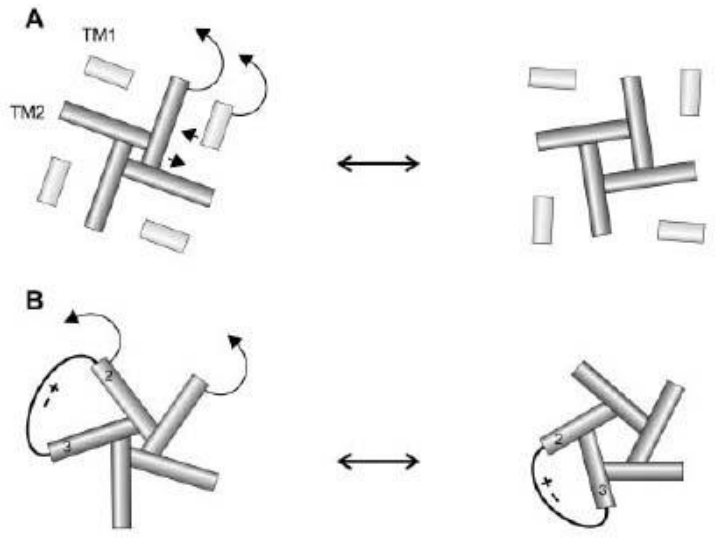

Figure 1.32: Representation of the gating mechanism of the KcsA K^+ channel, a), and the proposed MotA MotB H^+ channel, b). a) The position of four outer transmembrane helices (TM1) and four inner helices (TM2) of the KcsA channel, in closed configuration (left) and open configuration (right). b) The position of helices of MotA and MotB. Figure from [116].

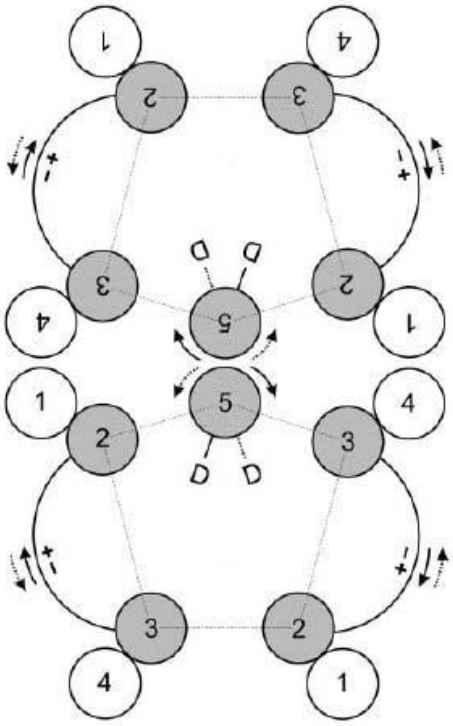

Figure 1.33: Diagram of the arrangement of MotA and MotB molecules that form two pentameric channels in the proposed mechanism. Each MotA molecule contains four helices and each MotB one. MotA helices are numbered $1-4$ and MotB numbered 5. Each MotB helix contains a conserved protonatable Asp residue, labelled D. Opening and closing of the channel rotates the residue. Forward rotation of the channel is indicated by the solid arrows and backwards rotation by the dashed arrows. Figure from [116].

1.9.2 Mathematical modeling of the motor mechanism: The model of Xing *et al.*

Approaches taken to the modelling of motor function can be divided into electrostatic [113, 117, 118] and cross bridge models [119, 120, 99]. A simple kinetic model of Meister *et al.*, involving a system where the transit of protons is tightly coupled to torque generation, was one of the first to point to the necessity for investigation of the high speed regime [99]. Further mathematical models followed on from this include the models of Walz and Caplan [117, 121] and Berry [122].

Most recently, Xing *et al.* [123] created a mathematical model that holds true for a variety of physical mechanisms involving a conformational change and is based on previous work by Xing, Oster and Wang [124, 125, 118]. Their model displays the important features of the experimentally derived torque speed curve. These are as follows; torque is constant until a knee value, whereupon it drops sharply toward zero. Below this knee value, the torque is independent of temperature and hydrogen isotope, however this changes to a strong dependence in the high speed regime. Thirdly, there is a linear dependence on proton motive force (PMF) that does not alter with speed.

Xing *et al.*'s model is based on four assumptions based on experimental evidence. It is assumed that rotation is observed via a soft elastic linker, the hook of the motor. Motor rotation and ion transport are assumed to be tightly coupled. The power stroke is driven by a conformational change, which occurs when protons bind and unbind the stator. Here, proton binding is viewed as an instantaneous process on the time scale of rotation. Finally, it is assumed that the ion channel is gated by the rotor motion.

Langevin equations to describe the behaviour of motor and the load, involving potentials of mean force, are constructed. The potential of mean force between the rotor and stator, a function of angle and conformational state, is chosen to incorporate the assumptions mentioned previously.

The action of one stator is considered. The stator can be in one of two conformations, separated by an energy barrier. The *Langevin* equations are converted into a *Fokker-Planck* probability density of the rotor and load being at position $(\theta, \theta L)$ at time t and in chemical state j. The model was then extrapolated to N stators, where the total number of states is $S = 2^N$, from this a composite potential was derived and the torque speed curves plotted for differing stator numbers. Figure 1.34 represents the trend that the model predicts. Note that one stator is predicted to have a considerably higher zero torque speed than more stators. This figure does not compare favourably with figure 1.28, showing experimental data on the torque speed curve for differing stator numbers. The trend in figure 1.34 is an example of a prediction arising from a mathematical model that can be further tested by electrorotation.

Models with tight coupled mechanisms produce the same torque at stall but vary widely at high speed [99]. It is therefore important to investigate the torque speed relationship at high speeds and low loads.

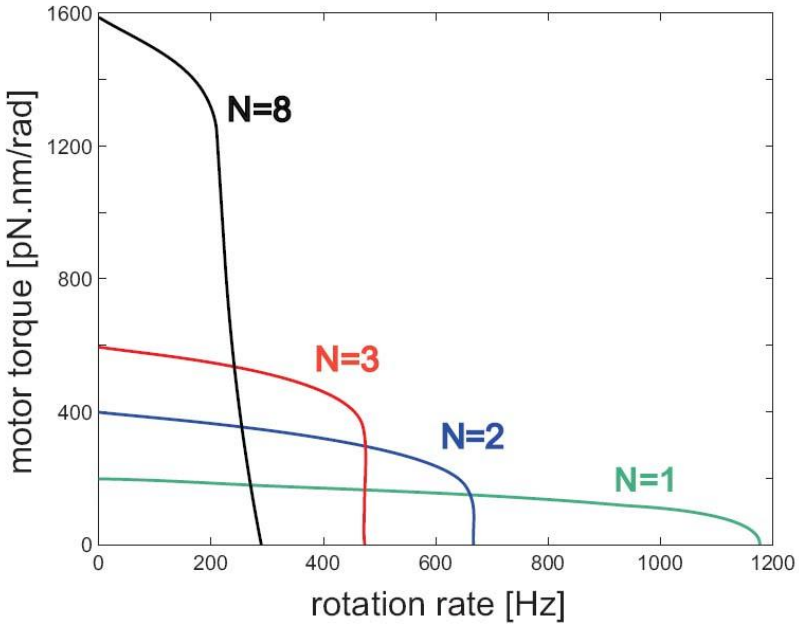

Figure 1.34: Predicted trend in the torque speed relationship for varying stator numbers, n is the number of working stators. Figure from [123]

Chapter 2

Aims

This project continues the work of Rowe *et al.*, who demonstrated the high speed rotation of trapped polarisable beads, using the back focal plane method to detect the rotation [126]. The aim is to gain information on the relationship between torque generated by the motor and the speed of rotation. Ryu *et al.* were able to plot the torque speed curve for stator numbers from 1 to 5, see figure 2.1. There is a large section of missing information, highlighted red in the figure. The results of Ryu *et al.* were constrained by the limits on the load that they were able to apply to the motor. I hope to use the electrorotation method of Berg and Turner and Berry and Berg [98, 105, 107] in combination with a polarisable bead assay to extend this graph. This will also either confirm or refute the predicted stator number trend of Xing *et al.* [123], plotted in graph 1.34 in the previous section.

To achieve this, a system for the symmetrical, high speed, low drag electrorotation of the flagellar motor must be designed. The ultimate goal is to use this system to extend the knowledge of the torque speed curve to single stator units, and compare the zero torque speed between wild type motors and low induction motors.

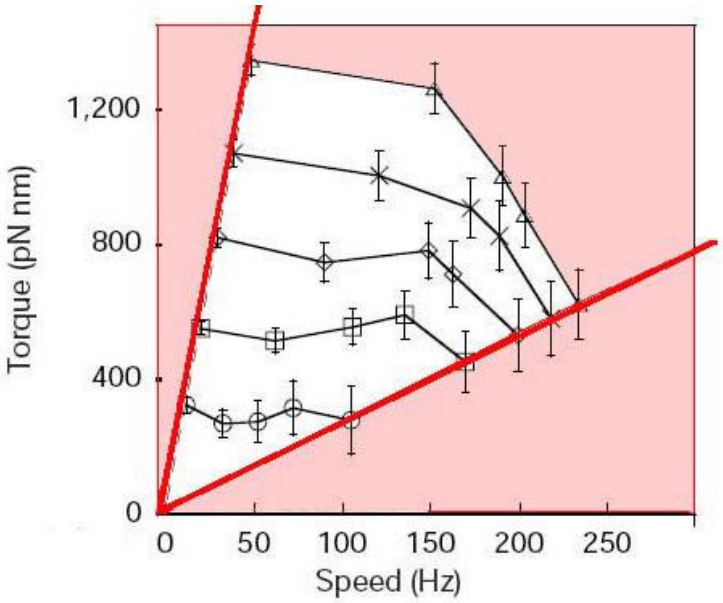

Figure 2.1: Torque speed curves with one (bottom) to five (top) torque generating units. The area beyond the red load lines, shaded red, represents the section of data that was unobtainable with the method of *Ryu et al.*. Figure taken from [70]

This information can then be incorporated into existing models for motor function, or used to formulate new ones. The method to extend the torque speed curve to high speed and single stator number is to be achieved by devising a handle to rotate the motor at speeds beyond the natural rotation rate of the motor, 100Hz. The technique chosen to do so is electrorotation. Electrorotation will be used to rotate a highly polarisable carboxy modified latex bead, 0.83μm in diameter. This is to be attached to the flagellar filament by smaller 0.2μm plain latex particles which bind to the genetically modified sticky filament strain of *E.coli* KAF95 and inducible *motA* deletion strain WSR8, figure 2.2 illustrates the method.

Aims can be summarised as follows:

- Design and build detector to measure the rotation rate of the particle (Chapter 3)
- Build flow cell that will allow loading of cells and beads for electrorotation (Chapter 3)
- Design a set of electrodes that will maximise the torque generated and provide a spherical field (Chapter 3)
- Find a suitable combination of buffer and polarisable particle that will result in maximum torque on the particle (Chapter 4)
- Reproduce previous electrorotation results with tethered cells (Chapter 5)
- Rotate a bead attached to a filament of a rotating motor at speeds beyond the zero torque speed, and measure torque generated by the motor (Chapter 6)
- Obtain data for the torque speed curve for differing stator numbers (Chapter 6)

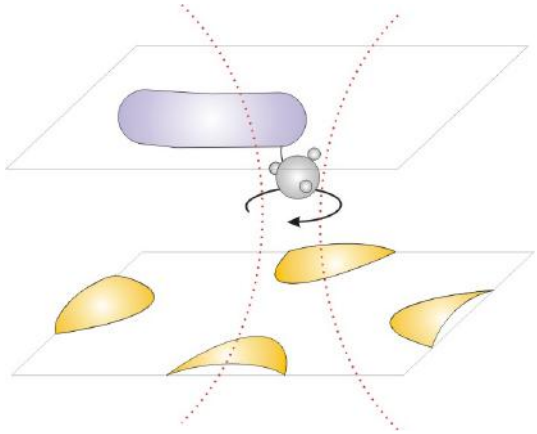

Figure 2.2: Illustration of an *E.coli* cell with a decorated bead attached to a filament. The cell is positioned over a set of four electrodes and the motion of the bead is detected using a focused laser beam.

Chapter 3

Design and Construction of a Novel Detector and Micro-Electrode System for Electrorotation

This chapter details the design and fabrication of a novel detector and micro-electrode system, for the electrorotation of the flagellar motor. The method of detection was chosen to be an optical trap to be used as an interferometer [81]. This method works well as the trap and detector are not required to work separately. It was assumed that only a weak optical trap would be required as its function is solely for position detection, and not to trap a particle with any degree of stiffness. Rotation rates will be measured over periods of time, of the order of one second, and giving speed resolution greater than one Hertz, adequate to distinguish between different numbers of stator units.

The design of the experiment requires that a suitable bacterium, tethered to the coverslip, be placed over the electrodes, which necessitates a movable coverslip. Conventional laser traps often operate using an inverted microscope, this confers mechanical stability on the objective lens, through which the trap is formed. In order to move the coverslip, which in the standard optical trap is located on the underside of the slide facing the objective, you must be able to reach it easily. Attempts by R. Berry and M. Leake to build an inverted flow cell with an independently manipulable coverslip had previously failed (unpublished). It was therefore decided to build an upright trap and microscope. As the trap is to be used solely for detection, stability should be conferred on the assembly by simplifying the optics. The resulting detector is a very simple system in comparison with current laser trap technology.

3.1 Purpose built microscope and laser position detector

In an upright microscope, the objective is free to move and the condenser fixed. There is much more vibration of the objective, however, the coverslip is easily accessible to a micro-manipulator. The design must be modified from the standard inverted configuration, to confer stability on the objective lens. It was decided that the objective would rock out of the optical path when the specimen was being placed on the stage, using a hinge. It could then be returned to its functioning position and bolted down. To achieve this the objective was mounted on a lockable dovetail x, y, z stage (Newport Spectra-Physics Ltd), and connected by a hinge to the microscope body, see figure 3.1. The optics were simplified from the standard set up to allow the upright trap to function as a basic detector. By selecting a lens specific to the back aperture of the particular objective to be used in the trap, the need for a beam

expander is eliminated. This means the number of lenses from the laser is reduced so that the optics can be suspended above the air table. However this also results in reduced flexibility of the system, as the beam is limited to one size and cannot be steered in the specimen plane. In the electrorotation set up the condenser is fixed in position and the objective lens is moved. Here the field iris acts as a marker for the objective. The number of lenses between the condenser and the quadrant photodiode is reduced by selecting a lens that images the condenser back focal plane on the diode. The lens was chosen such that the image of the back focal plane of the condenser filled the face of the diode.

A standard upright microscope was built with a 1.3N.A. 100× oil immersion objective (Nikon, Japan). Illumination was provided by a tungsten halogen lamp, and configured according to standard Köhler Illumination, a method devised to give optimum illumination of the specimen, see figure 3.2. A multimode optic fibre was positioned near the focus of the collector lens. The opposite end of the optic fibre was inserted into a translational mount to enable fine positioning of the beam. The illumination could then be directed to lens (L2 figure 3.2), which images the light source on the back focal plane of the condenser. The condenser lens collimates this light to fill the sample plane. Light scattered from the object plane is collimated by the objective and an image of the object was originally formed on a CCD (Watec) by a 200mm plano-convex lens. This lens and the objective in combination magnify the microelectrodes to fill the 8mm CCD face. This 200mm lens was then replaced by a 100mm lens and a set of three further lenses, two flipper mounted, to give the option of high or low magnification. These components were bolted on to a 0.5m aluminium tower (Thorlabs).

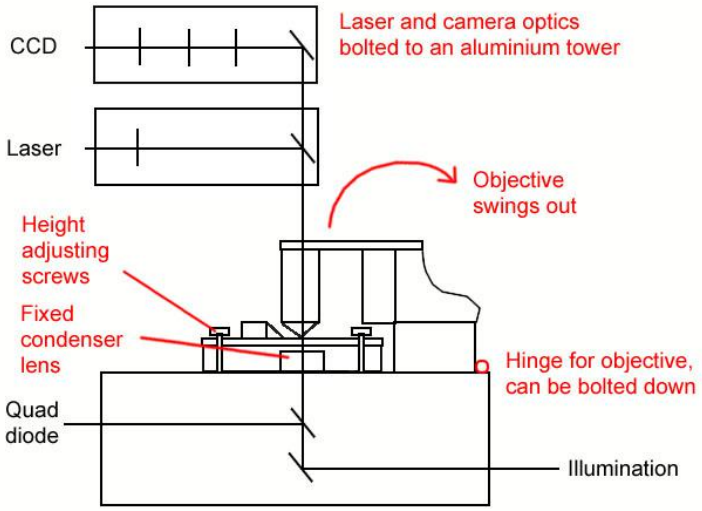

Figure 3.1: The initial design of the detector.

3.1.1 The optical detector

A 100mW, 980nm laser (Elforlight, Northants, UK) was chosen to form the trapping beam. Biological specimens tend to absorb at wavelengths below 800nm due to absorption of chromophores, such as haemoglobin and cytochrome. At longer wavelengths absorption by water becomes a significant factor, reaching a maximum at 3μm. This leaves a window of suitable wavelengths which accommodates infrared lasers [127]. The inverted trap used in subsequent sections is formed by a 1W Nd:YAG laser at 1064nm (also Elflorlight).

The bare, single mode laser fibre was cut, polished and connectorised using diamond scribe, manual polishing puck, lapping film, multimode connector and epoxy. See *Thorlabs Fiber Polishing Notes*. The connector was then mounted on a dovetail x,y,z stage. The divergent laser beam was collimated by a planoconvex lens of 50mm focal length. The beam profile was measured using a power meter and pinhole, and found to have a half angle of approximately 4.5 deg, and in combination with a 35mm lens this results in a beam width of 8.5mm. This just over-fills the 6mm back

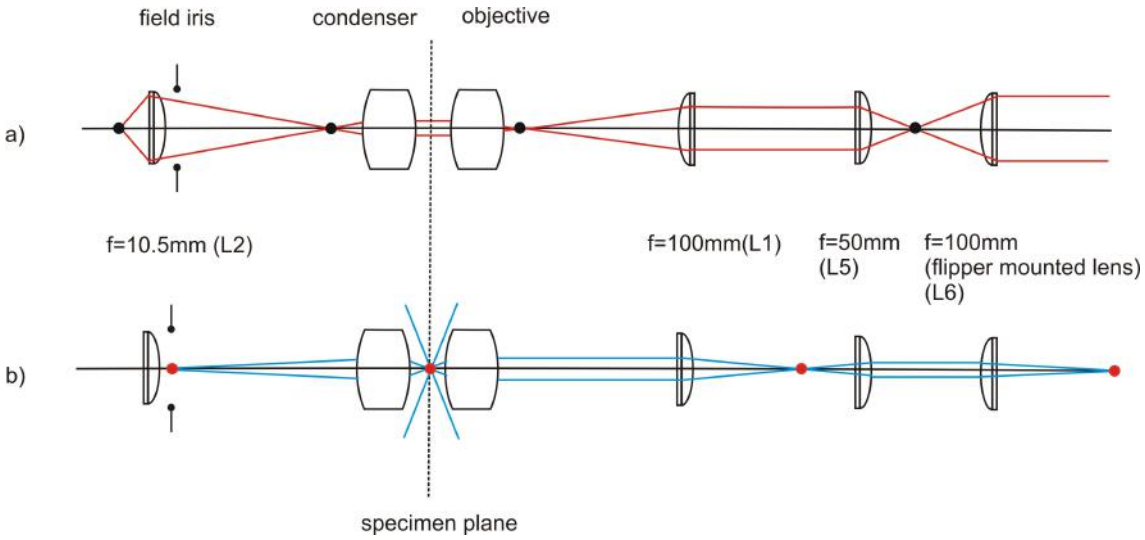

Figure 3.2: Diagram illustrating the configuration for Köhler Illumination. a) undeviated light b) light scattered by the object. Lenses L5 and L6 were added at a later date so that low magnification could be achieved. L6 is interchangeable with a 50mm lens for higher magnification.

aperture of the objective thus maximising the stiffness of the trap. The collimated beam is then directed into the objective using a dichroic mirror at 45 degrees on a kinematic mount. This is a simplified version of the standard laser trap, the telescope to adjust the beam width has been eliminated by calculation of the correct beam width for the corresponding objective. This does however mean that the beam width cannot be altered easily to accommodate other lenses or adjust the spot size of the focus. There is also no method for moving the trap in the specimen plane with out miss-aligning it, as usually two conjugate mirrors provide this option. By reducing the optics in the laser path the entire set up could be suspended from a metal plate perpendicular to the table, above the objective. The more complex the optics the more difficult it is to do this.

The high numerical aperture objective focuses the beam to a diffraction limited spot, which forms the trap. Movement of the particle in the trap is detected by imaging the back focal plane of the condenser on the quadrant diode. The con-

denser lens acts as an imaging lens for the laser focus. The image in the back focal plane (BFP) of the condenser is independent of the lateral motion of the laser focus. The pattern in the BFP represents the angular distribution of the light that has passed through the specimen. As a particle in the focus is displaced, the angular intensity distribution changes, where intensity changes are due to interference of the scattered light with the illuminating light. It is possible to quantify this change and relate it to the position of the particle [81]. A second dichroic directs the beam from the condenser to the diode. The image of the BFP is formed on the 8mm face of the diode by a 50mm focal length planoconvex lens, see figure 3.3. These optics are all placed on an air table.

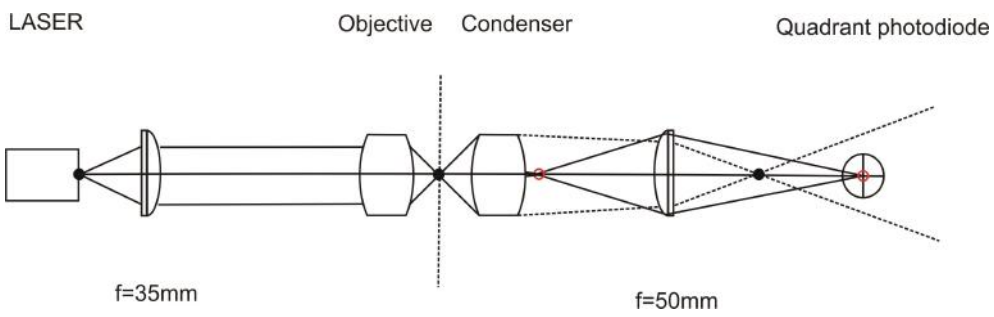

Figure 3.3: Ray diagram illustrating the path of the laser beam to the quadrant photodiode detector in the upright trap

The electrorotation slide is mounted on a piezo-electric stage, which provides nanometre displacements of the slide that are controlled by hand written LabView software. The objective lens is fitted to an x, y, z dovetail stage, which can be adjusted to focus the trapping beam and fixed in place with high mechanical stability. Both these stages and the condenser lens are bolted to a homemade aluminium box 140mm by 220mm.

3.1.2 Alignment

First the illumination was introduced to the microscope and the opitcal axis of the objective defined. With the objective and condenser removed the fibre was positioned to form an image on a piece of paper roughly in the position of the back focal plane of the condenser. The two lenses were then replaced. The electrodes were used to locate the optical axis of the objective and track the beam into the image forming lens and Watec camera. The field iris was shut down and imaged in the sample plane, centred on the electrodes.

The diode beam was then collimated, this was done by adjusting the position of the fibre terminus in relation to the collimating lens. The collimated beam was then reflected into the back aperture of the objective using the dichroic. Reflection of the beam appears as a Maltese cross on the monitor. Fine adjustment of the fibre and dichroic in x and y alters the axis of the beam to align it with the axis of the objective.

Once the trap had been formed, a maltese cross shape was visible in the camera image, reflected off the coverslip. A moveable high pass filter was placed between the objective and the camera, so that the laser could be blocked so it was not obvious on the monitor. It was possible to then trap and hold a 1μm latex bead suspended in water, a few μm from the coverslip.

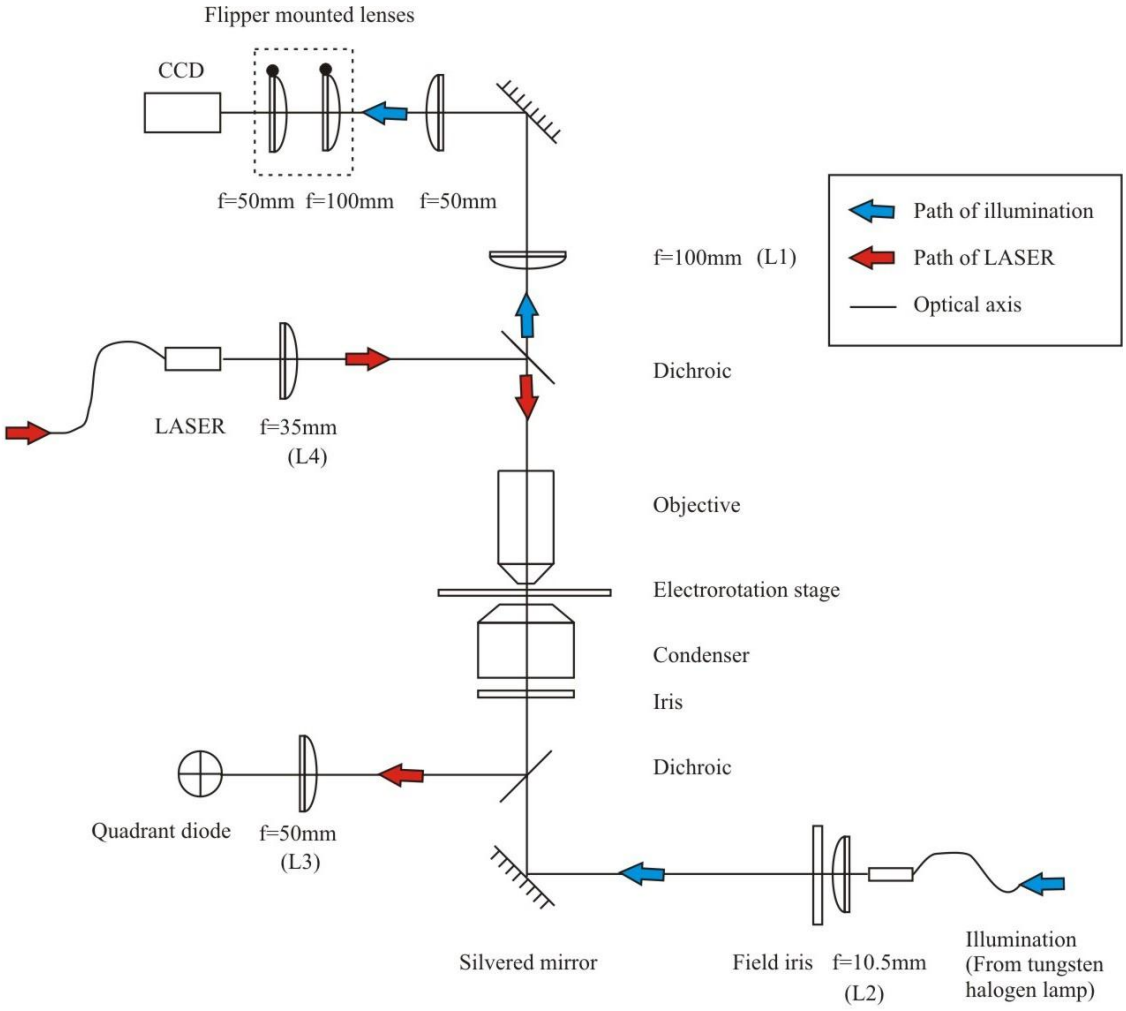

Figure 3.4: Optics of the trap. The trap is provided by a 980nm fibre coupled laser. The divergent beam is collimated by a 35mm lens, then brought to a diffraction limited focus at the specimen plane by a 1.4 N.A. objective lens. Transmitted light is re-collimated by the condenser and the back focal plane of the condenser imaged on the face of the four quadrant diode (8mm in diameter). The electrorotation stage is placed in the sample plane. Illumination of the sample is supplied by a tungsten halogen lamp. The beam is collected and fed into a multimode fibre. The source is then imaged on the back focal plane of the condenser. This ensures a collimated beam at the specimen plane that illuminates the entire sample. Scattered light from the specimen is brought to a focus on the charge coupled device (CCD) video camera, 8mm in diameter, creating an image of the specimen and the tips of the four microelectrodes.

3.2 Microelectrodes, flow cell and XY manipulator

In order to apply torque to the motor of a selected cell, either electrodes with very large gap encompassing many cells, can be used, or the cell can be moved to the centre of a set of small gap electrodes. The latter was chosen as small electrodes provide a much higher torque. The slide is searched for a suitable cell with attached, spinning bead. Once one has been located, it can be moved in relation to the electrodes to bring it over the centre. The electric field drops off dramatically with distance beyond the distance equal to the electrode gap. It is therefore preferable to have cells less than 25μm away from the electrodes when the electrode gap is 25μm.

Options for maximising the torque experienced by the rotating particle are:

- Raise the electrodes up to meet the particle
- Bring the particle down to the electrodes, i.e. narrow the channel to reduce the gap between the coverslip and the electrodes

The first option to raise the electrodes is to have pillar electrodes, figure 3.5 a). The electrodes project into the solution, allowing the use of a deep flow channel. Having a deep channel equivalent in depth to the standard design (100μm deep tape channel), means that the shear forces are reduced and the channel fills more easily. A second option to raise the electrodes is to create a mound, figure 3.5 b). This design is equivalent to pillar electrodes, but here the electrodes are fabricated by lithography techniques on to a pre-formed mound. The electrodes would be raised around 80μm.

The challenge of the final design, figure 3.5 c), is to make a channel that is less

than 25μm deep, with a movable wall. At this depth the flow is approximately laminar and the shear forces are high.

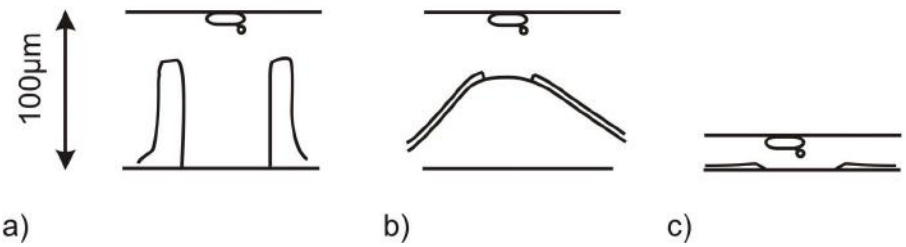

Figure 3.5: Possible designs for the electrodes: a) Pillar electrodes; electrodes that project into the solution. b) Mound electrodes; nanometre electrodes are fabricated by photolithograpy onto a 80μm raised mound, patterned onto the glass. c) Narrow channel; electrodes are again fabricated by photolithography but the channel depth is reduced, to bring the cell closer to the electrodes.

3.2.1 Minimising the distance between the cell and the electrodes

The first design to be tested was a set of raised gold pillar electrodes. The electrodes were in the centre of a 5mm square channel, bounded by a 100μm teflon wall and had been fabricated previously by H. Morgan and M. Sandison. These were difficult to clean as grease and debris was attracted to the electrodes, where it became stuck in between the individual projections. The teflon wall would not form a water tight seal. This design was abandoned as a tight seal could not be made without adding grease to the teflon, which then was attracted to the electrodes during application of the voltage. The electrodes were extremely difficult to clean and it was not possible to make a successful flow cell with a manipulable wall.

A micro-fabricated mound was suggested as a template for the electrodes. An 80μm mound in a 100μm channel would leave a gap of 20μm between the electrodes and the bacterium. This would reduce the pressure required to fill an equivalent

20μm flow cell and solutions could be flowed in by capillary action alone. The separate electrodes would not project into solution, so cleaning would be much easier, grease and debris would not get stuck between the metal. This option was also abandoned as the fabrication of the mound, by M. Sandison, proved time consuming. Simultaneously the design for a grease channel appeared to be working well. If the channel could be narrowed, it would eliminate the complex fabrication techniques required to create a raised mound.

3.2.2 Grease channel printing

The solution to making a narrow, sealed channel with the possibility of moving one wall, was found to be the use of grease. Rectangular grease walls of 4mm by 15mm, approximately 2mm wide by 15μm deep, were formed using the following protocol:

Grease channels for the electrorotation experiments, requiring a narrow channel, were made in the same way. The shape of the channel was cut out of a piece of parafilm and this was used as a mask. This mask was then placed on a second piece of film. Vacuum grease was was applied to the mask using a syringe and the excess scraped off with a slide. The parafilm mask was then removed, leaving the shape of the channel in 100μm grease. The film was used to print the grease onto the substrate, the electrode slide. A coverslip was placed on top of the grease and finger pressure applied. The depth of the channel was measured using a microscope and by marking the glass slide and coverslip. The channels were measured at between 10μm and 20μm, which is less than the smallest electrode gap used, of 25μm.

The action of the grease channel is depicted in figure 3.6. The entire slide can be searched to find a suitable cell with spinning bead, 3.6 a). Once this specimen has been selected, the coverslide is moved with respect to the electrode slide, whilst maintaining a water tight seal to keep the bacteria alive and facilitate flow if neces-

sary, see figure 3.6 b).

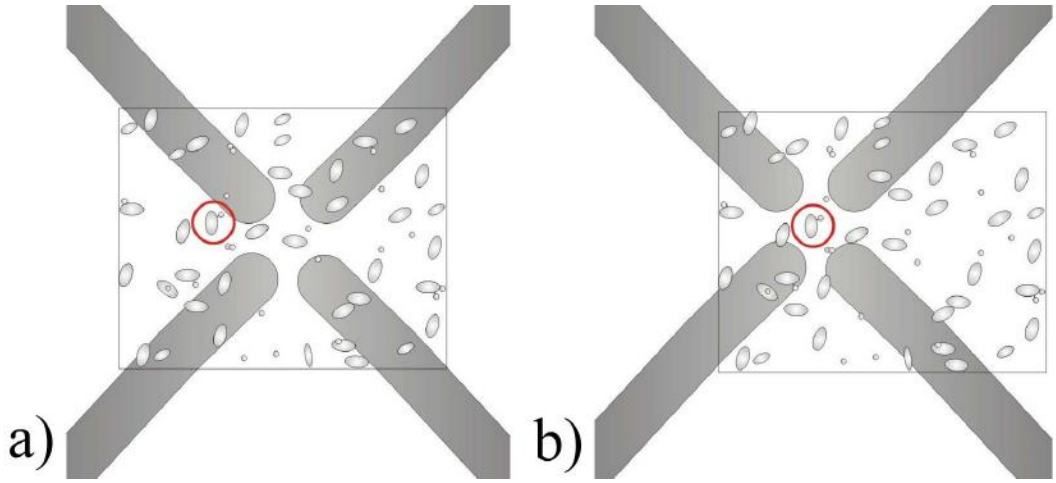

Figure 3.6: a) A suitable cell with attached rotating bead is selected. b) The cell and bead are moved to the centre of the electrodes by manipulation of the coverslide.

A further option for the design of the electrode flow cell was considered, that of electrode arrays. A two dimensional array could possibly allow the walls to be fixed, if there is a high enough probability that a suitable cell will be found in proximity to an electrode centre. Fabrication of a two dimensional array requires several layers of patterning with an insulating layer between each layer of metal. As each layer is added the aligning of the layers becomes increasingly difficult.

3.2.3 Fabrication of microelectrodes

Once it was established that a narrow enough channel could be fabricated with grease walls, and that this could be filled with no leakage, the first set of electrodes could be designed, see figure 3.7. The electrodes were designed so that as many devices as possible could be fitted onto a 10.2cm (4 inch) wafer. The flow cell was to have one inlet pipe placed at 9mm from the centres to allow it to fit next to the condenser lens. The channel was designed to have three walls with one side open to

allow exit flow. This removed the need for an exit pipe which would have to be a further 9mm from the centre on the opposite side. A brass slider which was used in previous experiments was designed to be taped to the coverslip, then glued to the x, y stage to allow manipulation of the coverslip. Five of the first set of electrodes were fabricated by photolithography, see the protocol at the end of this section, two with centres of gap 25μm and 40μm, and one with a centre of gap 60μm were made so that these could be compared experimentally [1].

Firstly a mask for the electrodes was designed using software and sent off to be printed as metal on quartz. Micro-electrodes were then fabricated by photolithographic techniques in the clean room facility.

A 10.2cm glass wafer was coated in consecutive layers of 20nm Titanium, 100nm Gold and 20nm Titanium. The Titanium acts as an adhesion layer and also protects the inner gold layer. Layers were formed by vapour deposition. Vapour deposition involves heating a metal filament to boiling point under vacuum. The glass substrate is then coated as the gaseous metal condenses on its surface.

The metal coated wafer was then spin coated with a layer of positive photoresist. A photoresist is a material that is chemically altered by ultraviolet light allowing a pattern to be printed. Positive photoresist is made up of a resin base, a photoactive compound and an organic solvent. When the photoactive compound is exposed to ultraviolet light, it is broken down. The dissolution rate of the exposed resist is increased by up to 1000 times. The wafer is held under vacuum to a spinning plate. A drop of resist is placed in the centre of the wafer and the resist spreads out to form a thin layer.

The pattern on the mask was then projected onto the wafer. A beam of nearly collimated monochromatic ultraviolet light is shone through the mask onto the wafer

[1] Single electrode slides, set 'A' were fabricated by myself with the help of M. Sandison at the laboratory of H. Morgan, Southampton University

for a fixed length of time. The exposed resist can then be dissolved in an alkaline developer solution, leaving the electrode pattern. The exposed metal was then etched away by placing in a strong acid etch solution, leaving the final electrodes. The remaining resist was removed by washing with acetone.

Figure 3.7 shows set of electrodes 'A', with a 25μm interelectrode gap and 33mm gap between bonding pads. An aluminium holder was made for the electrodes and this could be mounted directly on the trap, in a position where the electrodes were approximately centred in the objective. The holder was designed so that the glass slide was 1mm proud of the aluminium, the coverslip could then slide over the glass and not be obstructed by the metal. The wires were soldered onto the bonding pads then sealed with epoxy.

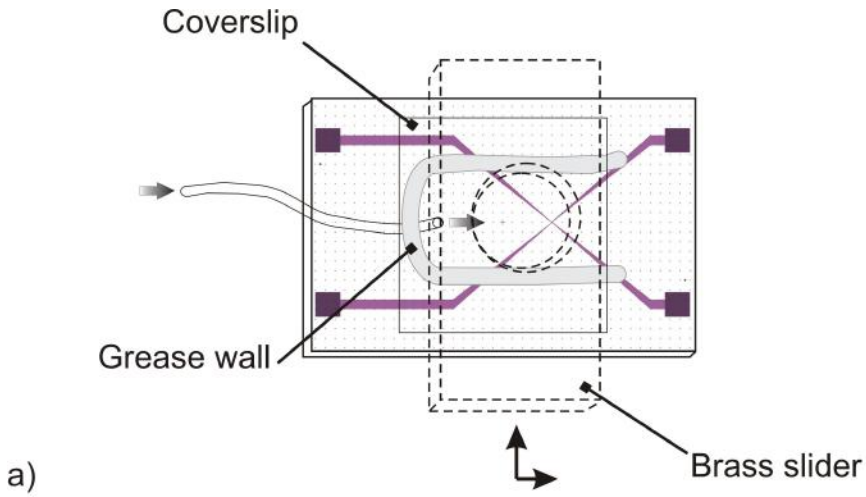

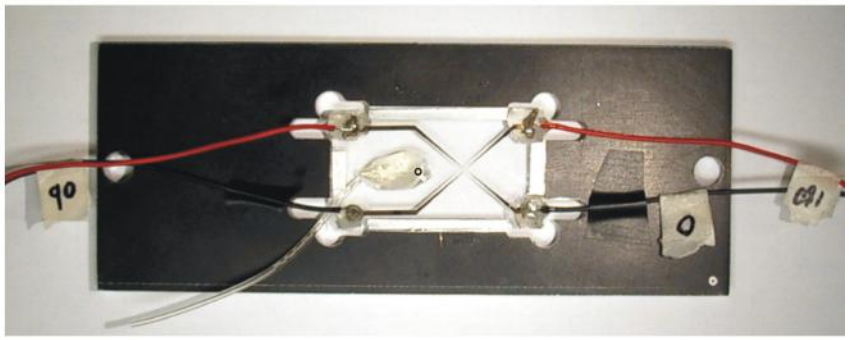

Figure 3.7: Set of electrodes A: a) Illustration of the electrodes plus flow channel, formed from printed grease and a square coverslip, with an attached brass slider. b) The electrodes and electrode holder

After calibration experiments it was necessary to make a second set of electrodes as the previous sets were easily scratched and broken in the soldering process and general handling. Set of electrodes 'B', figure 3.8, were glued into identical aluminium holders which fitted in a groove on the microscope stage, so they were positioned approximately in the centre of the objective focal plane. Wires of identical lengths were attached to the bonding pads using silver loaded epoxy, purchased from *RS Components*. Silver loaded epoxy was chosen instead of soldering, as the solder did not stick effectively to the bonding pads. The glass of two of the previous sets of electrodes was broken by the high temperatures generated by the solder iron in an attempt to solder the wires to the pads. Silver epoxy was applied and the wires held in place by masking tape. The epoxy was then cured at 90° for 15 minutes, which resulted in a strong bond. The flow tube was attached by drilling a hole with a diamond drill, inserting the tubing and epoxying the tubing in place. Once the epoxy was dry excess tubing could be sliced off with a razor blade leaving the electrode surface flat. The wires and tubing were glued down to the hand made aluminium holder to keep them in place.

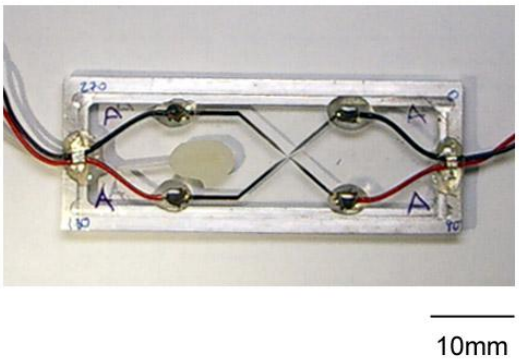

Figure 3.8: Set of electrodes *B*: Each set was placed in one of four identical aluminium holders, with the intention that each slide would come to rest in the same location over the objective. An electrode holder was made with a groove for the electrode holder to slot into, see figure 3.9

An aluminium plate was designed and made by myself in the research workshop for the holders to slot into, see figure 3.9. On the plate was also bolted an x, y micro-manipulator, with an aluminium arm. The grease channel was printed onto the electrode slide and sealed with a coverslip. The slide was then mounted on the aluminium plate. Double sided tape was applied to the brass slider and this was used to attach it to the coverslip. The aluminium arm of the x, y stage is moved up to the brass slider and epoxied in place. Once the epoxy had set, the coverslip could be manipulated in x and y via the brass slider. The arm was glued to the coverslip each time the experiment was performed.

The aluminium plate functioned to hold each electrode slide firmly while the coverslip was being manipulated and was useful as each electrode slide would come to rest in the same position when inserted into the groove. It also allowed the entire assembly to be carried independently of the microscope, so that loading of the cell and gluing of the coverslip could be done simultaneously.

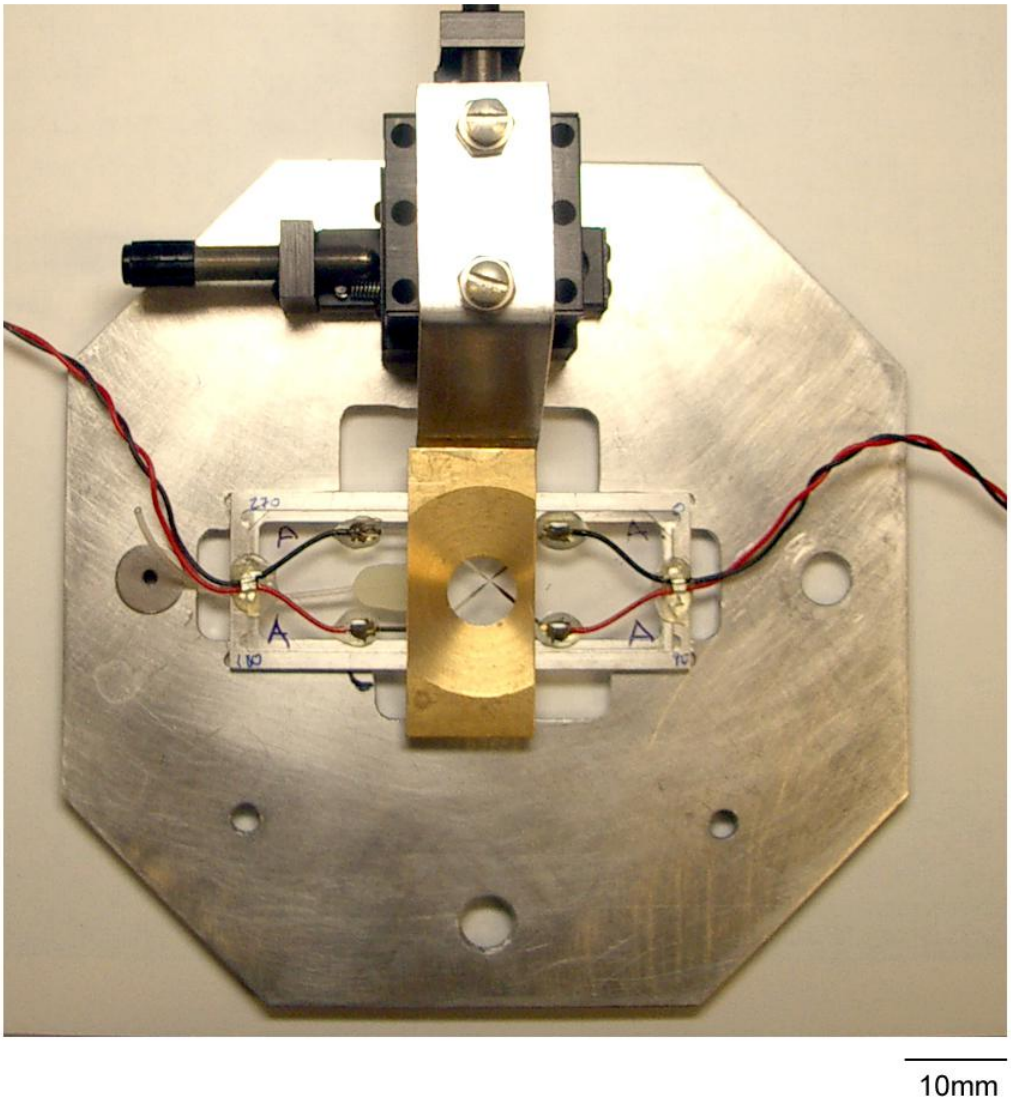

Figure 3.9: Electrode holder 1: The electrode holder for the upright trap.

3.2.4 Returning to the inverted trap

The design of the experiment had several problems at this stage. The buffer in the flow cell which exited through one side of the cell was wicking back under the brass slider. It was then mixing with the immersion oil for the microscope and disrupting the image. Larger coverslips were purchased in the hope that this would keep the two liquids from mixing. Once the large coverslip was applied I noticed that the protruding end could be attached directly to the x, y manipulator, removing the need for the brass slider, see figure 3.10.

Now that the grease channel design was working and the brass slider removed, it became obvious that this design could be easily inverted and transferred to the inverted microscope, without resulting leakage of the flow cell. Once cells decorated with beads were being rotated, it was also noticed that the beads were only sticking on long filaments. This meant that the orbit of the bead was too large for the detector. I realised that a stronger trap could be used to tauten the filament and hold the bead in place in the trap whilst the motor still rotated. This necessitated the use of the stronger inverted trap.

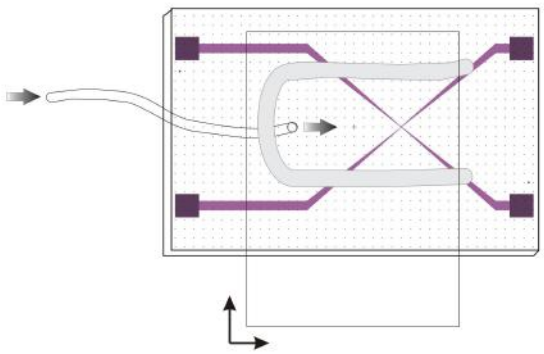

Figure 3.10: The second design for the flow cell to work with both the inverted and upright trap, set of electrodes B

3.2.5 Electrode arrays

A two dimensional array was considered to maximise the number of electrode centers that may have a suitable cell labeled with a bead in or near the correct position. This third design option could allow the flow cell to be fixed, not requiring a movable wall. The idea was abandoned after consultation with M. Sandison at Southampton University as it would require several layers of metal, separated by insulating layers. This increases the complexity of the fabrication and the margin for error in alignment of the masks for each separate layer of metal.

I therefore designed a linear array of nine four-electrode centres that could be fabricated in the same way as the single set of electrodes, see figures 3.11 and 3.12. There would probably not be enough electrode centres for the channel to be sealed and the need for moving the specimen would remain, however the yield of suitable specimen in proximity to a centre is increased by increasing the number of centres. Also damage of one set of centres would leave several remaining functional centres. The final slide was fabricated by a technician of H. Morgan and M. Sandison, in a facility in Switzerland, see figure 3.13. The bonding pads are now placed at the far ends of the side so that there is room for a larger flow channel, there is now space for an entry and exit flow pipe so that flow can be maintained during the experiment [2].

This new set of electrodes has a slightly narrower gap between the electrodes, of around 20μm. There are also nine centres on one slide, allowing a wider area to be scanned for suitable spinning beads. The bonding pads were moved to the edge of the slide allowing a larger area for the flow cell, as such it was possible to drill

[2]It was my aim to be able to fabricate the electrodes myself, so that I could replace sets as and when I needed them, and also alter the design if necessary as the experiment progressed. However, due to the destruction of the Southampton facility due to fire, the electrode arrays were fabricated by a technician in Switzerland. These had been damaged during fabrication but one of the nine sets was salvageable, using silver epoxy to patch the breaks in the circuit.

and inlet and outlet hole. 24mm × 40mm coverlips were used to make the flow cell which gave a few extra milimetres for the chamber. All together this slide made the exchange of fluid during an experiment possible. However the slightly different arrangement of electrodes changed the dynamics of the manipulated bead.

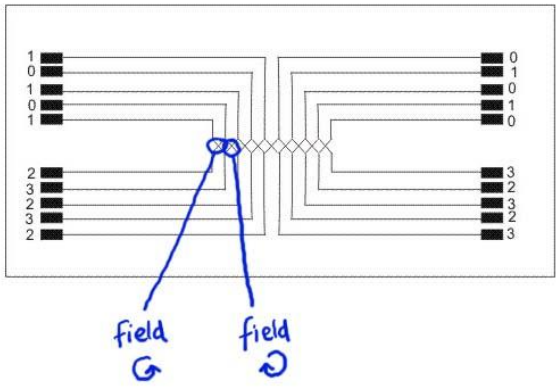

Figure 3.11: Electrodes set 'C'. The design for the electrode arrays.

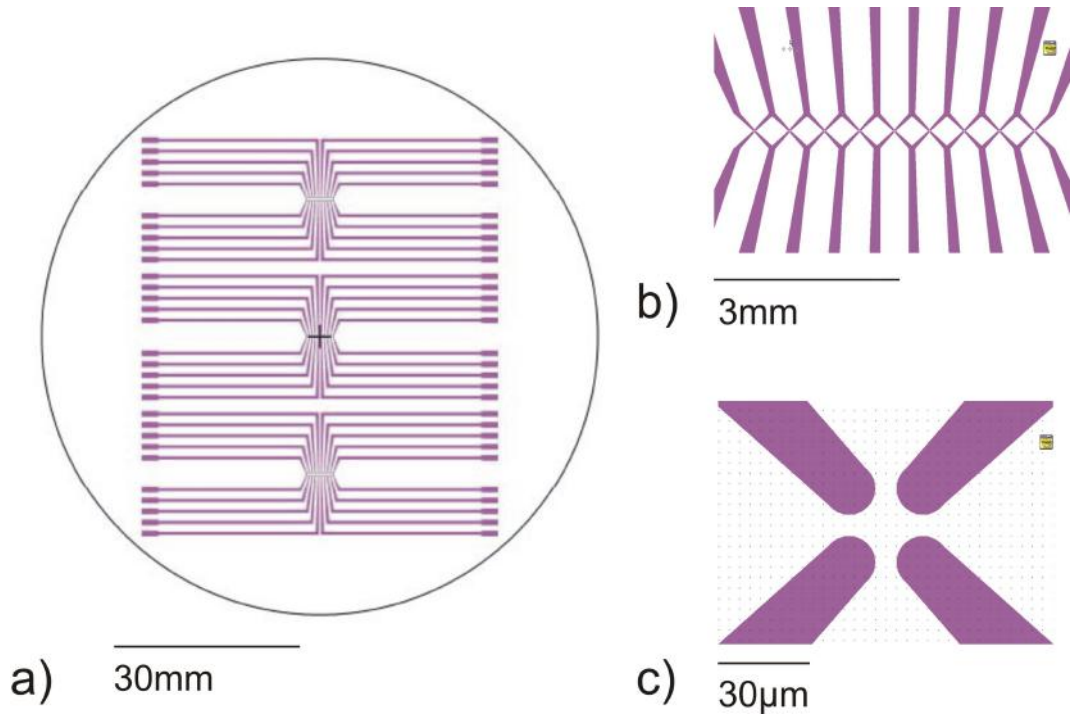

Figure 3.12: Electrodes set 'C'. The mask for the electrode arrays: a) The design for the wafer b) Magnification of the electrode centres c) Further magnification, the 25μm gap electrode centres. Designs were drawn in L-edit (Tanner Research, Inc.)

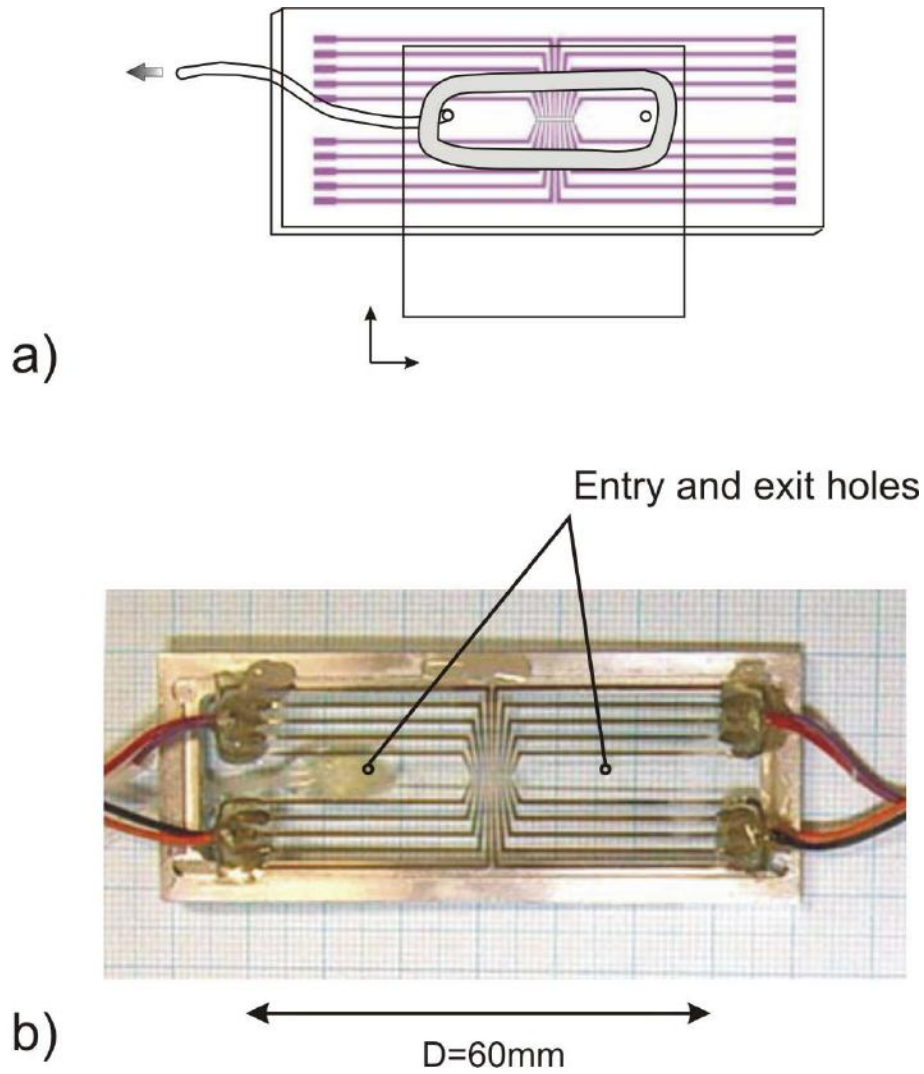

Figure 3.13: Electrodes set 'C': a) Diagram of the new flow cell. b) The electrode array slide and custom made holder.

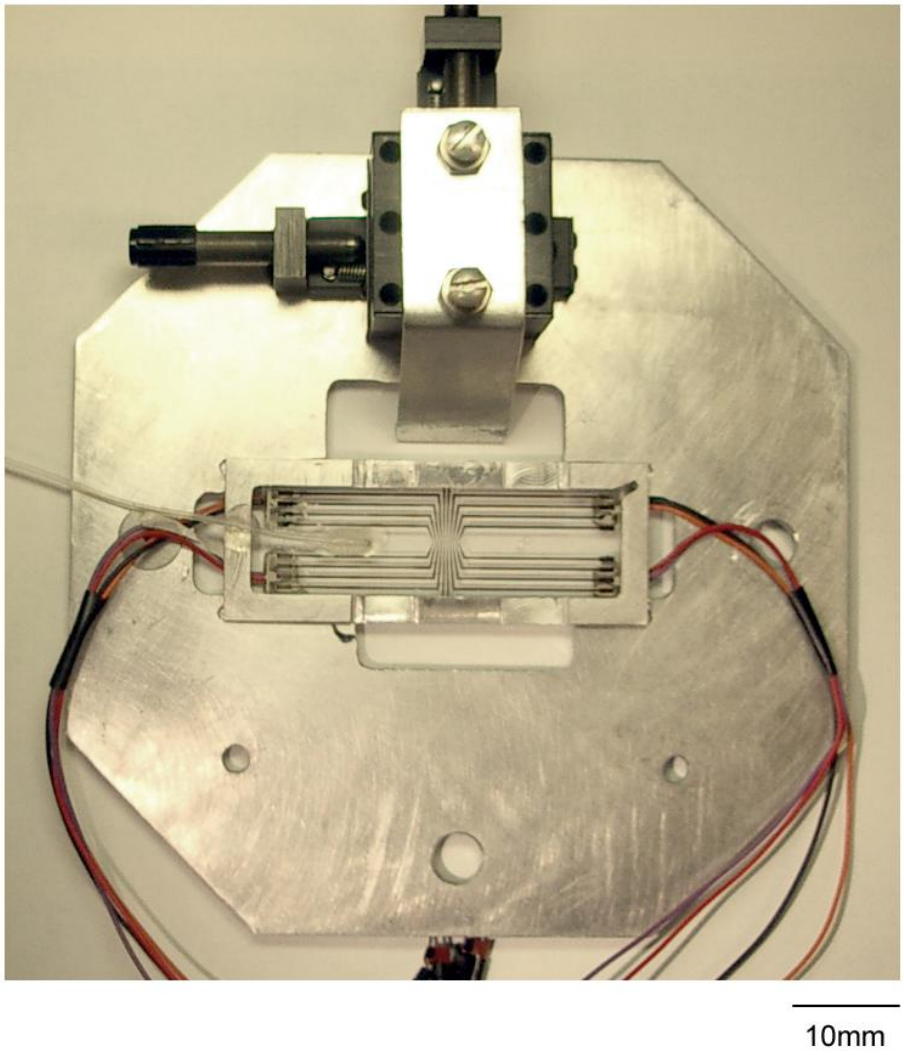

Figure 3.14: Electrode holder 2: The set up for the inverted microscope, with the electrode array slide. The improved design has a large coverslip of 24mm × 40mm which attaches directly to the xy stage removing the need for the brass slider. The electrode slide is viewed from above, the electrodes are on the reverse side, with the coverslip underneath.

3.2.6 Cleaning the electrodes

After an electrorotation experiment the electrodes would be covered with grease from the channel, beads and bacterial cells. Two methods of cleaning the electrodes after an experiment were tested; sonication and wiping.

Sonication:

Sonication in both 95% ethanol and detergent has been tried. Electrodes were placed on a piece of foam, in a beaker of de-ionised water and 1% Triton (detergent) or 95% Ethanol, filled to cover the device. The beaker was placed in a sonicator for a few minutes until the coverslip came free of the glass slide. The solution was then changed and the sonication repeated to remove the remains of the grease. Ethanol was abandoned as a method of cleaning as it dissolved the epoxy and rubber tubing attached to the electrodes. Triton was more gentle and effective at cleaning, however the sonication process appeared to be damaging the edges of the electrodes, so the wiping method was attempted.

Wiping:

Electrodes were wiped with *Whatman* lens cleaning tissue, first with decane then approximately three more times with ethanol. A fresh piece of tissue was used for each pass over the electrodes to avoid scratching with debris and moving the grease around. This was the more successful method and apparently less damaging to the electrode surface.

3.3 Conclusions

A laser detector has been constructed, with simplified optics so that it can be coupled to an upright microscope. This was successful and trapping of a 1μm bead observed.

A flow cell was designed that is approximately 20μm deep. A glass slide and coverslip formed the bottom and top surfaces of the flow channel. The walls were formed from printed vacuum grease, which allows the coverslip to be manipulated independently of the lower glass slide. This works well as it is possible to reduce the flow cell height beyond 25μm, with finger pressure on the coverslip, and there is no leakage.

Four sets of 120nm deep Ti/Au/Ti electrodes, two with 25μm and two with 40μm interelectrode gaps, were photolithographically fabricated onto glass wafers. The top 20nm layer of titanium increases the durability of the device so that it can be wiped clean with out scratching. A hole was drilled 9mm from the centre of each set of electrodes and a length of plastic tubing epoxied in place. This provides the channel with flow so that the bacterial cells, beads and buffer can be added.

Chapter 4

Characterising the Properties of the Micro-Electrodes

This chapter deals with characterisation of the micro-electrode flow cell, using polarisable, optically asymmetric, decorated beads. Rotating a bead at high speeds requires a strong trap to hold the bead in place, the inverted trap was therefore used. It is possible to trap a bead and move the piezo-electric stage in x, y and z and measure the rotation rate to investigate variation of the field between the electrodes, see illustration 4.1. The dependence on buffer conductivity and frequency can also be investigated in this manner.

4.1 Experimental methods

The oscillator used is a handmade 4 phase generator, made in the lab of Howard Berg and used in the experiments of Berg and Turner [98], which delivers 5 volts at 100% power output.

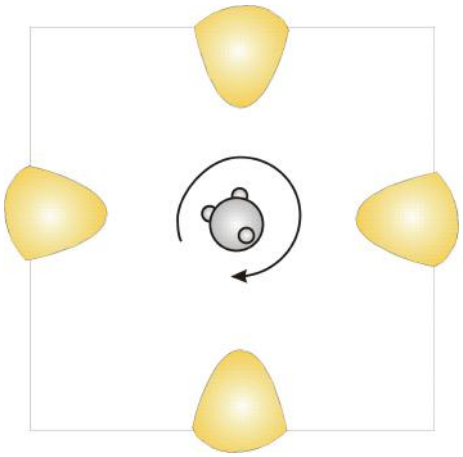

Figure 4.1: Illustration of a decorated bead held in the centre of the electrodes, rotated by the rotating electric field.

4.1.1 Media

Medium	Conductivity
De-ionised water	9μS
HEPES 1mM	44μS
HEPES 2mM	55μS
HEPES 5mM	112μS
HEPES 6mM	453μS
HEPES 10mM	669μS

All buffers are pH7. 1mM HEPES was used in all experiments unless otherwise stated [1].

[1] *Notes on HEPES buffer*: All measurements in this section were performed with alkaline HEPES buffer, this was reduced in pH to the band in which it functions most efficiently, pH6.8-pH8. However, addition of HCL $1M$ to reduce the pH increases the conductivity of the buffer. I then realised that it was possible to obtain acidic HEPES, in this case NaOH must be added to increase the pH until it falls within the desired region. The resulting solution is of lower conductivity than the alkaline HEPES, and therefore was used in subsequent experiments. The lower the conductivity of the buffer, the higher the torque generated when using highly charged particles

4.1.2 Polystyrene beads

Diameter	Surface modification	
0.833μm	carboxy modified	Polysciences
0.202μm	plain	Polysciences

4.1.3 Polarisable beads protocol

0.833μm polarisable carboxy-modified latex (CML) beads were decorated with 0.202μm plain latex beads, see figure 4.2. The polarisable beads were decorated for two reasons, firstly it would allow them to be detected rotating in the electric field due to their asymmetry, even when aligned in a stiff trap. Secondly, the large surface modified beads would not adhere to the bacterial filaments, due to the hydrophilic nature of the surface groups. The modified bead, however, can attach via the small beads, which are known to stick well.

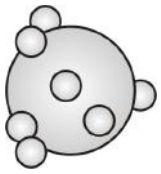

Figure 4.2: Illustration of a 0.83μm carboxy modified latex (CML) bead decorated with 0.20μm plain latex beads.

50μl	plain latex beads, 0.202μm
10μl	carboxy modified latex (CML) beads, 0.833μm
40μl	KCl, 3M, (final concentration 1.2M)

The volume ratio of 1μl of CML beads to 1μl of plain latex beads is equivalent to 1 : 44 by number. The ratio of 1 : 5 CML:plain is therefore approximately equivalent

to 1 : 9 by number.

The above solution was sonicated for 10 minutes, quenched in 1ml HEPES 1mM and then spun down in a 1ml eppendorf, using a microcentrifuge at 13000rpm for 2 minutes. This was repeated three times to remove the salt. The beads were finally re-suspended in 50μl HEPES 1mM (final concentration approximately 2μM KCL)

The high speed rotation of a decorated bead whilst held in the trap was demonstrated, see figure 4.3. The peak in the spectrum indicates 1150 revolutions per second.

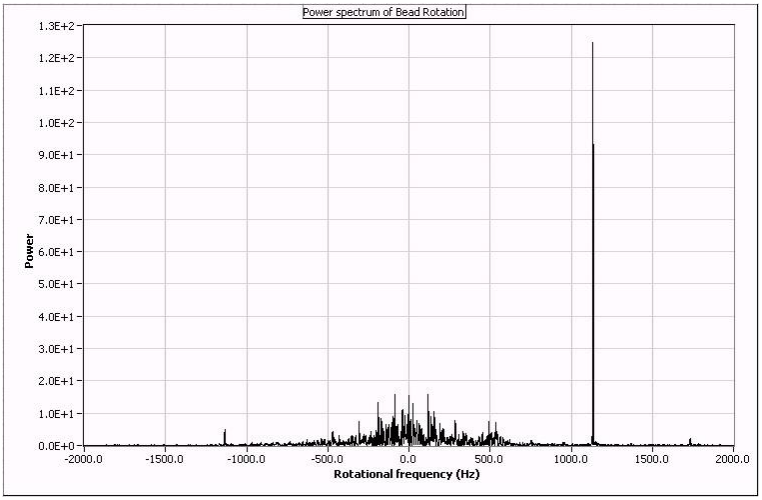

Figure 4.3: The power spectrum for the rotation of a decorated bead. The bead was suspended in 1mM HEPES and held in the centre of 25μm gap electrodes, with an applied RMS voltage of 5.2V and frequency 2MHz.

4.1.4 The flow cell for characterising electrode properties

Electrodes set 'A', with an interelectrode gap of 25μm were used to investigate the properties of the system. Electrodes set 'A' has identical centres to set 'B'. Set 'C' (the array) however, came out a little smaller, so further calibrations were made with these.

Wires were soldered to the four bonding pads on the glass electrode slide A. A hole was drilled on either side of the electrodes, 9mm from the centre using a Dremel drill, fitted with diamond drill bits, 1mm in diameter. 1mm bore tubing was epoxied to one hole to enable flow. A rectangular grease wall was printed on the slide, using the grease printing method, see chapter 3.2. The electrode slide was inverted in the holder. A length of tubing and the flow cell were both filled with buffer and the tubing attached to the outlet pipe. The slide was then mounted on the microscope stage. A drop of bead solution was placed on the entrance hole of the electrode slide and beads were flowed in under gravity by lowering the flow tube.

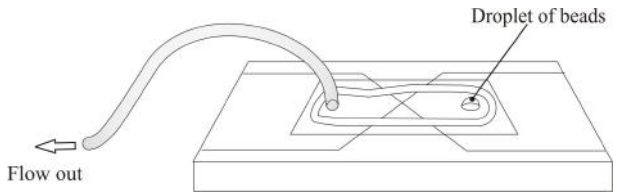

Figure 4.4: Illustration of the electrode slide

4.1.5 Method: variation with conductivity

The channel was loaded with de-ionised water. A 10μl drop of dilute decorated beads (1000× dilution from stock) in de-ionised water was placed on the exit hole in the slide and the beads were flowed backwards into the channel under gravity. A bead was trapped and rotated for a few seconds. Flow was then resumed for four seconds and a second bead selected and rotated, this was repeated for several beads. The droplet of de-ionised water was then removed and replaced by a 10μl droplet of beads suspended in 1mM HEPES, and the measurements repeated. This was subsequently repeated for 2mM, 5mM and 10mM HEPES solutions. Buffers were as detailed above.

4.1.6 Method: variation with z position

The 100× oil immersion lens was replaced with a water immersion lens. This allows strong trapping deep into the channel, necessary when approaching the electrode surface, as the oil immersion lens does not provide a strong enough trap to overcome dielectrophoretic forces. An approximately 20μm deep grease channel was printed onto an electrode slide, as described in section 4.1, to be placed on the inverted trap, see figure 4.4. The solution containing beads was flowed into the channel under gravity. A decorated bead was trapped, brought to the centre of the electrodes (as marked on the monitor screen) and a voltage applied to the electrodes. The bead was moved in z with steps of 1μm and its rotation rate measured. Beads were rotated in a 2.5MHz field, in 1mM HEPES.

4.1.7 Method: variation with x, y position

Beads were rotated in a 2.5MHz field, in 1mM HEPES using 25μm gap electrodes. The grease flow channel was $20 \pm 5\mu$m deep. The bead was trapped and rotated for one second, with a one second gap between measurements. Each point was 2μm and one second apart. The z height was kept constant at approximately 5μm from the electrodes.

4.2 Variation with frequency

A bead was rotated in the selected buffer, 1mM HEPES, at 25% power and the frequency altered through the range of the oscillator, 0.35MHz to 5.39MHz. The optimum frequency to achieve the maximum rotation rate was found to lie between 2.3MHz and 3.4MHz. The frequency chosen for the experiments was 2.5MHz. A low voltage was used to obtain the optimum frequency, to avoid collection of debris at the electrodes.

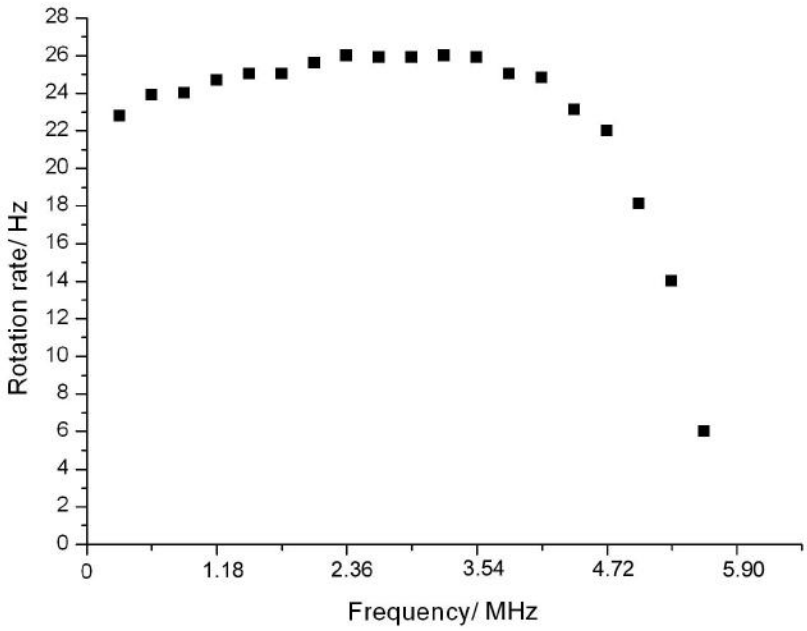

Figure 4.5: The frequency response of a bead

4.3 Variation with conductivity of the medium

Beads were rotated at 2.5MHz, in 25μm gap electrodes, approximately 5μm from the electrode surface in HEPES buffer of varying conductivity, see section 4.1. Figure 4.6 displays the average rotation rates for each buffer with the error as a standard deviation. Of the 60 beads trapped, 28 were rotated. Fewer rotation rates were obtained for the higher conductivity buffers as a smaller proportion of beads spun. The buffer selected for the *E.coli* experiments was 1mM HEPES as this produces the maxiumum torque. However the 2mM HEPES would also be suitable, producing rotation rates $(88 \pm 9)\%$ of those generated in the 1mM HEPES[2].

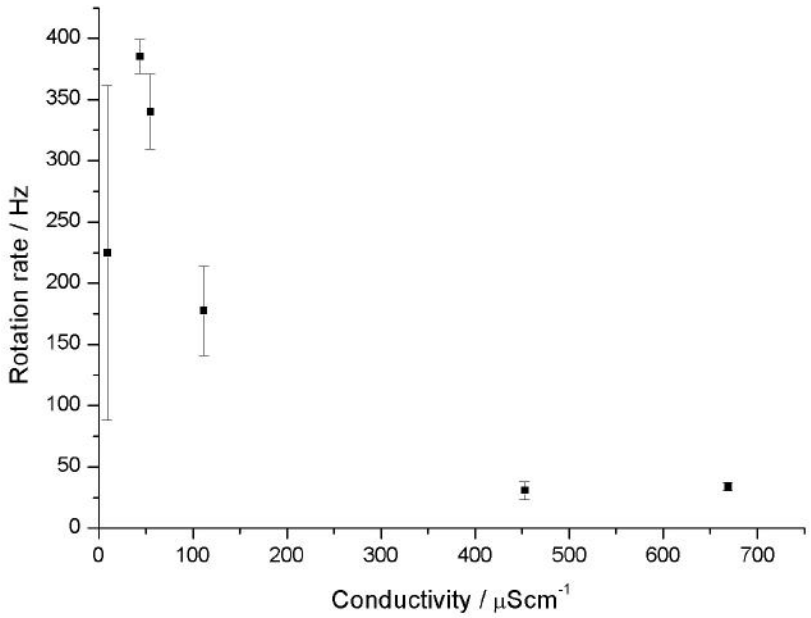

Figure 4.6: Rotation rate against conductivity of the medium for 25μm gap electrodes. Decorated beads were suspended in each of the following media: 1mM HEPES, 2mM HEPES, 5mM HEPES, 6mM HEPES and 10mM HEPES. Properties of the buffers are listed in section 4.1

[2]There are too many unknown parameters to fit the theory of Appendix A to the data, as the dielectric properties of the particle can only be estimated. If a few more data points were obtained this would be possible, however obtaining these points was highly time consuming

4.4 Variation with z position in the flow chamber

Six beads were rotated in three different conductivity media, see figure 4.7. The beads were moved in z towards the electrodes until they met with the surface. The maximum range of the piezo electric stage in z is 20μm. The results for each bead were normalised to the first bead, by determining the point at which the bead came into contact with the electrode slide. The six sets of data were then averaged. Error bars show the standard deviation on the mean of the normalised values. The consistency of the rotation rate over this range could possibly be attributed to confinement of the field lines by the channel. Further experimentation with differing channel size and exploration of the region close to the coverslip may therefore be of interest. The rotation rate at the centre of the electrodes was found to vary by less than 3% from 0 to 6μm from the electrode surface.

The variation with z position was re-calibrated for the electrode arrays, electrode set 'C', see figure 4.8. Here the electrode gap is a little smaller, approximately 5μm, the drop in rotation rate at the coverslip is now around one third of the value at the electrodes[3].

[3]It was hoped to repeat the z-position measurments with hind-sight to cover the area up to the coverslip for different depths of flow cell, however the piezo-electric stage became broken at this point

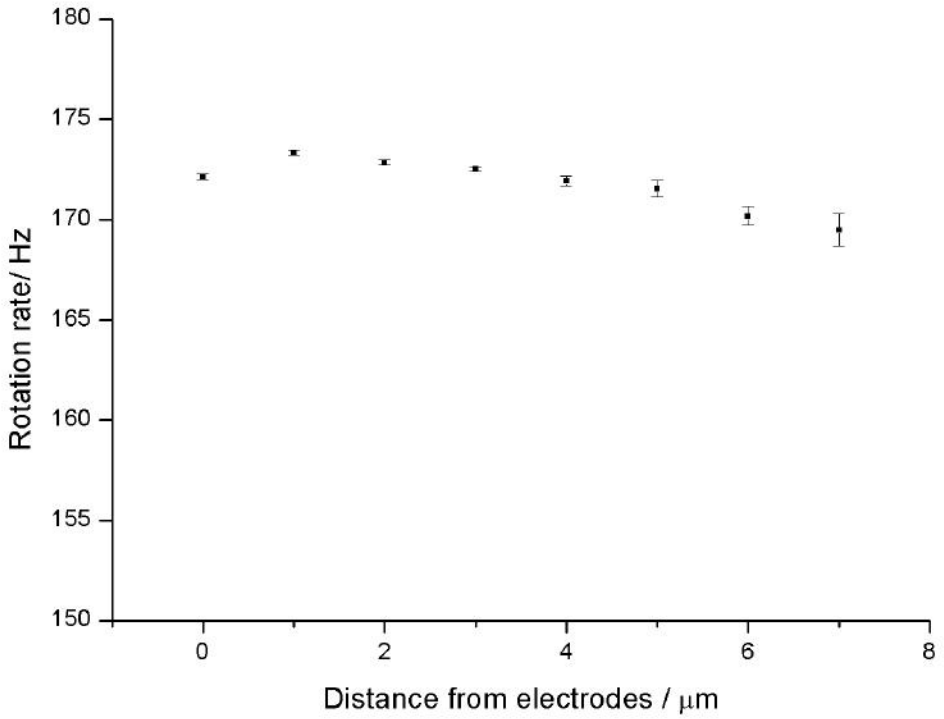

Figure 4.7: Graph showing the variation of rotation rate with z position in the electrode flow cell

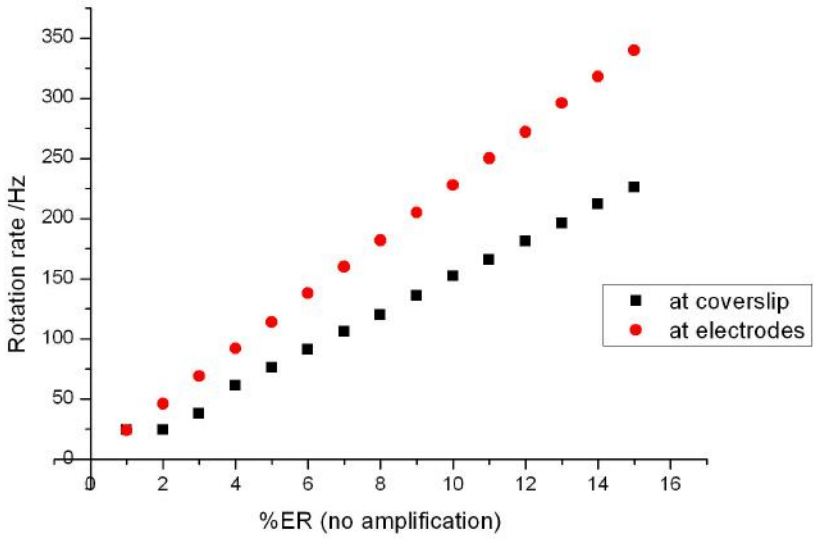

Figure 4.8: A bead was rotated in an approximately 20μm channel. It was rotated first just below the coverslip - the location of a bead when attached to a bacterial filament, and just above the slide, close to the electrodes. The rotation rate dropped by about a third as the bead was moved to the coverslip. This is a much more significant drop than in the previous electrodes, as the electrode gap is smaller. However, it is not much of a worry as the rotation rate next to the coverslip is much higher than previously recorded.

4.5 Variation with x and y position: A map of the field

The variation of rotation rate with x, y position in the electrodes, proportional to the torque on the bead, was measured as detailed in the methods section 4.1.

The average rotation rate of four decorated beads[4] was measured at 100 points in the centre of the electrodes. The data are plotted and superimposed on an image of the electrodes in figure 4.9. The torque experienced by the bead follows a double saddle shape with maxima close to the electrode tips and minima between each pair of adjacent electrodes. It can be seen that an area of $12\mu m^2$ in the centre of the electrodes varies less than 5%. It is therefore possible to place the particle to be rotated anywhere in this central region and it will experience the same torque to within this value.

Asymmetry in rate of rotation in figure 4.9 could be attributed either to irregularities in the electrodes or to charge migration, as a result of leaving the electrorotation voltage on for the duration of the experiment[5]. It is hoped that use of flow during the bacterial experiments will remove these effects.

The data of figure 4.9 can be compared with the model of Hughes *et al.* [86]. Hughes *et al.* modeled the electric field in a set of electrodes of $0.2\mu m$ thickness and $400\mu m$ inter-electrode gap. The charge density method of Wang et al. [85] was applied to simulate the torque generated by a rotating electric field, produced by

[4]The errors are not marked on the graph, the variation between beads was less than 5%

[5]The experiment was subsequently carried out with flow in order to address this problem, however the bead would not remain in the trap for the duration of the experiment. The strength of the trap was increased but this repeatedly resulted in a second bead being drawn into the trap before the end of the experiment.

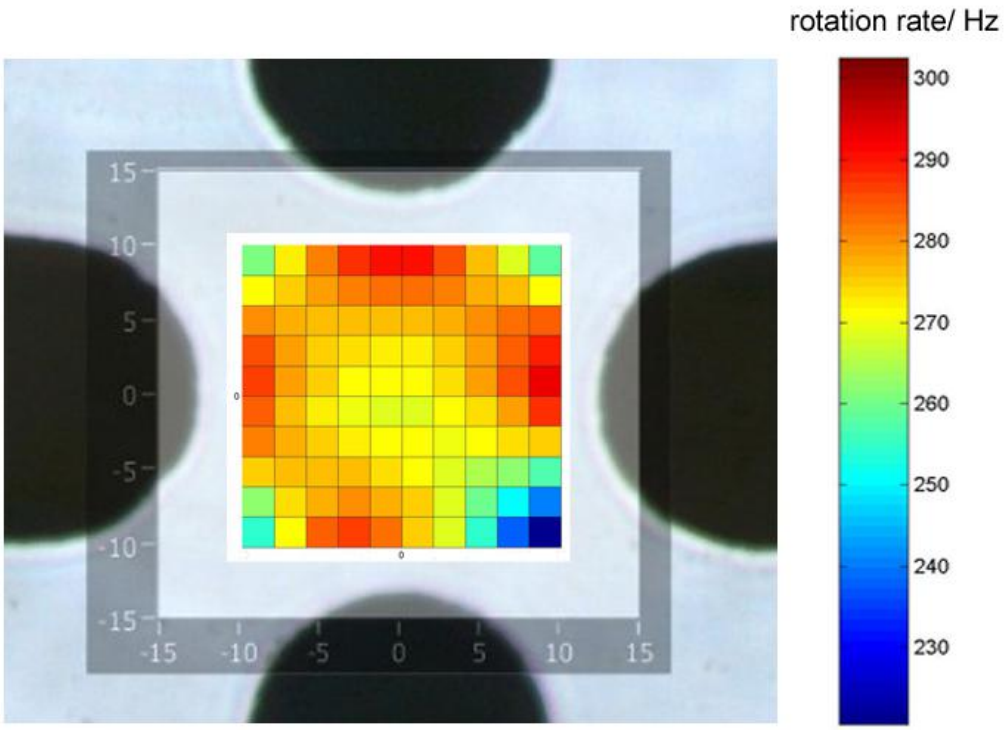

Figure 4.9: Image of the electrodes with a projection of rotation rates of a trapped bead. Each intersection on the grid corresponds to one data point. The scale on the electrodes is in micrometres and rotation rates are in Hertz.

the polynomial electrode geometry. The rotating field is simulated for one cycle of voltage, by calculating the static electric field for a grid of points in x and y, at 10° voltage intervals. The torque was derived from theory of Appendix A.

Hughes *et al.* showed that the magnitudes of the field vectors varied according to position, see figure 4.10 a). The general variation of the torque predicted by the model is close to that of the data, re-plotted for comparison in figure 4.11. The model also predicts that the magnitude varies over one cycle of the field. Only the field vectors located in the central region, a circular area with diameter about one quarter of the inter-electrode gap, behave as a circularly rotating field. There are regions where the induced rotation is contrary to the main rotating field. The simulation was made at 3μm above the upper surface of the electrodes.

Hughes *et al.*[87] went on to map the electrorotation torque experimentally, his technique is described for comparison with the current method. 3μm $\times$ 5μm elliptical beads were observed rotating in 400μm x 400μm gap polynomial electrodes [84]. Rotation of the beads was recorded by video and the time to complete five revolutions timed by stopwatch. This was done for 203 beads at random locations within the defined area, see figure 4.10 b) for the raw data. Due to dielectrophoretic effects, the motion of the particles could not be measured in a 50μm band surrounding the electrodes as they were forced out of this region. They estimated an experimental error of 5% on the speed measurements and also a variation between beads. The trend in the data was not apparent in the raw measurements due to the noise. However, after reflecting the data along its axes, rotating the data four fold due to the symmetry of the electrodes, and applying a 40μm moving average, the results appeared similar to the simulation. It was concluded that the torque varies in excess of 50% in this central gap.

The trapped bead technique for mapping the field is useful, as one bead can be used for all data points and it can be moved to any desired position in all three dimensions. It would be interesting in the future if the method could be used to measure the angular component of the torque, to find the axis of rotation. Attempts were made at this but these were unsuccessful.

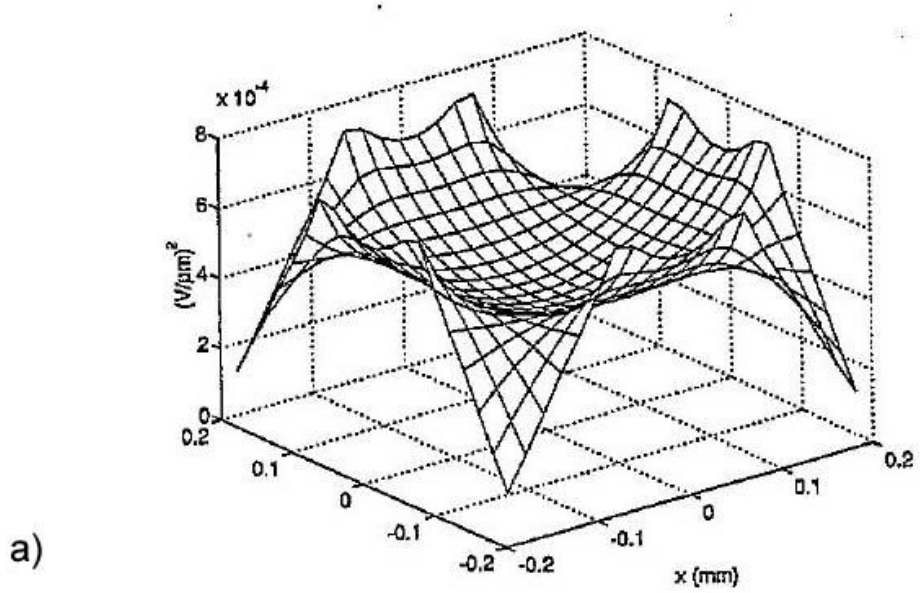

a)

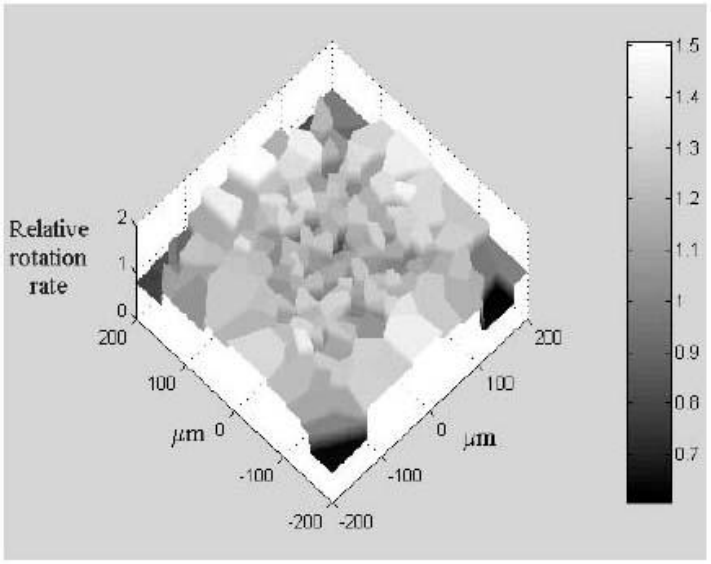

b)

Figure 4.10: a) Predicted spatial variation of the relative torque for electrodes of spherical geometry. Figure from [86]. b) Data from the rotation of five micron elliptical beads, rotating in 400μm gap electrodes. Figure from [87]

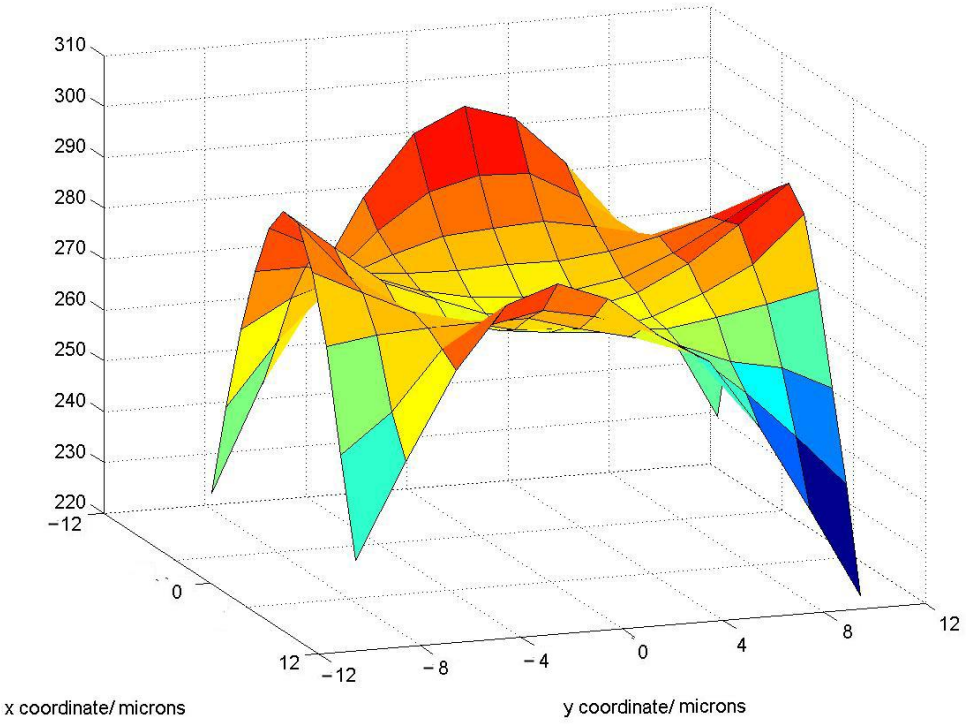

Figure 4.11: A 3D plot of the rotation rate measured at each point in figure 4.9, averaged over four beads. The centre of the electrodes lies as in figure 4.9, at (0,0).

4.6 Variation with time

Three beads were rotated, each for 300 seconds, at a different power, see figure 4.12[6]. Beads were rotated at 10, 25 and 50% power, corresponding to voltages of 2.6V, 4V and 5.2V, where power is proportional to the torque applied to the bead and varies as the square of the voltage. There is no apparent drop in rotation rate at the two lowest voltages. At 50% power the drop in voltage is around 3% over 300 seconds of constant rotation. This drop in rotation rate with time can be attributed to charge migration due to the applied voltage, which results in a local change in the buffer composition. The non-symmetric rotation rate in the field map can therefore be explained by this effect.

[6]Measurements were made with electrodes set 'C', the electrode array with sub-25μm gap.

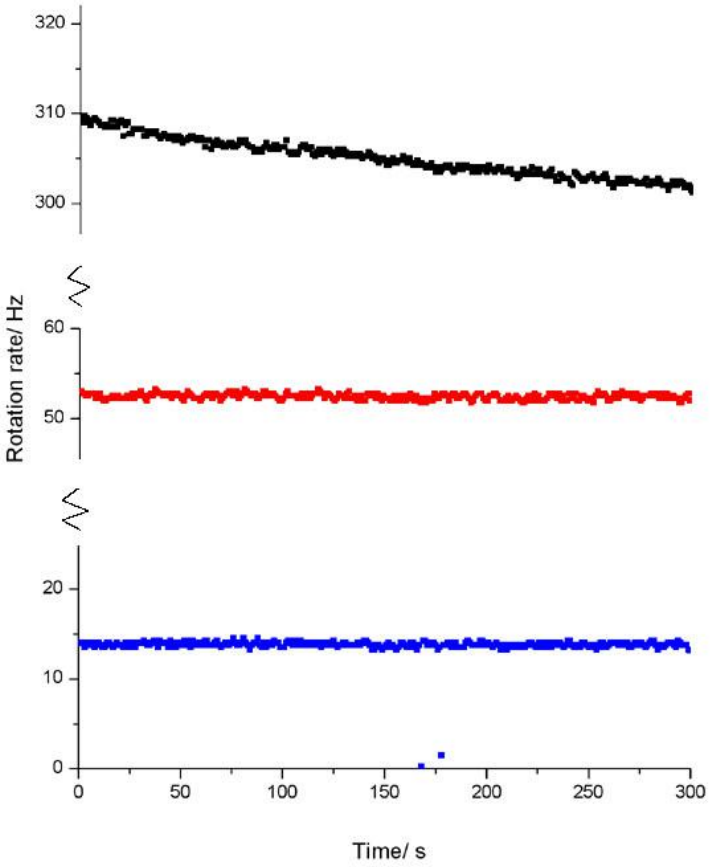

Figure 4.12: The rotation of three beads held in the trap, each rotated at a different power.

4.7 Conclusions

A protocol for making decorated polarisable beads, which can be electrorotated, was devised. A 0.833μm decorated bead was rotated at speeds beyond 1KHz and this motion detected by the back focal plane method.

Decorated beads were found to rotate beyond 1KHz at maximum voltage, with out amplification, using an optimum frequency of applied current of 2.5MHz. The variation of rotation rate as you move away from the electrodes was found to be less than 3% within 6μm of the electrodes. This allowed the variation of the rotation rate in x and y to be plotted whilst keeping z roughly constant. A plateau region of 12μm^2, where the electric field varied by less than 5% was evident. It was therefore possible to define a large region in the centre of the electrodes, 40% of the total area, where the rotation rate was known to vary by less than 8%. The particle to be rotated did not have to be placed accurately in the centre of the electrodes for the same torque to be experienced.

The 1mM and 2mM solutions of HEPES produced approximately twice the torque of the 5mM HEPES. Using 25μm gap electrodes and as low conductivity buffer as possible, 1mM, 44μS HEPES, beads were rotated at over 350Hz using $\frac{1}{4}$ of the available voltage from the oscillator. This is significantly greater than the zero torque speed of the fully induced bacterial flagellar motor, measured at 250Hz by Berg and Turner [98]. 1mM HEPES was selected as a suitable buffer, in which the bacterial cells could survive, that provides a high torque for rotation of the beads and reduces local heating in the solution as it has low conductivity.

Chapter 5

Electrorotation of *E.coli*

The aim of this chapter is to repeat the experiments of Berg and Turner [98] to test the new electrode flow chamber and method of detection. Berg and Turner electrorotated tethered cells in order to measure the torque generated by the motor over a range of speeds. The experiments suffered from the following issues, which have been improved upon in the current set up.

Local heating

Due to the use of high conductivity buffer, local heating required the use of a sapphire window. A highly conductive buffer was chosen by Berg and Turner to maximise the torque on the bacterial cell. For a given electrorotation power, cells rotated at 28Hz in the low conductivity buffer (0.004mScm^{-1}), and at 48Hz, in the opposite direction, in the high conductivity buffer (0.41mScm^{-1}). The optimum frequency of rotation for a cell was found to be 0.75MHz and 2.25MHz in the respective buffers. A sapphire window was used to allow heat transfer and reduce local heating. Cells were covalently linked to the sapphire surface so they would remain attached during rotation. In my experiments a low conductivity buffer was selected to eliminate

local heating. The extra torque afforded by a highly conductive medium was not necessary, as sufficient torque was generated by the electrodes. This was due to a much smaller inter-electrode gap of 25μm, compared with Berg and Turner's 70μm gap electrodes. It was possible to use such small electrodes with a small inter electrode gap, due to the shallow flow channel that was designed, which had a depth less than this gap value.

Motion detection

Large cells were necessary for motion detection with the linear gradient filter. Large cells have a correspondingly large drag coefficient, which decreases the speed of rotation and applies large unnatural stresses to a tethered motor. The use of the optical trap and back focal plane detection method allows much smaller cells to be rotated, which reduces the viscous drag.

Elipticity of the field

The approximately 70μm diameter electrodes were hand made and therefore not perfectly symmetrical, generating an elliptical field. This irregularity may be the cause of artifacts in the torque speed curve, such as a false barrier to backwards rotation. It was hoped that the use of photolithographically fabricated gold electrodes would reduce the ellipticity of the field.

5.1 Experimental methods

Electrode set 'B' were used for the experiments in this chapter. The wires were bonded to the bonding pads using silver epoxy (RS), which was then cured at 90°C for 10 minutes. Silver epoxy was used to remove the need for solder, as the heat from

the soldering iron broke several of the previous sets of electrodes and the contacts were not durable. The silver epoxy worked well.

The bacterial cells at approximately 3μm in length were much larger than the focused laser beam spot, and as such the detection of their motion was very noisy. This was improved by placing an iris in the laser beam path before the objective lens, to reduce the diameter of the beam. With the iris shut down (so that the beam was approximately 1mm wide) the focused laser spot size was increased resulting in an improved signal from the detector.

5.1.1 Media

Tryptone broth	Bacto-tryptone	1%
	NaCl	0.5%
Motility medium	$KHPO_4$, pH7	10mM
	NaCl	85mM
HEPES medium	HEPES pH7	1mM

5.1.2 Growing cells

KAF95, Δ*cheY*, *fliC* sticky filament [98]

100μl	cells (from frozen)
5μl	ampicillin [100μg/ml]
5ml	Tryptone broth

Incubate for five hours at 30°C with shaking

WSR8, *motA* point mutation, *fliC* sticky filament [70]

100μl	cells from freezer
5μl	ampicillin [100μg/ml]
3.7μl	chloramphenicol [34μg/ml]
5ml	Tryptone broth

Incubate for six hours at 30°C with shaking

5.1.3 Tethered cell assay

Cells were grown as above. 1ml of cells was spun down in a micro-centrifuge at 7000r.p.m. for 2 minutes and washed with motility medium. This was repeated three times. On the final spin, cells were re-suspended in 50μl motility medium. A grease channel was prepared as described previously. The dry flow cell and tubing was loaded with motility medium using a syringe. Cells were then flowed through under gravity, using the filled flow tube. The cells were left to flow gently into the chamber for 10 to 20 minutes, sticking and flow was observed under the microscope. Once an even carpet had formed, remaining cells were washed using 50μl of motility medium.

5.2 The torque speed curve with tethered cells

Once the new experimental setup was complete and the flow cell working, the experiments of Berg and Turner [98] were replicated. The strain used was *cheY* deletion, non-switching, sticky filament *Escherichia coli* strain KAF95, constructed by Karen Fahrner [98]. 1mM HEPES was chosen as the low conductivity buffer to eliminate local heating and the need for a sapphire window to dissipate heat, and to maximise the torque generated. Photolithographically fabricated electrodes were hoped to reduced the problem of ellipticity in the field and allow the motor to be driven both forwards and backwards with out angular considerations, however this appeared not to be the case.

In total 11 cells were rotated. The motors of the majority of these cells broke on application of an external torque. Two cells were rotated that appeared not to break. Noise in the data is due both the short intervals over which the cell was rotated and the design of the detector. The cells were rotated for short intervals of 0.1 seconds to decrease the likelihood of the cell breaking. The detector was optimised to detect the rotation of micron sized particles, the rotating cell body gave a poor signal due to its large size.

The x and y signals were analysed using custom LabView software. Figure 5.1 shows the data for cell 11. The cell was rotated from 0 to 60% power five times, it was then rotated at 100% power, breaking the motor. The initial measurements were then repeated. The data for the runs with the working motor and broken motor were each averaged, see figure 5.2. The difference between the two was then plotted as a speed offset, equivalent to the torque generated by the motor, see figure 5.3.

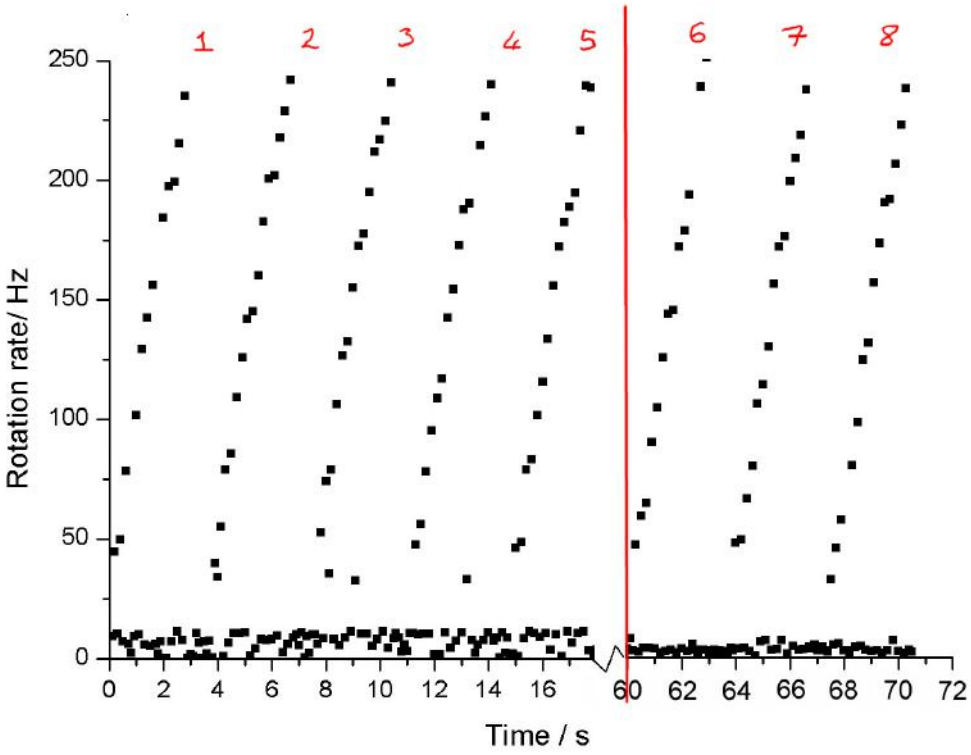

Figure 5.1: Rotation rates for an electrorotated tethered cell

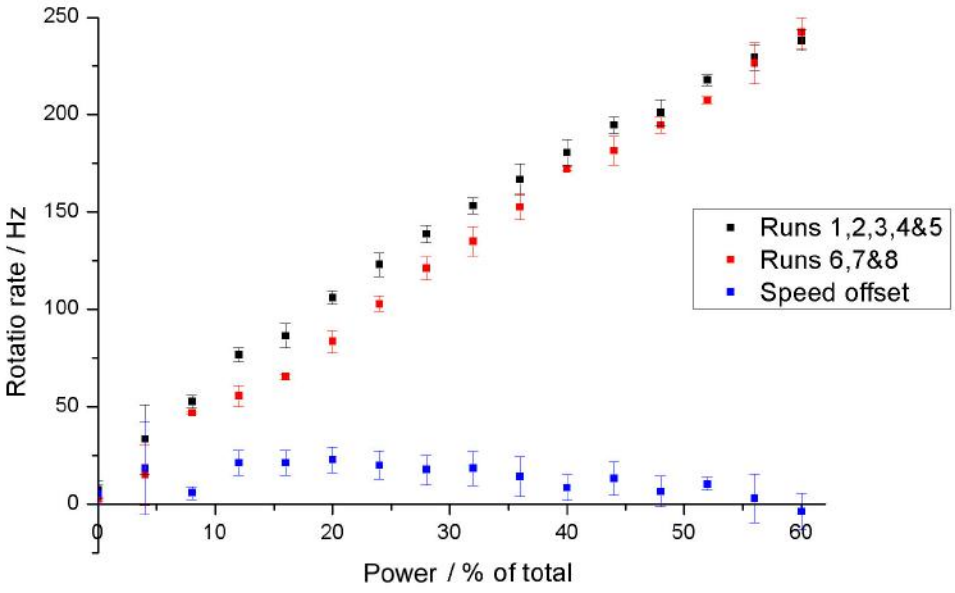

Figure 5.2: Averaged rotation rate against applied voltage, for the cell in figure 5.1

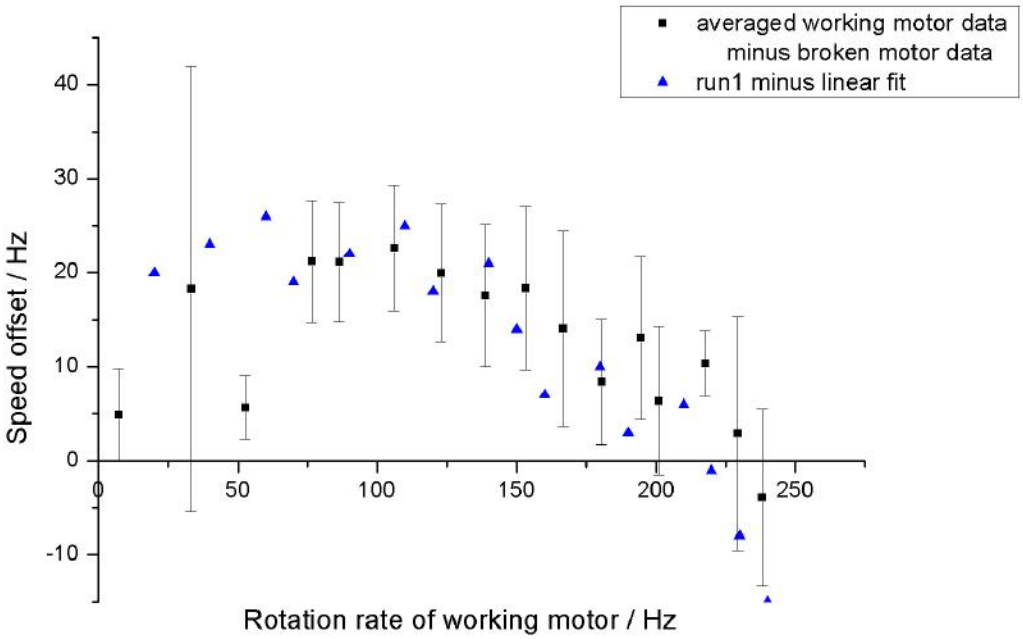

Figure 5.3: Speed offsets for the cell in figure 5.1. Errors on the averaged data, black squares, were calculated from the standard deviation from the mean.

A speed offset was plotted for this cell using a different analysis technique. The first run was selected and a straight line was fitted to the rotation rate against voltage, for rates below 100Hz. In this region the torque generated is presumed to be constant. The total rotation rate is assumed to be due to the rotation rate generated by the electric field plus the rotation rate generated by the motor, [70]. It is therefore possible to estimate the rotation rate generated by the electric field by shifting the linear fit to intercept the origin, see figure 5.4. This was then subtracted from the original data and a speed offset plotted, see figure 5.3. The points indicated by blue triangles correspond to the data calculated by this method. The speed offset is proportional to the torque generated by the motor, given by the equations 1.3 and 1.4. This speed offset can be compared to the previous speed offset for the cell, indicated by the black squares in figure 5.3.

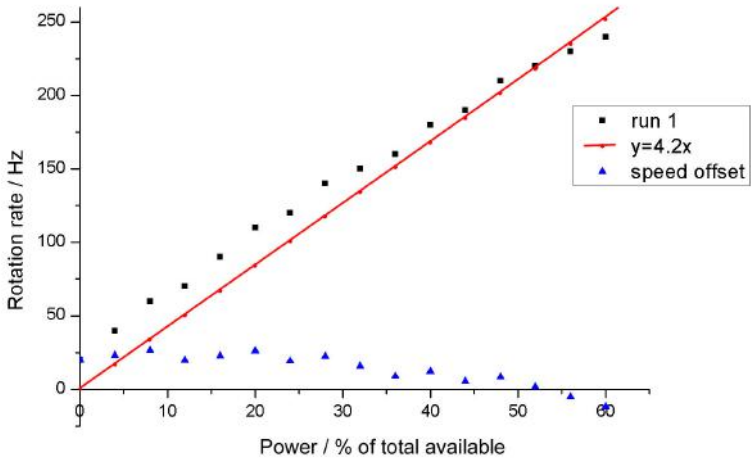

Figure 5.4: A linear fit to the rotation rate against power for the cell in figure 5.1

In many cases it was not possible to break the motor with out detaching the cell from the glass surface. The better method was then used to plot torque speed curves for motors which had not been broken. A linear fit to the first four points in the rotation rate against voltage plot was shifted to the origin and subtracted

from the data to produce a speed offset, see figure 5.5. The zero torque speed is approximately 350Hz from this figure. This is within the range of zero torque speeds estimated by Berg and Turner stated as between 200 and 400Hz [98]. Data beyond approximately 500Hz can be attributed to noise as the tether may have been disrupted at these high rotation rates.

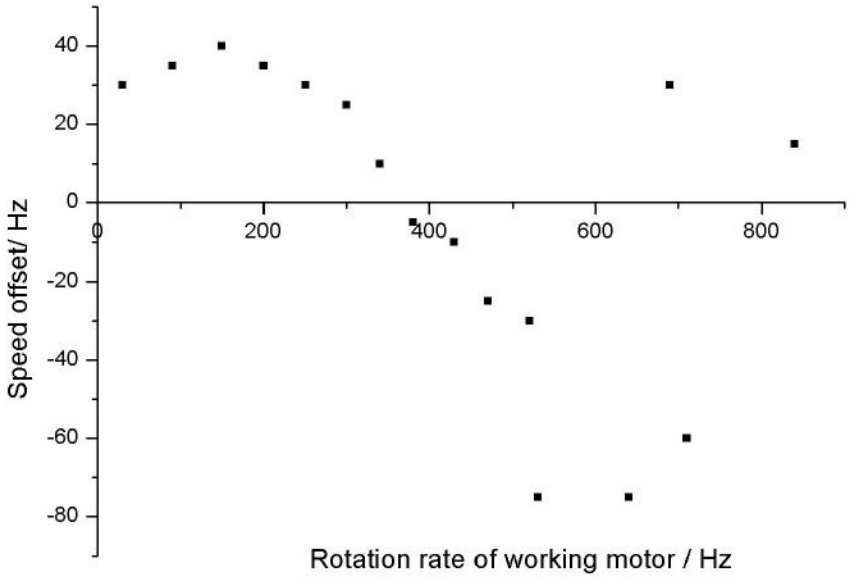

Figure 5.5: The speed offset for another cell, rotated beyond 300Hz. Data beyond 500Hz is most likely noise.

A very high voltage was required to force the cell backwards, the majority of cells become un-stuck or broken at this extreme. It is noticeable that the cell sticks when it is forced backwards and gradually the angle changes as the voltage is increased. This effect was also noticed by Berry and Berg [106] and is probably attributable to ellipticity in the field [107]. Ellipticity in the field arises from either the signal generated by the four phase generator, (this does appear to be elliptical) or the electrodes themselves, if they are scratched or damaged this may affect the field. In addition the path of the current to the electrodes may vary between electrodes, the connections and cables are not perfect. It possible that speed of rotation varies with angle depending on position in the field as suggested by Hughes [86].

Figure 5.6 shows a typical example of the variation in the speed of the rotating cell with angle, during the application of external torque. Angular variation was calculated by fitting an ellipse to the x and y data from the quadrant photodiode for each block of data. In this case 0.1 seconds long, corresponding to 200 points. The ellipse fit was then used to estimate the variation with angle of the rotation rate. The rotation rate ranges from less than 10Hz to over 200Hz over one revolution, which is a dramatic variation with angle. It is possible that it is this irregular torque on the cell which causes the barrier to backwards rotation. By rotating a symmetrical bead attached to a filament it is hoped to reduce or eliminate altogether the angular variation and therefore obtain torque speed data in both directions of rotation. As the noise is of the order of the rotation rate of the cell it should be expected that any trend would not be resolved.

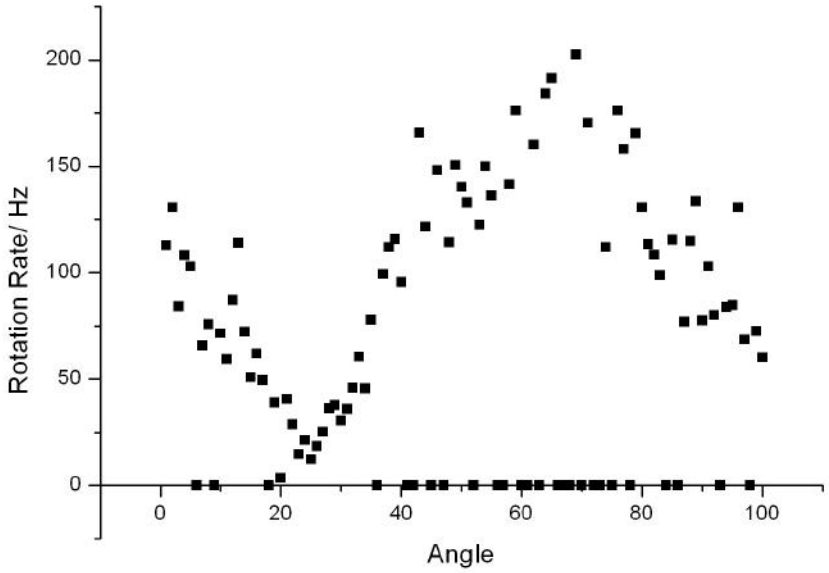

Figure 5.6: A typical plot of the rotation rate with angle for a cell rotated by external electrorotation. A similar plot for a cell rotating under its own power showed no variation with angle.

5.3 Experiments on tethered cells with one single torque generating unit

In order to say that a motor is working under one single torque generating unit, you need one of two situations. Either you know the load on the motor and the viscous drag, in order to be able to predict the speed at which such a motor would rotate, or you keep both these constant so that the variables can be ignored. In the case of a rotating bead, this is possible as each bead is of a similar size. Therefore, the number of units in a particular motor can be deciphered by relating this speed to speed of the total population. However, this is not possible in the case of the rotating cell, as each cell differs in length and position of the centre of rotation. The cells are also much larger and are irregular in shape compared to a bead. Therefore the external torque required to reach high speeds is much larger.

The rotation rates of 48 tethered KAF95 cells were measured to find if there was a correlation between this and cell length. The cells were chosen to have tether positions as near as possible to the end of the cell so that the effect of this on the results would be minimal, see figure 5.7. The rotation rate is found to be approximately proportional to the inverse of the cell length as expected.

Cultures of WSR8 were grown to investigate the possiblity of experimenting on different stator number cells. WSR8 is a *motA* point mutation strain that will resurrect when induced with isopropyl β-D-thiogalactopyranoside (IPTG). When grown under low-level induction conditions, in 5μM IPTG, the average number of stator units present in each motor is approximately one. As the concentration of IPTG is increased in the growth stage, the average number of wild type stator units increases. I was interested to see if the number of stator units could be resolved from the cell

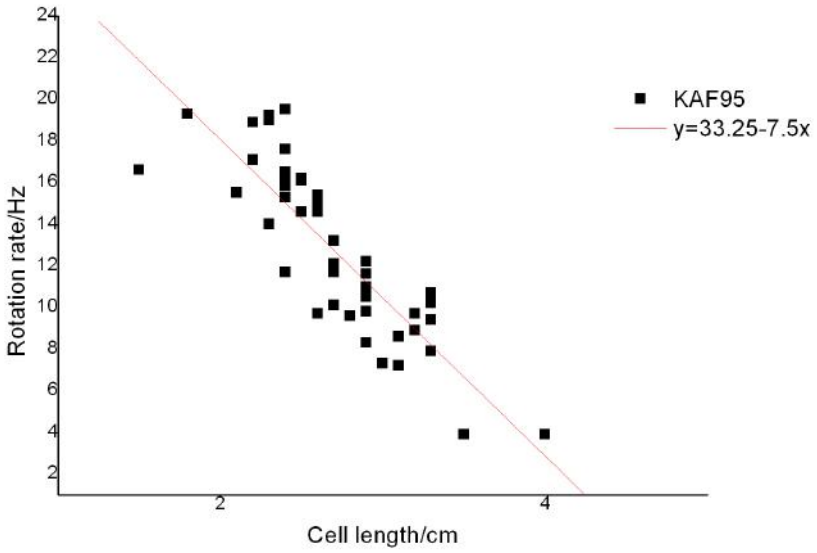

Figure 5.7: Rotation rates for 48 tethered KAF95 cells plotted against the length of the cell body.

rotation speed for a tethered cell. Reid *et al.* was able to plot speed distributions for different concentrations of inducer and obtain an average rotation rate per stator unit using a bead assay[61]. Each stator was found to correspond to an increase in speed of approximately 7Hz. The single stator unit speed would be expected to be lower for a rotating cell. The rotation rates of 78 cells in 5μM IPTG and 87 cells in 10μM IPTG were multiplied by the cell length divided by the average cell length (2.6μm). A histogram of these rates is given in figure 5.8. It is possible that a cell of 2.6μm had a rotation rate of 24Hz fully induced, speeds above that may be due to the cell being tethered at the mid point and the detector recording double the actual speed. It is not possible to discern a single stator unit speed from the histogram, where this would be estimated at 1-2Hz.

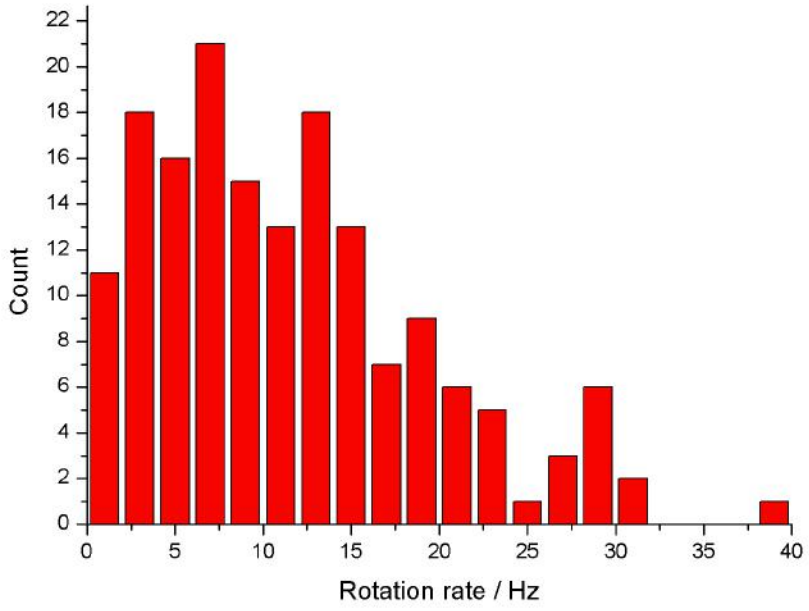

Figure 5.8: Histogram of rotation rates of 77 cells of WSR8 grown in 5μM IPTG, and 86 cells grown in 10μM IPTG after accounting for length.

5.4 Conclusions

A torque speed curve for KAF95 was plotted that is in agreement with the previous results of Berg and Turner, and Chen and Berg [98, 109]. The signal from the rotating cells was noisy and it was not clear how much damage the electrorotation had done to the cell. It would be useful to have more information on the cells free rotation rate in between applications of electrorotation. The next step in the experiment was to see if a torque speed curve could be plotted for single stator unit motors. Cells were grown under low induction conditions and speed histograms plotted using the method of Reid *et al.* [61]. However in this case the speed of rotating cells was measured instead of beads on cells. This introduced greater noise to the system and the variables of cell length and tether position. The cell length was taken into account when plotting the rotation rate histogram, however this revealed no distinction between stator numbers.

Subtracting the rotation rate of the broken motor from that of the working motor is the method used by Berg and Turner to plot a speed offset curve, this seems reasonable if all variables are kept constant between the rotation of the working motor and the rotation of the broken motor. However, if the properties of the medium have changed locally due to electorotation this may introduce errors. Since Chen and Berg, and Ryu *et al.* [109, 70] confirmed the constant torque plateau up to approximately 100Hz, it is also possible to obtain the torque due to electrorotation by assuming a linear fit to the data in this region and shifting to the origin. This improved method was used to calculate the torque when broken motor data was not available. Changes in the properties of the medium become significant when the field is applied for a length of time. Charge migration may also depend on flow of the medium through the channel and or percentage of cells and beads in the vicinity of the electrodes.

The technique of rotating tethered cells is not ideal, as the drag on the motor is far greater than it would experience in nature. Also the detection system is not optimised to detect the rotation of such large particles. The error in the above experiments is high, due to the size of the cell and the length of the interval. If the interval is increased, fewer cells survive electrorotation. Despite this, the experiments determined that the method and apparatus worked well and previously published results were confirmed and improved.

Chapter 6

Electrorotation of Decorated Beads Attached to the Filament Stub of *E.coli*

The aim of attaching polarisable 1μm beads to the flagellar filament is to increase the resolution of the experiment. The external torque required to rotate the bead is also much less than that of a tethered cell, and much closer to the rotation rate of a naturally spinning motor. The data obtained from the tethered cells in between applications of electrorotation pointed to progressive breaking of the motor during forced rotation, however the resolution was not high enough to reliably say the extent of the breaking or to estimate a stator number. It is hoped that rotating a bead will allow more information to be gained during the experiment.

The first few attempts to bring together the sheared cells assay, narrow grease channel and the decorated beads were made on the upright trap. It was observed that any spinning decorated beads were stuck on long filaments. The standard ra-

dius of orbit for a 1μm plain latex bead attached to a sheared filament is between 150nm and 250nm. In this case the radius of orbit was frequently 1μm or more. A possible explanation for this is that the charged beads are repelled by the negative cell body. It was decided to trap the beads and pull the tether tight, so that the bead rotates on its axis. This required the more powerful trap with a 1W laser, which was set up on an inverted microscope.

6.1 Experimental methods

Electrode set'B' were used for the beginning of this section. Upon breaking these electrodes, the arrays, set 'C', were then used. The electrode arrays were prepared by bonding four wires to the bonding pads using silver epoxy (RS), which was then cured at 90° for 10 minutes, as previously described.

The original protocol for making decorated beads, from section 4.1, was used. The decorated beads stuck well to filaments when suspended in 85mM NaCl motility buffer and added to un-sheared cells, see image figure 6.1. The yield was dramatically reduced by shearing the filaments. When the beads were stuck to filament stubs and electrorotation applied, the signal was weak, possibly due to a low level of decoration. In order to increase the yield and get as strong a signal as possible, another method of decoration was sought. The divalent salt magnesium chloride was used at high concentrations, up to 8M. 0.833μm CML beads were observed after spending 10 minutes in a sonicator in varying concentrations of $MgCl_2$. Above 2M the CML beads were seen to stick to each other forming pairs, above 4M there was excessive clumping of the beads. 2M was chosen as the charge double layer could be overcome at this concentration and it was hoped that beads sticking in this level of salt would remain tightly bound over long periods of time and high electrorotation

forces.

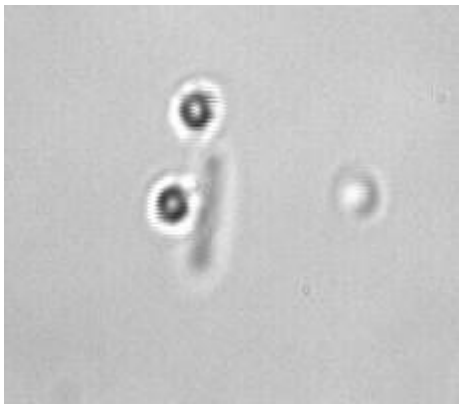

Figure 6.1: Image of a bacterial cell with attached decorated beads.

6.1.1 Decorated beads for beads on cells experiment

70μl	plain beads, 0.202μm
20μl	carboxy modified latex (CML) beads, 0.83μm
910μl	$MgCl_2$, 2M

The above was sonicated for 15 minutes and quenched in 9ml of 1mM HEPES buffer. This was then spun down three times to remove the salt and re-suspended in 1mM HEPES. The dilution used was 2μl 0.83 CML for every 100μl of solution, the solution was made more dilute than previously to allow the use of higher salt but still reduce clumping of beads.

Beads were spun down in a sucrose gradient to remove as many of the 0.202μm beads as possible. A sucrose gradient functions to separate particles of varying drag into well defined 'bands', which can then be separated to give mono-disperse samples. Beads were spun in a Beckman centrifuge (rotor 'JS13.3', which accommodates 1ml tubes, were used) at 11000rpm for 15 minutes. The beads were then washed

three times into 1mM HEPES to remove the sucrose and resuspended in 20μl 1mM HEPES. See below for details of the sucrose gradient formation. The beads were stored in the fridge for a maximum of 5 days and then a new batch were made, as the level of decoration of the beads drops over time.

Preparation of sucrose gradient:

Two tubes were joined at the bottom by a connecting pipe, and one was fitted with an exit pipe. A magnetic stirrer was placed in the bottom of each tube to aid mixing. 5ml 10% sucrose solution was placed in the tube with the exit pipe and 5ml of 5% sucrose solution was placed in the other. A 10ml Beckman centrifuge tube was coated with 10μg of bovine serum albumin in 1ml water, and clamped at an angle below the mixing tubes. As solution drained from the 10% tube, the 5% and 10% solutions mixed through the connecting pipe. The solution from the exit pipe was collected in the Beckman tube for centrifugation in a standard Beckman centrifuge. This separates the small beads from the large and decorated beads. Small beads left in the bead solution stick preferentially to the filaments reducing the yield of spinning decorated beads.

6.1.2 Preparing the decorated bead electrorotation assay

The standard bead on cell assay:

Cells were grown as in section 5.1. A glass cover slide was cleaned in KOH and ethanol, rinsed and air dryed. A tape tunnel slide was prepared with the clean coverslip.1ml of cells were sheared and spun down at 7000r.p.m. for 2 minutes. These were then washed into motility medium. This washing was repeated three times to remove the filaments. The final preparation was resuspended in approximately half the original volume. Polylysine (1%) was added to the dry flow channel followed

by cells. The slide was then left for 15 minutes, with coverslip underneath in a humidity chamber. After 15 minutes the slide was washed with approximately 100μl of motility medium. Beads (0.1% solid, 50$\times$ dilution in motility medium) were added to the flow channel, and left for 15 minutes. These were then removed by washing again with 100μl motility medium.

The decorated bead assay with electrode flow cell:

Cells were sheared as before, and approximately 1ml of cells re-suspended in 100μl motility medium. A grease channel was formed with a cleaned 24×40 coverslip. The dry channel was then flushed with a few μl of 0.1% polylysine. This was then removed immediately by flushing with 50μl motility medium, using a syringe and negative pressure. The flow tubes were then filled so that cells could be flowed in under gravity. Cells were added to the entry tube and flowed gently - the flow was observed under a microscope to ensure there were no obstructions. The cells were allowed to flow through the slide for 15 minutes. The slide was then flushed with $50 - 100\mu$l motility medium. A few mul of decorated beads at concentration 2μl 1% solid in 10μl 150mM NaCl motility medium were then added. The flow of beads into the chamber was also observed to make sure it was steady and that there were no large clumps. A gradual flow was maintained for 15 minutes. The beads were finally flushed out with 100μl HEPES 1mM.

6.2 Rotating beads on cells

The experiments of Berg and Turner [98] on rotating tethered cells, see section 1.7.4, were repeated with a new technique, designed to improve upon the technique and extend its possible applications. Here a polarisable bead is attached to the filament via smaller plain latex beads.

6.2.1 A torque speed curve for varying numbers of stator units

Over 100 beads on cells of wild type KAF95 were rotated over the course of several experiments, with an average of three cells per slide[1]. Three cells were successfully rotated beyond the zero torque speed and the most resilient cell is shown here as an example. A second cell, which also survived repeated rotation (although not beyond the zero torque speed) and showed slightly different behaviour, is analysed for comparison.

The orientation of the bead on the tether seemed to be important, as some beads would stop spinning when trapped and most motors would break on application of the electric field. Alignment of the bead in the trap can cause the motor to stall depending on how the bead is attached to the filament and its orientation with respect to the hook, and the symmetry of the decoration of the bead itself [128]. This means that few cells were aligned properly for electrorotation and could explain why many broke.

[1]The yield of spinning beads is often low, depending on the way the flow cell is filled (as it is so narrow) and the consistency of the various solutions. However, this was improved upon as the experiment was repeated.

Different durations of electrorotation were used in the experiments. Increasing the interval for which the bead is rotated, increases the rotation rate resolution of the experiment. However, it also increases the effect of the voltage on the surrounding medium, possibly drawing charge into the region, or leeching this from the nearby cells and the conductivity of the medium possibly increases. The result is to lower the electrorotation strength more dramatically than in the previous experiments. In cases where the motor was not broken, this is compensated for by assuming the constant torque plateau at the low speed region of the torque speed curve. The speed offset is then calculated by subtracting the data from a linear fit to this, shifted to the origin.

A bead attached to a filament with a rotation rate of approximately 42Hz was selected. The bacterial cell and rotating bead were moved to the centre of the electrodes using the micromanipulators. Successive pulses of electrorotation were then applied to the bead. The pulse lasted for one second and the power was increased in five percent intervals, see figure 6.2. Figure 6.3 a) shows the rotation rates for a polarisable bead attached to a filament, during 11 runs of electrorotation. Figure 6.3 b) is an expanded section of figure a), showing the free rotation of the bead in between each application of electrorotation. The relative number of working stator units can be roughly estimated from this free rotation data. The data were divided according to the estimated stator number, indicated by the red lines, into coloured sections a, b and c. The rotation rate average and standard deviation from the mean are plotted as red points on the free rotation plot, figure 6.3 b). The average rates are 42, 38 and 34, which is a drop of 4Hz per step, corresponding to one stator unit being lost or broken. Figure 6.4 shows the average rotation rate of the free bead for each run, there is a small variation in sections labeled a (black) and c (blue), but there is a larger change over section b (red). This may be due to

more than one stator unit being lost over the course of the runs.

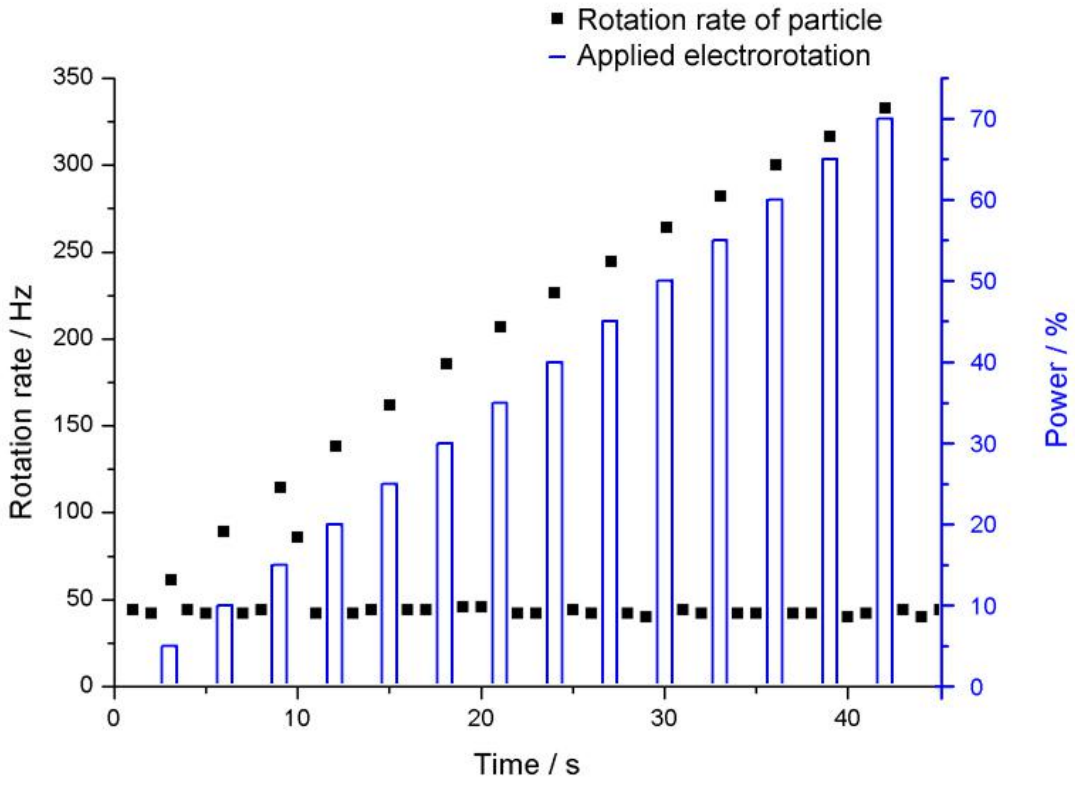

Figure 6.2: Electrorotation of a polarisable bead attached to a filament. The bead's initial rotation rate, due to the flagellar motor, is approximately 42Hz.

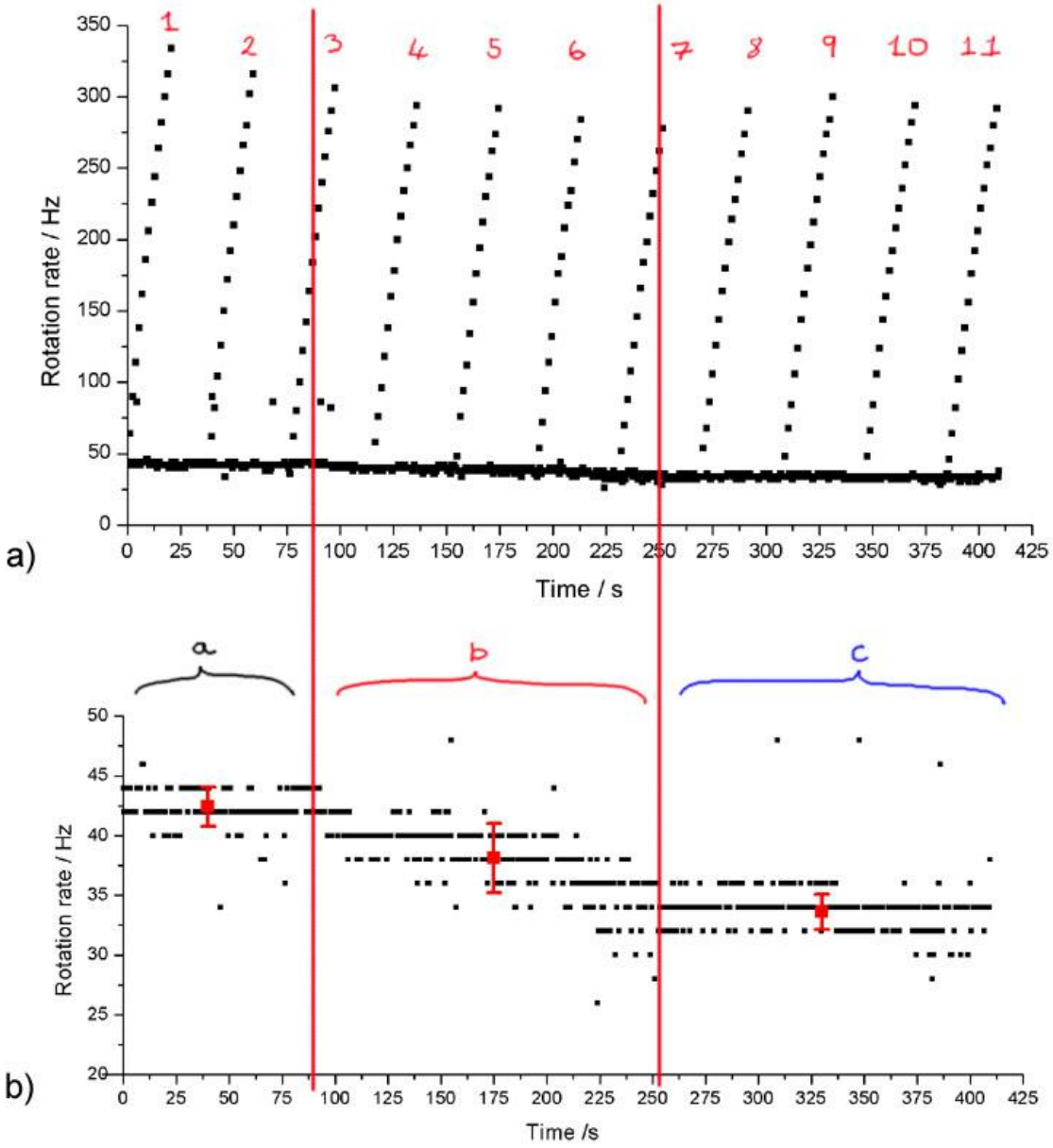

Figure 6.3: The data for the bead in figure 6.2 over 11 applications of electrorotation. a) Speed against time for the entire experiment b) Expanded section of data showing the free rotation of the bead in between applications of electrorotation. Data were divided by eye into steps. The red points at (42.4 ± 1.6)Hz, (38.1 ± 2.9)Hz, (38.1 ± 2.9)Hz are the mean values for sections 'a', 'b' and 'c' respectively.

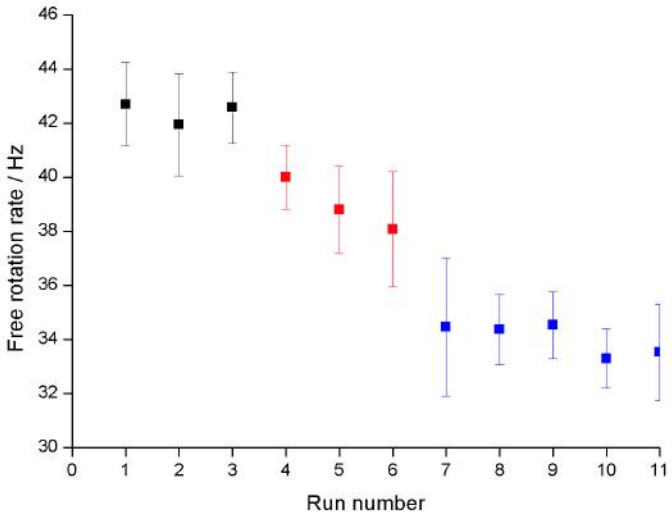

Figure 6.4: The average of the free rotation speed for each run.

Straight line fits were made to each run of electrorotation rates against electrorotation power and the gradients are plotted in figure 6.5. The gradients decrease with time, as was seen in section 4.6 with rotating beads. The decrease in rotation rate is expected to be greater as there are charge cells in the vicinity of the electrodes, from which charge may leak. This charge leakage was reported by Berg and Turner. It was hoped that using low conductivity buffer would have the opposite effect, but this appears not to be the case. However, the change in buffer composition over time is eliminated using the method of fitting a straight line to the data. This is an improvement on the method of Berg and Turner, who may have incurred changes in the torque speed curve due to changes in buffer between one measurement and the next.

Speed offsets are plotted for each run in figure 6.6. It appears as though the zero torque speed drops as the motor loses stator units. One explanation for the overlapping of the curves in various places could be that the stator units are in constant flux, dropping in and out of the motor, and this may cause the data to follow the

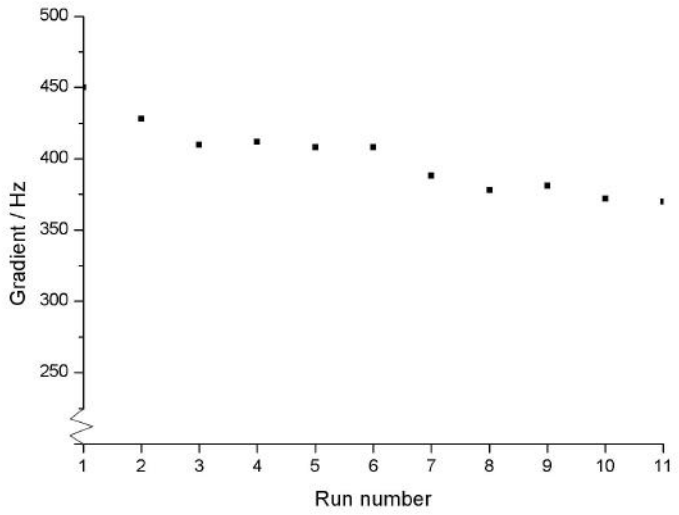

Figure 6.5: The gradient of a straight line fit, for each run from which the speed offset in figure 6.6 was calculated.

torque speed curve for one stator number then switch to that of a higher or lower stator number [67].

The data were then separated into postulated stator number groups. These averages were plotted in figure 6.7. The zero torque speed drops from approximately 325Hz to 300Hz 275Hz. This could correspond to 11, 10 and 9 stator units. As before, the true torque speed curves could be hidden as stator units are lost and then replaced. However, there is still a definite change in the zero torque speed between each curve. As the torque is decreasing, one explanation for the trend in the data is a change in PMF due to charge migration during electrorotation. This possible explanation can be ruled out by the data in the following section.

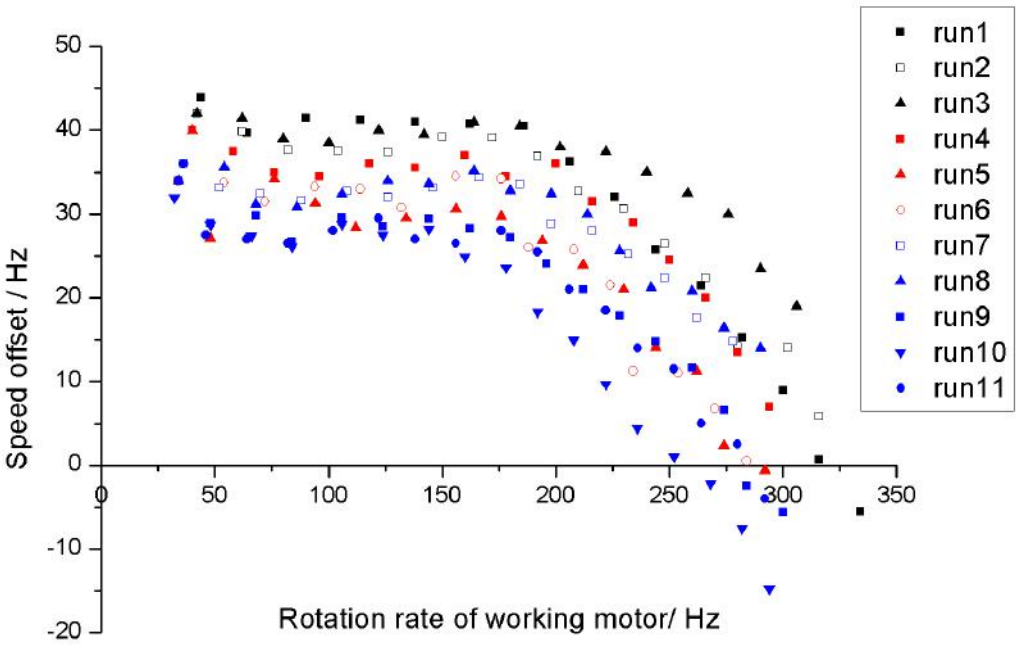

Figure 6.6: The speed offset calculated from data in figure 6.3

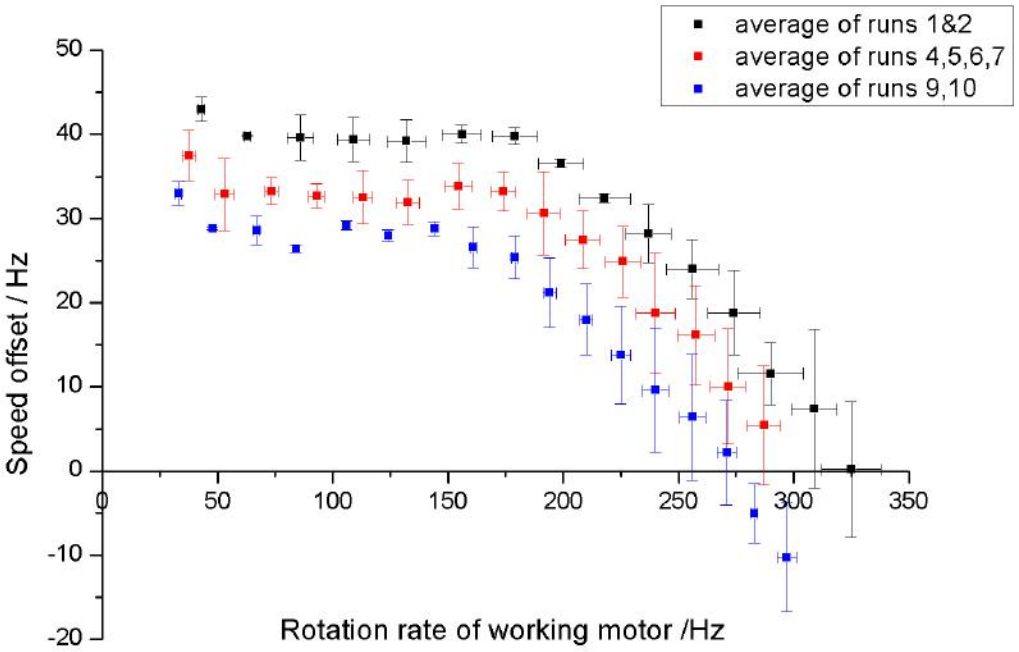

Figure 6.7: The speed offset for the cell in figure 6.3. The runs are split according to steps in the free bead data. Runs (1 and 2), (4,5,6 and 7) and (9 and 10) are averaged. Errors are the standard deviation on the mean.

6.2.2 Part of the torque speed curve: for stators moving out and in to the motor.

A second set of data for KAF95 is shown in graph 6.8. These data show the rotation rate of the motor decreasing, probably due to the breaking or removal of a stator unit. This is followed by an increase in speed, most likely due to the attachment of a working stator unit diffusing from the membrane. The motor is progressively broken from an initial speed of 40Hz to an intermediate speed of 25Hz, it then resurrects to close to its original value. Figure 6.8 b) shows the section of the previous graph corresponding to the rotation rate for the free bead. This is divided up in to sections a, b and c, according to a rough estimate of speed. The average speed of each of these sections is indicated by the red points, with the standard deviation for each section. If the decrease in rotation rate due to charge migration is taken into account, the rotation rate can be seen to drop from an initial value, then jump back to this value. It is possible that either the motor is broken progressively by the electrorotation or that the motor simply loses one or more working stators, at around $5-7$ seconds, then regains this at approximately 32 seconds. The two speed offset plots 6.9 and 6.10 show the constant torque plateau for the cell. It can be assumed that the black and blue plots (corresponding to the first and last two runs) are due to the motor with the same number of stators and the red plot (corresponding to intermediate runs) is due to the motor with fewer stators, possibly one less. As the motor is able to regain its original speed this suggests that the change in the torque speed curve in figures 6.6 and 6.7 is not simply due to a change in PMF brought on by the electric field.

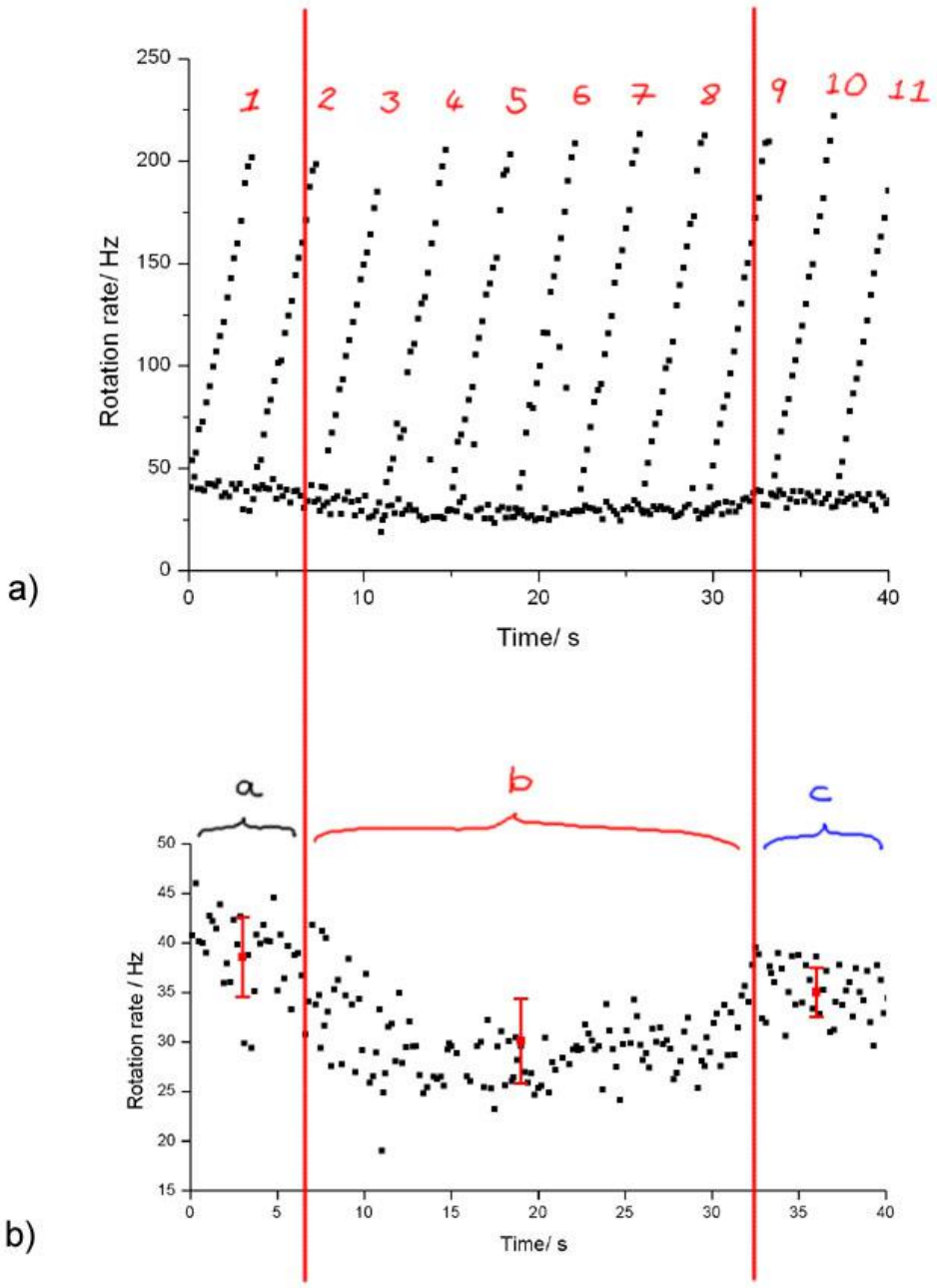

Figure 6.8: a) Raw data for a bead on a cell, the bead is electrorotated eleven times. Each pulse of electrorotation is 0.1 seconds in duration. b) Expanded section of the above raw data. The data has been divided into three steps, a - black, b- red and c- blue. The average speed of the free rotating bead for each of these sections is marked at position $x = 0$ with the standard deviation.

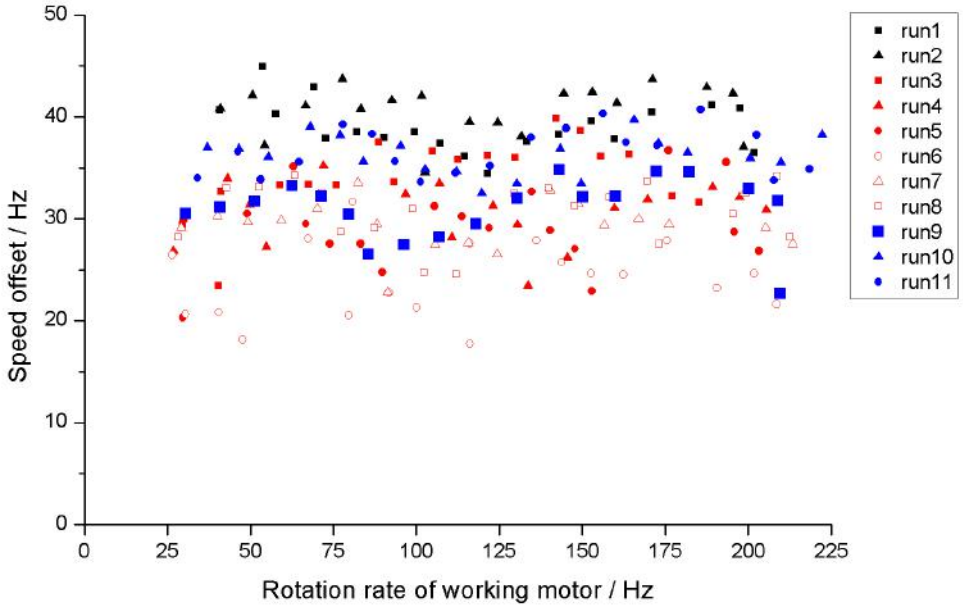

Figure 6.9: The speed offsets for each run, calculated from the data in figure 6.8.

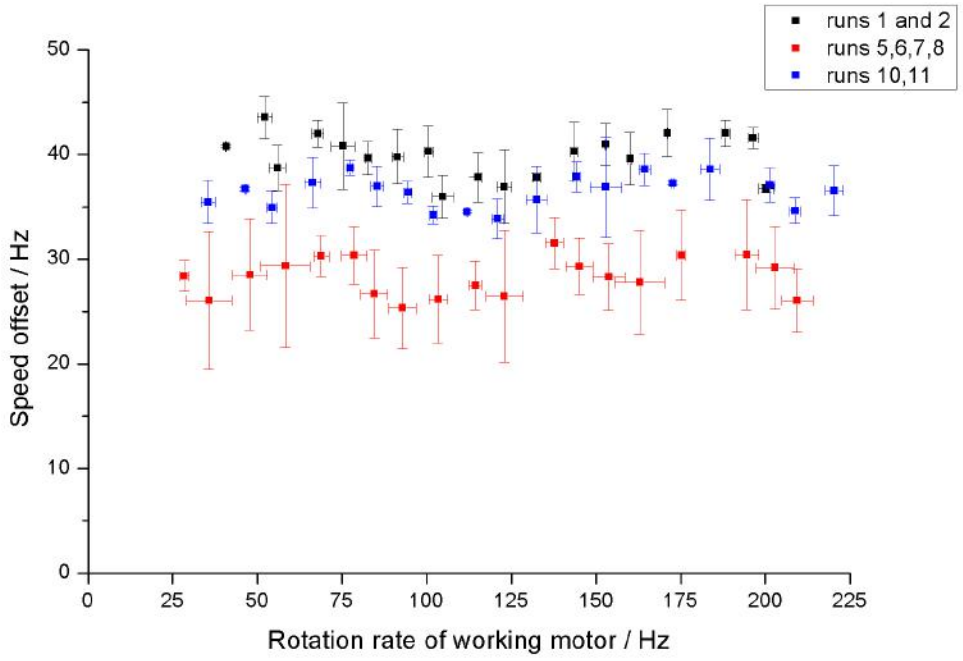

Figure 6.10: Averaged speed offsets for runs (1 and 2), (5,6,7,8) and (10,11). Calculated from the data in figure 6.8.

6.3 Resurrection

Resurrection [71, 59] was attempted as a method of obtaining single stator unit torque speed curves. If it is possible to resurrect a cell and electrorotate it as it increases its stator numbers, this would give a set of torque speed curves for each stator number, for the same motor, with the same load.

The first problem with resurrection of *motA* point mutation strain WSR8, is that it normally requires a resurrection buffer of around 10mM IPTG in motility medium and 10% tryptone broth (TB). This is a highly conductive nutrient broth and as such the carboxy modified latex beads would not rotate in this medium. In order to rotate the beads successfully, the resurrection buffer must be replaced with the low conductivity 1mM HEPES buffer, used in the other electrorotation experiments. This requires that the resurrection protocol is modified to allow for the exchange of buffer. In order to see if this is possible, the resurrection of tethered cells in a simple tape tunnel cell was investigated.

WSR8 were grown in TB with no IPTG for 5 hours. Two tape tunnel slides were made with glass coverslips straight from the box (therefore relatively dirty and hydrophobic) and the bacteria flowed directly into the cell from the growth flask. The bacterial cells tether to the dirty glass surface. To one slide the standard resurrection buffer was added and the resurrection of the cells observed as a control.

To the second slide second slide the resurrection buffer was added for 5 minutes, then the slide was flushed with HEPES. Resurrection was seen to occur as in the control slide.

As this method appeared to be suitable, the experiment was then conducted in

the electrorotation slide with decorated beads. The flow in this slide is much slower as the channel depth is 15μm. It takes approximately 6 seconds for buffer to reach the first electrode centre from when it leaves the inlet. A rotating bead on a cell was selected. The resurrection buffer was then added whilst the set up was on the trap and the cells could be observed. The buffer was removed after 5 minutes. The bead was then rotated. In this case the bead broke free from the tether. It took longer than the time to full resurrection for a second suitable bead on cell to be found. It was concluded that this method, although possible, does not allow sufficient time to find a suitable cell. This is problematic since the yield is low and the time to set up the electrorotation slide is of the order of hours.

6.4 The torque speed relationship under low induction conditions

The motA point mutation strain, WSR8, was used to study the affect of stator number on the torque speed relationship. WSR8 was grown under low induction conditions in 10μM isopropylβ-D-thiogalactopyranoside (IPTG). At this IPTG concentration the distribution of speeds was as shown in figure 6.11. From this graph the speed of one stator unit appears to be between 8 and 10 Hertz. This is in agreement with the findings of Reid *et al.* [61], who found a rotation rate of 7.2$\pm$0.3Hz for a 1μm diameter bead. In this case the bead is of 0.833μm diameter with decoration with 0.202μm so the drag coefficient would be expected to vary. The rotation rates below 5Hz may be due to the motor starting and stopping in this low induction state.

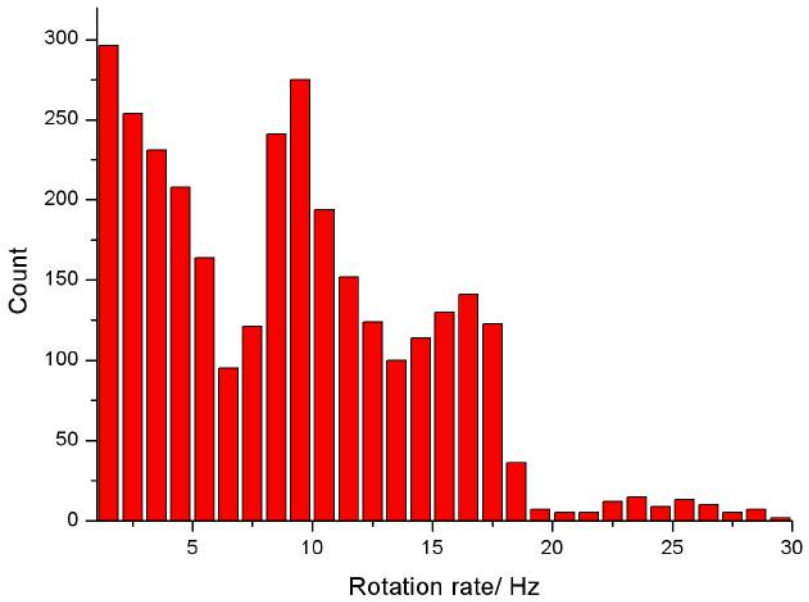

Figure 6.11: Histogram of speeds of rotating decorated beads attached to WSR8 filaments. WSR8 were grown in 10μM IPTG for five hours. Speeds were measured for 24 cells.

As decorated beads seem to be repelled by the cell, they only appear to attach to long filaments and no spinners on short filaments are seen. This means that the bead must be held firmly in the trap to fix its orbit. At low stator numbers the trap strength becomes an issue in measuring speeds. The trap strength at which the bead can be held firmly for the duration of the electrorotation is high enough to also stop the bead from rotating under normal circumstances. Whether the bead is stopped by the trap also seems to depend on the decoration of the bead and position of the motor on the tethered cell, and therefore its orientation in the trap. Some beads will continue to rotate in the trap where as others will be stopped by the trap, in which case it is not possible to measure the rotation rate of the bead between applications of ER.

It is important that the decorated beads are not contaminated and that they stick well to the filaments. Some experiments were unsuccessful as the beads came detached easily at low ER powers. Using detergent to clean the gradient tube on one occasion resulted in the beads not adhering at all to the filaments.

Graph 6.12 shows the data from one cell, which was rotated from between two and six Hertz to 280Hz, four times[2]. Again it was assumed that the torque speed curve is constant in the low speed regime, a linear fit to the first four data points was generated and shifted to the origin. This was subtracted from the raw data to give a speed offset, see figure 6.13 as it was not possible to break the motor. The bead was turning during this experiment, although it is difficult to make this out from the data.

[2]the first run of electrorotation was not up to a high enough power, so the power was increased for subsequent runs

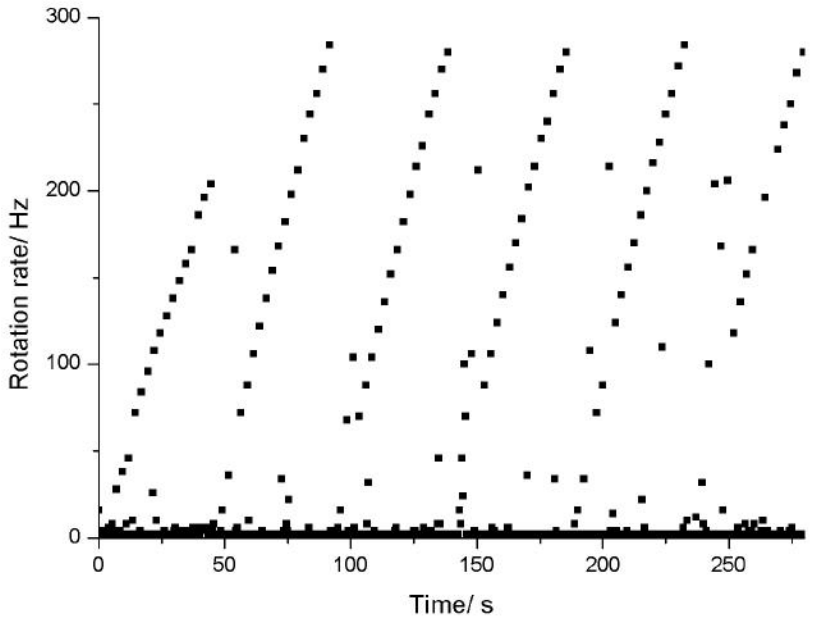

Figure 6.12: Raw data for the electrorotation of a bead on a cell, grown in 10μM IPTG.

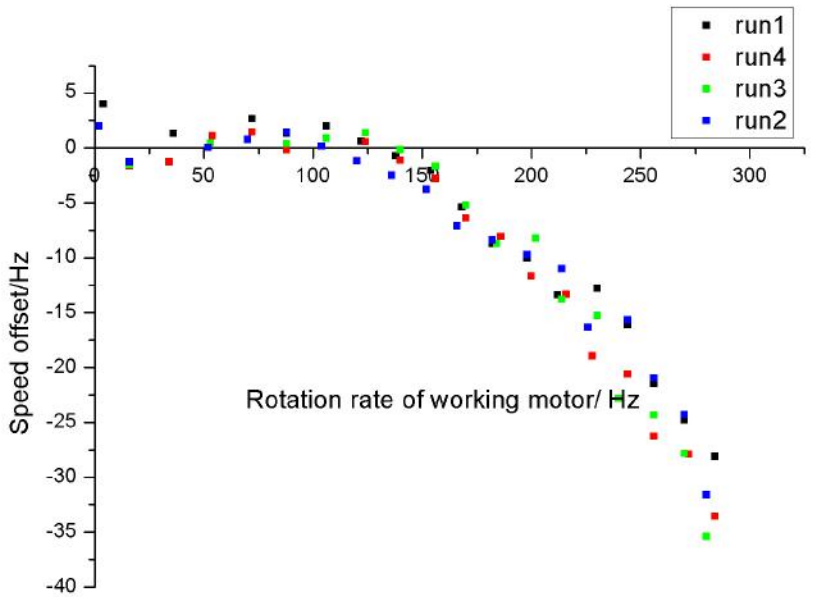

Figure 6.13: Speed offset plots for the cell in figure 6.12: The rotation rate of the motor minus the linear fit for each run, plotted against the rotation rate of the working motor.

6.5 Discussion and conclusions

In the previous chapter, rotation of cells about a tether point showed a torque speed curve similar to those reported in the literature. Zero-torque speed values were 225Hz and 350Hz, also in agreement with previously measured values. Measuring a torque speed curve for varying stator number was attempted but proved difficult due to the low speed per stator unit. The fully induced motor speed ranged from 10Hz to 25Hz depending on cell length. The bead on cell method was then attempted as it was hoped that a higher resolution would be achieved, which would enable more information to be gained about the electrorotation process and variation between recorded torque speed curves.

In this chapter beads attached to filaments were rotated. Again a torque speed curve for non switching strain KAF95 was plotted. In this case it was possible to obtain higher resolution for the rotation of the motor, both during electrorotation and in between applications of external torque. The speed of the free bead would change during the experiment, which could either be attributed to progressive breaking [98] or exchange of stator units with the membrane over time [67]. It is possible to vary the interval over which the bead was rotated. At first a very short interval was used in an effort to minimise damage to the bacterium and motor. It was then noted that higher resolution would be valuable, so the interval was increased. As the time period over which the electrorotation was applied was increased, another effect became evident in the data, that of a decrease in external torque. This can be explained by charge migration due to dielectrophoretic effects, which possibly results in a change in the conductivity of the medium. The longer the runs of electrorotation, the more ionic change in the surrounding medium, possibly due to ion leakage from other cells near the electrodes and the general accumulation of debris. It was possible to apply flow to the channel but the effect of this was not quantifiable. This decrease

in external torque was taken into account by assuming the constant torque plateau in the low speed regime [98, 109, 70], and subtracting from a linear fit based on this assumption.

It is important to have high resolution data of the rotation rate of the free spinning motor between applications of electrorotation, so that the stator number can be inferred. It may be possible to pick out different stator number curves from the repeated rotation of a wild type cell. Use of rotating beads instead of the traditional method of rotating the entire body allows both a higher speed offset, closer to the rotation rate of the filament in its natural environment, and higher resolution data, with a greater difference between rotation rates per stator number. This makes it easier to define a speed for each number of stators and therefore to separate torque speed curves accordingly.

Graphs of the speed offset for the wild type motor, progressively broken, indicate that the value of the zero-torque speed for decreasing stator number may decrease. This would explain the large variation in zero-torque speed values previously recorded. It is possible that the torque speed curves measured previously for fully induced motors [98], were not in fact due to a full complement of stator units, and that the electrorotation process progressively breaks the motor, damaging or removing stators from the motor. This would account for the variation in zero torque speeds found by Berg and Turner etc. Initial results from the progressively broken wild type motor indicate that the zero torque speeds may vary between 200Hz and 400Hz. This conflicts with the predictions of Xing *et al.* [123], which arise from assumptions relating to the shape of the driving potentials of the stator. Xing *et al.* predicted increasing torque with decreasing stator number, however, this prediction is also physically unlikely as the predicted single stator zero-torque speed is

un-feasibly high at 1200Hz.

The *motA* deletion strain, WSR8, containing *motA* behind a *lac* promoter, was again grown at low induction and a histogram of speeds plotted. As the beads are of similar size, there is little variation in drag coefficient. Slightly below the estimates of Reid *et al.* single stator units were measured at approximately 5Hz and two stator units at 10Hz. The fully induced motor has a speed of under 50Hz. At these speeds, the difference in rotation rate between two stator units is within the resolution of the system. A bead attached to a filament of a working motor was rotated and the torque speed curve plotted at low induction. The speed was so low that the cell was unstable, the motor speed would fluctuate rapidly during rotation. The results from these experiments, although in agreement with the fully induced motor results, are therefore unreliable. It would be preferable to repeat these experiments with a medium induction culture with a steady free rotation speed.

Difficulties encountered during experimentation include the following: The yield of cells with decorated beads attached is extremely low, approximately four cells would be seen rotating per slide. The beads also appeared only to stick to long filaments, it is possible that they are repelled by the cell body. As the beads would only stick to long filaments, they must be held in the trap for electrorotation. The alignment of the beads in the trap and orientation of the bead with respect to the hook appears to be crucial [128]. Often the bead would stop spinning when trapped, this was more frequent for the *motA* strain. On some occasions a high power trap would not stop the bead spinning, and it is assumed that the bead orientation is favourable in this case. During electrorotation many of the beads would be pulled out of the trap. This could be due to the ellipticity in the field, damage of the electrodes or inherent properties of the field. This lateral force on the bead often broke

the motor, pulled the bead off or caused the signal to be lost. When low induction experiments were attempted, the yield was decreased further, and the unstable motors would often break when held in the trap.

The data obtained by electrorotation can be qualitatively compared to those of Ryu *et al.* [70] in graph 6.14. The graph is plotted assuming a drag coefficient of 14.5pNnm per revolution per second (that of a 0.833μm diameter bead). The next step would be to fill in the section of the graph for intermediate stator numbers, to confirm the reduction in zero-torque speed with stator number. This could be done by rotating a strain such as WSR8 that has been grown under conditions of medium induction.

In conclusion, the data point towards a decrease in zero torque-speed with stator number, conflicting with the assumptions of Xing *et al.* and Ryu *et al.*. It is important to confirm these results by further experiments and the rotation of a medium induction *E.coli* strain. If there had been more time to work on the project I would have like to have tried some alternative particles to the decorated beads, which do not stick well and are possibly repelled by the cell body, or stick preferentially to the polylysine. These also require the correct orientation in the laser trap, or else the motor will be stalled by the influence of the trap. A higher yield of labeled cells with spinning particles would improve the experiment greatly.

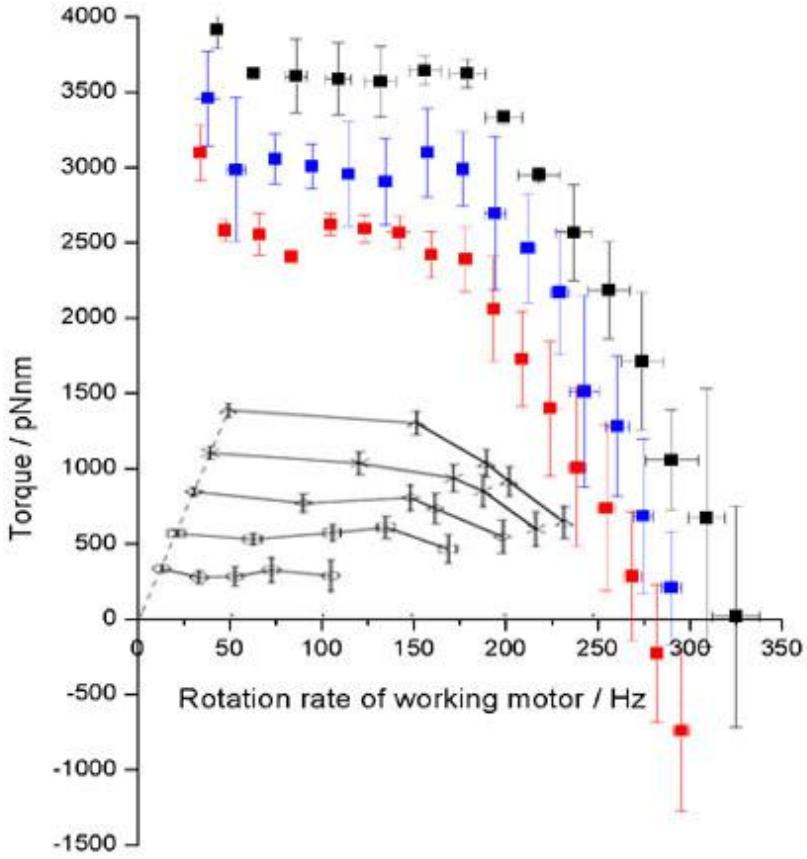

Figure 6.14: The data from one electrorotated cell, compared approximately with that of Ryu *et al.* [70]

Appendix A

Electrorotation theory

A particle in an electric field may experience two types of interaction. A dielectrophoretic(DEP) force, resulting from a gradient in the field and a torque when the electric field vector and dipolar vector are not parallel. This torque can be felt in a uniform field and gives rise to the phenomenon of electrorotation. It is represented by the equation

$$\bar{T} = \bar{p} \times \bar{E} \tag{A.1}$$

where $\bar{p}$ is the dipole moment

The behaviour of a dielectic sphere in an electric field can be described by approximating the dipole induced in the sphere to the effective dipole moment of a free charge point dipole that produces the same dipolar electrostatic potential.

$$p_{eff} = 4\pi\epsilon_1 K R^3 \mathbf{E_0} \tag{A.2}$$

where K, the Claussius-Mossotti factor, is a measure of the polarisability of the particle in the medium.

$$K = \frac{\epsilon_p - \epsilon_m}{\epsilon_p + 2\epsilon_m} \tag{A.3}$$

where ϵ is the permittivity of the particle, (p), and the medium, (m).

However, polarisation of a real dielectric is not instantaneous and as such has a characteristic relaxation time. Non-ideal dielectrics therefore exhibit a frequency dependence in an electric field. This allows a complex permittivity to be defined to describe the frequency response.

If the dielectric is non-ideal, it has both a permittivity and a conductivity, it can be modelled as a loss free capacitor in parallel with a resistor. Impedance for a capacitor given by

$$Z = \frac{1}{i\omega C} \tag{A.4}$$

where the permittivity, ϵ, is

$$C = \epsilon \frac{A}{d} \tag{A.5}$$

When a resistor is placed in series with a capacitor, this becomes

$$Z = \frac{1}{\frac{1}{R} + i\omega C} \tag{A.6}$$

and the resistance is given by

$$R = \frac{1}{\sigma} \frac{d}{A} \tag{A.7}$$

If equation (A.7) is substituted into equation (A.6) and compared with the original equation for the capacitor alone (A.4), a new complex permittivity can be defined

$$\epsilon^{\star} = \epsilon - i\frac{\sigma}{\omega} \tag{A.8}$$

The expression for the effective dipole moment, equation (A.2), becomes

$$p_{eff} = 4\pi\epsilon_m \bar{K}(\omega) R^3 \mathbf{E_0}(\hat{x} - j\hat{y}) \tag{A.9}$$

The time averaged torque is then

$$\langle T \rangle = |p_{eff}| E_0 \sin\alpha \hat{z} \tag{A.10}$$

where

$$\alpha = -\sin^{-1}\{Im[K(w)]/K(w)\} \tag{A.11}$$

At steady state, the drag experienced by the particle or viscous torque T^{ν} is equal to the torque due to the rotating field T^{e}

$$T^{\eta} - T^{e} = 0 \tag{A.12}$$

The angular velocity, using Lamb's approximation, is given by

$$\Omega = -\frac{T^{\eta}}{8\pi\eta_1} \tag{A.13}$$

which can be re written as

$$\Omega = -\frac{\epsilon_m |E|^2}{2\eta} Im(K) \tag{A.14}$$

where the complex Clausius-Mosotti factor is given by:

$$K = \frac{\epsilon_p^{\star} - \epsilon_m^{\star}}{\epsilon_p^{\star} + 2\epsilon_m^{\star}} \tag{A.15}$$

where the complex permittivities for the particle and medium, $\epsilon^{\star}$, are

$$\epsilon_p^{\star} = \epsilon_p + \frac{i\sigma_p}{\omega} \tag{A.16}$$

$$\epsilon_m^{\star} = \epsilon_m + \frac{i\sigma_m}{\omega} \tag{A.17}$$

Bibliography

[1] M Mazumdar, A Mikami, M A Gee, and R B Vallee, *In vitro motility from recombinant dynein heavy chain.*, Proc Natl Acad Sci USA **93**, 6552–6 (1996).

[2] T M Lohman, K Thorn, and R D Vale, *Staying on track: common features of DNA helicases and microtubule motors.*, Cell **93**, 9–12 (1998).

[3] Y L Shih and L Rothfield, *The bacterial cytoskeleton.*, Microbiol Mol Biol Rev **70**, 729–54 (2006).

[4] M Schliwa, **Molecular Motors** (Wiley VCH, 2002).

[5] A Yildiz, M Tomishige, R D Vale, and P R Selvin, *Kinesin walks hand-over-hand.*, Science **303**, 676–8 (2004).

[6] K Svoboda, C F Schmidt, B J Schnapp, and S M Block, *Direct observation of kinesin stepping by optical trapping interferometry.*, Nature **365**, 721–7 (1993).

[7] M J Schnitzer and S M Block, *Kinesin hydrolyses one ATP per 8-nm step.*, Nature **388**, 386–90 (1997).

[8] S Rice, A W Lin, D Safer, C L Hart, N Naber, B O Carragher, S M Cain, E Pechatnikova, E M Wilson-Kubalek, M Whittaker, E Pate, R Cooke, E W Taylor, R A Milligan, and R D Vale, *A structural change in the kinesin motor protein that drives motility.*, Nature **402**, 778–84 (1999).

[9] M Nishiyama, H Higuchi, and T Yanagida, *Chemomechanical coupling of the forward and backward steps of single kinesin molecules.*, Nat Cell Biol **4**, 790–7 (2002).

[10] Y Taniguchi, M Nishiyama, Y Ishii, and T Yanagida, *Entropy rectifies the Brownian steps of kinesin.*, Nat Chem Biol **1**, 342–7 (2005).

[11] N J Carter and R A Cross, *Mechanics of the kinesin step.*, Nature **435**, 308–12 (2005).

[12] Justin E Molloy and Stephan Schmitz, *Molecular motors: kinesin steps back.*, Nature **435**, 285–7 (2005).

[13] R D Vale and R A Milligan, *The way things move: looking under the hood of molecular motor proteins.*, Science **288**, 88–95 (2000).

[14] J E Molloy, J E Burns, J Kendrick-Jones, R T Tregear, and D C White, *Movement and force produced by a single myosin head.*, Nature **378**, 209–12 (1995).

[15] J R Sellers, *Myosins: a diverse superfamily.*, Biochim Biophys Acta **1496**, 3–22 (2000).

[16] J R Moore, E B Krementsova, K M Trybus, and D M Warshaw, *Myosin V exhibits a high duty cycle and large unitary displacement.*, J Cell Biol **155**, 625–35 (2001).

[17] A D Mehta, R S Rock, M Rief, J A Spudich, M S Mooseker, and R E Cheney, *Myosin-V is a processive actin-based motor.*, Nature **400**, 590–3 (1999).

[18] C Veigel, F Wang, M L Bartoo, J R Sellers, and J E Molloy, *The gated gait of the processive molecular motor, myosin V.*, Nat Cell Biol **4**, 59–65 (2002).

[19] T J Purcell, C Morris, J A Spudich, and H L Sweeney, *Role of the lever arm in the processive stepping of myosin V.*, Proc Natl Acad Sci USA **99**, 14159–64 (2002).

[20] A E-M Clemen, M Vilfan, J Jaud, J Zhang, M Barmann, and M Rief, *Force-dependent stepping kinetics of myosin-V.*, Biophys J **88**, 4402–10 (2005).

[21] J P Abrahams, A G Leslie, R Lutter, and J E Walker, *Structure at 2.8 A resolution of F1-ATPase from bovine heart mitochondria.*, Nature **370**, 621–8 (1994).

[22] H Noji, R Yasuda, M Yoshida, and K Jr Kinosita, *Direct observation of the rotation of F1-ATPase.*, Nature **386**, 299–302 (1997).

[23] R Yasuda, H Noji, M Yoshida, K Jr Kinosita, and H Itoh, *Resolution of distinct rotational substeps by submillisecond kinetic analysis of F1-ATPase.*, Nature **410**, 898–904 (2001).

[24] Joachim Weber and Alan E Senior, *ATP synthesis driven by proton transport in F1F0-ATP synthase.*, FEBS Lett **545**, 61–70 (2003).

[25] E M Purcell, *Life at low Reynolds number.*, Am J Phys **45**, 3–11 (1977).

[26] D R Thomas, N R Francis, C Xu, and D J DeRosier, *The three-dimensional structure of the flagellar rotor from a clockwise-locked mutant of Salmonella enterica serovar Typhimurium.*, J Bacteriol **188**, 7039–48 (2006).

[27] S H Larsen, J Adler, J J Gargus, and R W Hogg, *Chemomechanical coupling without ATP: the source of energy for motility and chemotaxis in bacteria.*, Proc Natl Acad Sci U S A **71**, 1239–43 (1974).

[28] M D Manson, P Tedesco, H C Berg, F M Harold, and C Van der Drift, *A*

protonmotive force drives bacterial flagella., Proc Natl Acad Sci U S A **74**, 3060–4 (1977).

[29] J I Shioi, S Matsuura, and Y Imae, *Quantitative measurements of proton motive force and motility in Bacillus subtilis.*, J Bacteriol **144**, 891–7 (1980).

[30] N Hirota and Y Imae, *Na+-driven flagellar motors of an alkalophilic Bacillus strain YN-1.*, J Biol Chem **258**, 10577–81 (1983).

[31] Y Magariyama, S Sugiyama, K Muramoto, Y Maekawa, I Kawagishi, Y Imae, and S Kudo, *Very fast flagellar rotation.*, Nature **371**, 752 (1994).

[32] K Muramoto, I Kawagishi, S Kudo, Y Magariyama, Y Imae, and M Homma, *High-speed rotation and speed stability of the sodium-driven flagellar motor in Vibrio alginolyticus.*, J Mol Biol **251**, 50–8 (1995).

[33] M Meister, G Lowe, and H C Berg, *The proton flux through the bacterial flagellar motor.*, Cell **49**, 643–50 (1987).

[34] R M Macnab and D E Jr Koshland, *The gradient-sensing mechanism in bacterial chemotaxis.*, Proc Natl Acad Sci U S A **69**, 2509–12 (1972).

[35] H C Berg and D A Brown, *Chemotaxis in Escherichia coli analysed by three-dimensional tracking.*, Nature **239**, 500–4 (1972).

[36] D L Milligan and D E Jr Koshland, *Site-directed cross-linking. Establishing the dimeric structure of the aspartate receptor of bacterial chemotaxis.*, J Biol Chem **263**, 6268–75 (1988).

[37] S L Mowbray and M O Sandgren, *Chemotaxis receptors: a progress report on structure and function.*, J Struct Biol **124**, 257–75 (1998).

[38] J R Maddock and L Shapiro, *Polar location of the chemoreceptor complex in the Escherichia coli cell.*, Science **259**, 1717–23 (1993).

[39] M Levit, Y Liu, M Surette, and J Stock, *Active site interference and asymmetric activation in the chemotaxis protein histidine kinase CheA.*, J Biol Chem **271**, 32057–63 (1996).

[40] J F Hess, K Oosawa, N Kaplan, and M I Simon, *Phosphorylation of three proteins in the signaling pathway of bacterial chemotaxis.*, Cell **53**, 79–87 (1988).

[41] M Welch, K Oosawa, S Aizawa, and M Eisenbach, *Phosphorylation-dependent binding of a signal molecule to the flagellar switch of bacteria.*, Proc Natl Acad Sci USA **90**, 8787–91 (1993).

[42] George H Wadhams and Judith P Armitage, *Making sense of it all: bacterial chemotaxis.*, Nat Rev Mol Cell Biol **5**, 1024–37 (2004).

[43] F A Samatey, H Matsunami, K Imada, S Nagashima, T R Shaikh, D R Thomas, J Z Chen, D J Derosier, A Kitao, and K Namba, *Structure of the bacterial flagellar hook and implication for the molecular universal joint mechanism.*, Nature **431**, 1062–8 (2004).

[44] H C Berg, *The rotary motor of bacterial flagella.*, Annu Rev Biochem **72**, 19–54 (2003).

[45] David F Blair, *Flagellar movement driven by proton translocation.*, FEBS Lett **545**, 86–95 (2003).

[46] M L DePamphilis and J Adler, *Purification of intact flagella from Escherichia coli and Bacillus subtilis.*, J Bacteriol **105**, 376–83 (1971).

[47] M L DePamphilis and J Adler, *Fine structure and isolation of the hook-basal body complex of flagella from Escherichia coli and Bacillus subtilis.*, J Bacteriol **105**, 384–95 (1971).

[48] H Suzuki, K Yonekura, and K Namba, *Structure of the rotor of the bacterial flagellar motor revealed by electron cryomicroscopy and single-particle image analysis.*, J Mol Biol **337**, 105–13 (2004).

[49] Yumiko Saijo-Hamano, Naoko Uchida, Keiichi Namba, and Kenji Oosawa, *In vitro characterization of FlgB, FlgC, FlgF, FlgG, and FliE, flagellar basal body proteins of Salmonella.*, J Mol Biol **339**, 423–35 (2004).

[50] S Kojima and D F Blair, *The bacterial flagellar motor: structure and function of a complex molecular machine.*, Int Rev Cytol **233**, 93–134 (2004).

[51] P N Brown, C P Hill, and D F Blair, *Crystal structure of the middle and C-terminal domains of the flagellar rotor protein FliG.*, EMBO J **21**, 3225–34 (2002).

[52] S A Lloyd and D F Blair, *Charged residues of the rotor protein FliG essential for torque generation in the flagellar motor of Escherichia coli.*, J Mol Biol **266**, 733–44 (1997).

[53] X F Zhou, J P Burt, and R Pethig, *Automatic cell electrorotation measurements: studies of the biological effects of low-frequency magnetic fields and of heat shock.*, Phys Med Biol **43**, 1075–90 (1998).

[54] H Sockett, S Yamaguchi, M Kihara, V M Irikura, and R M Macnab, *Molecular analysis of the flagellar switch protein FliM of Salmonella typhimurium.*, J Bacteriol **174**, 793–806 (1992).

[55] P N Brown, M A A Mathews, L A Joss, C P Hill, and D F Blair, *Crystal structure of the flagellar rotor protein FliN from Thermotoga maritima.*, J Bacteriol **187**, 2890–902 (2005).

[56] S A Lloyd, F G Whitby, D F Blair, and C P Hill, *Structure of the C-terminal*

domain of FliG, a component of the rotor in the bacterial flagellar motor., Nature **400**, 472–5 (1999).

[57] D F Blair and H C Berg, *The MotA protein of E. coli is a proton-conducting component of the flagellar motor.*, Cell **60**, 439–49 (1990).

[58] J Zhou and D F Blair, *Residues of the cytoplasmic domain of MotA essential for torque generation in the bacterial flagellar motor.*, J Mol Biol **273**, 428–39 (1997).

[59] S M Block and H C Berg, *Successive incorporation of force-generating units in the bacterial rotary motor.*, Nature **309**, 470–2 (1984).

[60] D F Blair and H C Berg, *Restoration of torque in defective flagellar motors.*, Science **242**, 1678–81 (1988).

[61] S W Reid, M C Leake, J H Chandler, C Lo, J P Armitage, and R M Berry, *The maximum number of torque-generating units in the flagellar motor of Escherichia coli is at least 11.*, Proc Natl Acad Sci USA **103**, 8066–71 (2006).

[62] G E Dean, R M Macnab, J Stader, P Matsumura, and C Burks, *Gene sequence and predicted amino acid sequence of the motA protein, a membrane-associated protein required for flagellar rotation in Escherichia coli.*, J Bacteriol **159**, 991–9 (1984).

[63] R De Mot and J Vanderleyden, *The C-terminal sequence conservation between OmpA-related outer membrane proteins and MotB suggests a common function in both gram-positive and gram-negative bacteria, possibly in the interaction of these domains with peptidoglycan.*, Mol Microbiol **12**, 333–4 (1994).

[64] S Khan, M Dapice, and T S Reese, *Effects of mot gene expression on the structure of the flagellar motor.*, J Mol Biol **202**, 575–84 (1988).

[65] T F Braun, L Q Al-Mawsawi, S Kojima, and D F Blair, *Arrangement of core membrane segments in the MotA/MotB proton-channel complex of Escherichia coli.*, Biochemistry **43**, 35–45 (2004).

[66] S M Van Way, E R Hosking, T F Braun, and M D Manson, *Mot protein assembly into the bacterial flagellum: a model based on mutational analysis of the motB gene.*, J Mol Biol **297**, 7–24 (2000).

[67] M C Leake, J H Chandler, G H Wadhams, F Bai, R M Berry, and J P Armitage, *Stoichiometry and turnover in single, functioning membrane protein complexes.*, Nature **443**, 355–8 (2006).

[68] G E Murphy, J R Leadbetter, and G J Jensen, *In situ structure of the complete Treponema primitia flagellar motor.*, Nature **442**, 1062–4 (2006).

[69] M Silverman and M Simon, *Flagellar rotation and the mechanism of bacterial motility.*, Nature **249**, 73–4 (1974).

[70] W S Ryu, R M Berry, and H C Berg, *Torque-generating units of the flagellar motor of Escherichia coli have a high duty ratio.*, Nature **403**, 444–7 (2000).

[71] M Silverman, P Matsumura, and M Simon, *The identification of the mot gene product with Escherichia coli-lambda hybrids.*, Proc Natl Acad Sci USA **73**, 3126–30 (1976).

[72] A Ashkin, *Optical trapping and manipulation of neutral particles using lasers.*, Proc Natl Acad Sci U S A **94**, 4853–60 (1997).

[73] A Ashkin and J M Dzeidzic, *Observation of radiation-pressure trapping of particles by alternating light beams.*, Phys Rev Lett **54**, 1245–1248 (1985).

[74] A Ashkin and J M Dziedzic, *Optical trapping and manipulation of viruses and bacteria.*, Science **235**, 1517–20 (1987).

[75] A Ashkin, J M Dziedzic, and T Yamane, *Optical trapping and manipulation of single cells using infrared laser beams.*, Nature **330**, 769–71 (1987).

[76] K C Neuman, *Optical trapping.*, Rev Sci Instrum **75**, 2787–2809 (2004).

[77] J E Molloy and M Padgett, *Lights, action: Optical tweezers*, Contemporary Physics **43**, 241–258 (2002).

[78] M J Lang, P M Fordyce, A M Engh, K C Neuman, and S M Block, *Simultaneous, coincident optical trapping and single-molecule fluorescence.*, Nat Methods **1**, 133–9 (2004).

[79] A I Bishop, T A Nieminen, N R Heckenberg, and H Rubinsztein-Dunlop, *Optical microrheology using rotating laser-trapped particles.*, Phys Rev Lett **92**, 198104 (2004).

[80] J Plewa, E Tanner, D M Mueth, and D G Grier, *Processing carbon nanotubes with holographic optical tweezers*, Optics Express **12**, 1978–1981 (2004).

[81] M W Allersma, F Gittes, M J deCastro, R J Stewart, and C F Schmidt, *Two-dimensional tracking of ncd motility by back focal plane interferometry.*, Biophys J **74**, 1074–85 (1998).

[82] W M Arnold and U Zimmermann, *Rotating-field-induced rotation and measurement of the membrane capacitance of single mesophyll cells of Avena sativa*, Z Naturforsch **37c**, 908–915 (1982).

[83] Y Huang, R Holzel, R Pethig, and X B Wang, *Differences in the AC electrodynamics of viable and non-viable yeast cells determined through combined dielectrophoresis and electrorotation studies.*, Phys Med Biol **37**, 1499–517 (1992).

[84] Y Huang and R Pethig, *Electrode design for negative dielectrophoresis.*, Meas Sci Technol **2**, 1142–46 (1991).

[85] X B Wang, Y Huang, J P H Burt, G H Markx, and R Pethig, *Selective dielectrophoretic confinement of bioparticles in potential energy wells.*, J Phys D: Appl Phys **26**, 1278–85 (1993).

[86] M P Hughes, S Archer, and H Morgan, *Computer-aided analysis of electric fields used in electrorotation studies.*, J Phys D: Appl Phys **27**, 1564–70 (1994).

[87] M P Hughes S Archer and H Morgan, *Mapping the electrorotational torque in planar microelectrodes.*, J Phys D: Appl Phys **32**, 1548–52 (1999).

[88] J Park, S Jung, Y Kim, B Kim, S Lee, and J o Park, *Design and fabrication of an integrated cell processor for single embryo cell manipulation.*, Lab Chip **5**, 91–6 (2005).

[89] Y Huang, X B Wang, J A Tame, and R Pethig, *Electrokinetic behaviour of particle travelling in electric fields.*, J Phys D: Appl Phys **26**, 1528–35 (1993).

[90] R Georgieva, S Moya, E Donath, and H Baumler, *Permeability and conductivity of red blood cell templated polyelectrolyte capsules coated with supplementary layers.*, Langmuir **20**, 1895–900 (2004).

[91] A D Goater and R Pethig, *Electrorotation and dielectrophoresis.*, Parasitology **117 Suppl**, S177–89 (1998).

[92] C Dalton, A D Goater, J P H Burt, and H V Smith, *Analysis of parasites by electrorotation.*, J Appl Microbiol **96**, 24–32 (2004).

[93] B Walderich, G D Burchard, J Knobloch, and L Muller, *Development of monoclonal antibodies specifically recognizing the cyst stage of Entamoeba histolytica.*, Am J Trop Med Hyg **59**, 347–51 (1998).

[94] J Gimsa, C Pritzen, and E Donath, *Characterisation of virus-red-cell interaction by electrorotation.*, Studies in Biophys **130**, 123–131 (1989).

[95] C Reichle, T Muller, T Schnelle, and G Fuhr, *Electrorotation in octopole micro cages.*, J Phys D: Appl Phys **32**, 2128–35 (1999).

[96] C Reichle, T Schnelle, T Muller, T Leya, and G Fuhr, *A new microsystem for automated electrorotation measurements using laser tweezers.*, Biochim Biophys Acta **1459**, 218–29 (2000).

[97] D Meitchen, T Schnelle, T Muller, R Hagedorn, and G Fuhr, *Automated dielectric single cell spectroscopy - temperature dependence of electrorotation*, J Phys D: Appl Phys **35**, 1258–1270 (2002).

[98] H C Berg and L Turner, *Torque generated by the flagellar motor of Escherichia coli.*, Biophys J **65**, 2201–16 (1993).

[99] M Meister, S R Caplan, and H C Berg, *Dynamics of a tightly coupled mechanism for flagellar rotation. Bacterial motility, chemiosmotic coupling, protonmotive force.*, Biophys J **55**, 905–14 (1989).

[100] M Washizu, Y Kurahashi, H Iochi, O Kurosawa, S Aizawa, S Kudo, Y Magariyama, and H Hotani, *Dielectrophoretic measurement of bacterial motor characteristics.*, IEEE **29**, 286–94 (1993).

[101] S Khan, M Meister, and H C Berg, *Constraints on flagellar rotation.*, J Mol Biol **184**, 645–56 (1985).

[102] A D Samuel and H C Berg, *Fluctuation analysis of rotational speeds of the bacterial flagellar motor.*, Proc Natl Acad Sci USA **92**, 3502–6 (1995).

[103] Y Sowa, A D Rowe, M C Leake, T Yakushi, M Homma, A Ishijima, and R M

Berry, *Direct observation of steps in rotation of the bacterial flagellar motor.*, Nature **437**, 916–9 (2005).

[104] R M Berry, L Turner, and H C Berg, *Mechanical limits of bacterial flagellar motors probed by electrorotation.*, Biophys J **69**, 280–6 (1995).

[105] R M Berry and H C Berg, *Torque generated by the bacterial flagellar motor close to stall.*, Biophys J **71**, 3501–10 (1996).

[106] R M Berry and H C Berg, *Absence of a barrier to backwards rotation of the bacterial flagellar motor demonstrated with optical tweezers.*, Proc Natl Acad Sci U S A **94**, 14433–7 (1997).

[107] R M Berry and H C Berg, *Torque generated by the flagellar motor of Escherichia coli while driven backward.*, Biophys J **76**, 580–7 (1999).

[108] G Lowe, M Meister, and H C Berg, *Rapid rotation of flagellar bundles in swimming bacteria.*, Nature **325**, 637–640 (1987).

[109] X Chen and H C Berg, *Torque-speed relationship of the flagellar rotary motor of* Escherichia coli, Biophys J **78**, 1036–41 (2000).

[110] C V Gabel and H C Berg, *The speed of the flagellar rotary motor of Escherichia coli varies linearly with protonmotive force.*, Proc Natl Acad Sci USA **100**, 8748–51 (2003).

[111] S Khan and H C Berg, *Isotope and thermal effects in chemiosmotic coupling to the membrane ATPase of Streptococcus.*, J Biol Chem **258**, 6709–12 (1983).

[112] P Lauger, *Ion transport and rotation of bacterial flagella.*, Nature **268**, 360–2 (1977).

[113] R M Berry, *Torque and switching in the bacterial flagellar motor. An electrostatic model.*, Biophys J **64**, 961–73 (1993).

[114] P Lauger, *Torque and rotation rate of the bacterial flagellar motor.*, Biophys J **53**, 53–65 (1988).

[115] S Kojima and D F Blair, *Conformational change in the stator of the bacterial flagellar motor.*, Biochemistry **40**, 13041–50 (2001).

[116] R Schmitt, *Helix rotation model of the flagellar rotary motor.*, Biophys J **85**, 843–52 (2003).

[117] D Walz and S R Caplan, *An electrostatic mechanism closely reproducing observed behavior in the bacterial flagellar motor.*, Biophys J **78**, 626–51 (2000).

[118] A Mogilner, T Elston, H Wang, and G Oster, **Molecular motors: Theory, in Computational Cell Biology** (Springer, NY, 2002).

[119] T Atsumi, *An ultrasonic motor model for bacterial flagellar motors.*, J Theor Biol **213**, 31–51 (2001).

[120] D Keller and C Bustamante, *The mechanochemistry of molecular motors.*, Biophys J **78**, 541–56 (2000).

[121] D Walz and S R Caplan, *A kinetic and stochastic analysis of crossbridge-type stepping mechanisms in rotary molecular motors.*, Biophys J **89**, 1650–6 (2005).

[122] R M Berry, *Torque and switching in the bacterial flagellar motor*, Biophys J **64**, 961–973 (1993).

[123] Jianhua Xing, Fan Bai, Richard Berry, and George Oster, *Torque-speed relationship of the bacterial flagellar motor.*, Proc Natl Acad Sci USA **103**, 1260–5 (2006).

[124] H Wang and G Oster, *Ratchets, power strokes and molecular motors*, Applied Physics A. **75**, 315–323 (2002).

[125] J Xing, H Wang, and G Oster, *From continuum Fokker-Planck models to discrete kinetic models.*, Biophys J **89**, 1551–63 (2005).

[126] A D Rowe, M C Leake, H Morgan, and R M Berry, *Rapid rotation of micron and submicron dielectric particles measured using optic tweezers*, J Modern Optics **50**, 1539–1554 (2003).

[127] K Svoboda and S M Block, *Biological applications of optical forces.*, Annu Rev Biophys Biomol Struct **23**, 247–85 (1994).

[128] T Pilizota, **A programmable optical angle clamp for rotary molecular motors**, D.Phil thesis, Oxford University, 2006.